Development of Reduced Dimensional Modeling Techniques for Laminar Pressure-Induced Flows in Narrow Gaps with Sudden Expansion

Master's Thesis

by

Abdulla Rahmah and Leo Flydalen

Department of Energy Sciences
Lund University
Sweden
June 17, 2024

Company Supervisor: **Lea Versbach, PhD**
Academic Supervisor: **Professor Johan Revstedt**
Examiner: **Professor Christer Fureby**

This degree project for the degree of Master of Science in Engineering has been conducted at the Department of Energy Sciences, Faculty of Engineering, Lund University.

Supervisor at the Department of Energy Sciences was Professor Johan Revstedt. Supervisor at FS Dynamics Sweden AB was Lea Versbach, PhD.

Examiner at Lund University was Professor Christer Fureby.

The project was carried out in cooperation with FS Dynamics Sweden AB in Lund.

Department of Energy Sciences
Faculty of Engineering
Lund University

ISSN: <0282-1990>
LUTMDN/TMHP-24/5582-SE

Typeset in LaTeX
Lund 2024

Abstract

Simulations of domains with large differences in length scales across different directions are often computationally expensive because they require high mesh resolution, leading to long simulation times. This master's thesis was done in collaboration with FS Dynamics Sweden AB and addressed the high computational cost associated with fully resolved 3D simulations. Inspired by semiconductor and electronics applications, with pressure-induced laminar fluid flow occurring within narrow gaps with sudden expansions, this thesis aimed to develop a model with reduced dimensionality, specifically adhering to the narrow section of the domain.

As a result, models with reduced dimensionality, referred to as the *Pseudo 2D-C* and *Pseudo 2D-C2* models, were constructed within the confined thin section, featuring one cell in the orthogonal direction of the main flow. A more complex and substantially different geometrical configuration was also evaluated. Due to the dissimilar methodology employed, the developed reduced dimensional model was referred to as the *Pseudo 2D-CX*. The research focused on validating the reduced dimensional models against full 3D simulations for low Reynolds number laminar air flows, using the STAR-CCM+ computational fluid dynamics software. The main properties of interest were the pressure within the confined domain and the velocity at the entrance to the connected larger space. To enhance the accuracy of the reduced dimensional model and conserve the desired flow properties, user-defined field functions were integrated based on theoretical and analytical derivations. Various geometrical configurations were incorporated including parallel plates and ducts with different geometrical features along with a pin-fin geometry, to evaluate the model's applicability and cell reduction possibilities for various representations of industrial occurrences.

The study revealed that the reduced dimensional model for all geometrical components in this project accurately represented the results of the 3D simulations, given the appropriate methodology, conditions, and field function implementation. It also revealed a significant reduction in mesh count, consequently reducing computational cost and increasing time efficiency.

Acknowledgements

This master's thesis marks the culmination of our five-year education in mechanical engineering at The Faculty of Engineering at Lund University. This thesis was conducted at FS Dynamics Sweden AB in Lund.

We extend our deepest gratitude to FS Dynamics Sweden AB for providing us with the opportunity to conduct this thesis with them. Special thanks go to our supervisor, Lea Versbach, PhD for her unfaltering support, guidance, and invaluable knowledge throughout the project. We also extend our appreciation to Mikael Fredenberg for the valuable discussions and meetings we had.

We are grateful for our colleagues at FS Dynamics Sweden AB for their warm welcoming and for engaging conversations.

Further, we want to thank all professors and lecturers at the Department of Energy Science, The Faculty of Engineering at Lund University for their invaluable contributions to our academic and professional growth by sharing their extensive knowledge. We would like to express special gratitude to our supervisor, Professor Johan Revstedt, for his guidance, valuable advice, and sharing of knowledge throughout this thesis.

Lastly, we thank our families for their unwavering support throughout our education and for always believing in us.

List of Figures

List of Tables

Nomenclature

Latin Letters

a $[m]$	Width of a general duct
A $[m^2]$	Area
$\mathbf{a}_f$ $[m^2]$	Surface area vector of face f
b $[m]$	Height of a general duct
D_h $[m]$	Hydraulic diameter
f $[-]$	Mesh stretching factor
h $[m]$	Distance between the plates
J $[\frac{W}{m^2}]$	Convective or diffusive flux
l $[m]$	Length of the plates
L $[m]$	Length
L_{char} $[m]$	Characteristic length
L_{DSM} $[m]$	Length of *denser mesh region*
L_e $[m]$	Hydrodynamic entrance length
$\dot{m}$ $[\frac{kg}{m \cdot s}]$	Mass flow rate per unit length
$\dot{M}$ $[\frac{kg}{s}]$	Mass flow rate
n $[-]$	Normal surface vector
p $[Pa]$	Pressure
p_{diff} $[Pa]$	Pressure difference
p'_{2D} $[\frac{kg}{s^2}]$	Momentum flow rate per unit width (*Pseudo 2D*)
p'_{3D} $[\frac{kg}{s^2}]$	Momentum flow rate per unit width (*3D* model)
P $[m]$	Perimeter of geometry
P_{2D*} $[m]$	Pressure of concerned *Pseudo 2D* model
P_{3D} $[m]$	Pressure of *3D* model
r $[m]$	Radius
Re $[-]$	Reynolds number
S $[-]$	Source term
S_M $[-]$	Momentum source term
t $[s]$	Time
u $[\frac{m}{s}]$	Velocity x-component

U $[\frac{m}{s}]$	Velocity
U_{2D*} $[\frac{m}{s}]$	Velocity of concerned *Pseudo 2D* model
U_{3D} $[\frac{m}{s}]$	Velocity of *3D* model
U_{diff} $[\frac{m}{s}]$	Velocity difference
U_{mag} $[\frac{m}{s}]$	Velocity magnitude
U_{max} $[\frac{m}{s}]$	Maximum velocity
$U_{max,2D}$ $[\frac{m}{s}]$	Maximum velocity for *Pseudo 2D* model
$U_{max,3D}$ $[\frac{m}{s}]$	Maximum velocity for *3D* model
u_b $[\frac{m}{s}]$	Bulk velocity
$\mathbf{u}$ $[\frac{m}{s}]$	Velocity vector
$\mathbf{u}_b$ $[\frac{m}{s}]$	Bulk velocity vector
v $[\frac{m}{s}]$	Velocity y-component
V $[m^3]$	Volume
w $[\frac{m}{s}]$	Velocity z-component

Greek Letters

α $[-]$	Correction factor in *Pseudo 2D-C2*
γ $[-]$	Mean free path
Γ $[-]$	Diffusion coefficient
ϵ_{mo} $[-]$	Momentum residual
ϵ_v $[-]$	Maximum velocity residual
ϵ^* $[-]$	Pressure residual
μ $[Pa \cdot s]$	Dynamic viscosity
ξ $[-]$	Minor loss coefficient
ρ $[\frac{kg}{m^3}]$	Density
τ $[\frac{N}{m^2}]$	Shear stress
ϕ $[-]$	Generic variable

List of Abbreviations

CAE	Computer Aided Engineering
CFD	Computational fluid dynamics
HVAC	Heating, ventilation and air conditioning
RANS	Reynolds-averaged Navier-Stokes equations
CPU	Central processing unit
CV	Control volume
FEA	Finite Element Analysis
FV	Finite volume
LES	Large eddy simulations
PDE	Partial differential equation

Contents

1 Introduction

The background, motivation, and goals of the project are presented in the following sections, focusing on the development of a reduced dimensional model. The aim is to create a generalized, highly applicable model for a wide range of industries, relevant to Computational Fluid Dynamics (CFD). This is done to enhance computational efficiency by reducing the mesh count used in simulations.

1.1 FS Dynamics

This master's thesis is done in collaboration with FS Dynamics Sweden AB, a company specializing in providing consulting services in Computer Aided Engineering (CAE), a field that combines fundamental physics, mathematics, and advanced computing. FS Dynamics offers expertise in the areas of Computational Fluid Dynamics (CFD) and Structural Dynamics using Finite Element Analysis (FEA). They work within various industries and areas, including automotive, fossil-free power production, marine, offshore, and semi-conductors [1].

1.2 Background and Motivation

Simulations of domains with significant differences in length scales in different dimensions are computationally expensive due to the inevitable high cell count. FS Dynamics has undertaken projects of this nature, particularly in the semi-conductor industry, where pressure-induced airflow is present in narrow gaps, such as between closely spaced plates and within long, narrow channels with different geometrical configurations. Due to high computational cost, FS Dynamics proposed the idea to investigate if it is possible to simulate this type of flow using a reduced dimensional model. The model would consist of one cell in the orthogonal direction of the main flow, instead of a fully resolved 3D model. This would have the aim to save mesh count and, consequently, simulation time, while still maintaining good accuracy.

Inspired by the mentioned semi-conductor and electronics applications, where pressure-induced laminar fluid flow occurs in small confined channels with narrow gaps, this thesis aims to develop a model with reduced dimensionality. The primary objective is to enhance computational efficiency by reducing the cell count, essentially decreasing the amount of data points necessary in the simulation. The model development will be enabled by the relatively simple and typically part-wise uniform geometries encountered in the regarded industry, making the generation of a lower-order structured mesh possible. In this project, the fluid, which is a gas (air), will be simulated utilizing computational fluid dynamics (CFD) in the software STAR-CCM+. After performing simulations, a validation between the developed simplified model and the fully resolved 3D model will be made. To support the validity and construction of the model, analytical solutions for a few simplified cases will be conducted by leveraging the theory of Poiseuille flows [22]. To enhance the accuracy of the reduced dimensional model with one cell in the orthogonal direction to the flow, user-defined field functions will be integrated to conserve the flow properties. The main properties of interest are the pressure along the channel and the velocity of the free outflow into the larger downstream fully resolved space. Figure 1.1 illustrates the considered domain, depicting the large differences in scale, along with the resulting meshes, with two larger open spaces of outflow with an interconnecting spacing comprised of a channel. The channel will be constructed in two different configurations: a duct with finite dimensions, and a duct with infinite width, resembling parallel plates. This will support the implementation of various geometrical features, including bends, branching features, constrictions, and pin-fins, to establish a rigorous foundation for evaluating the model's performance.

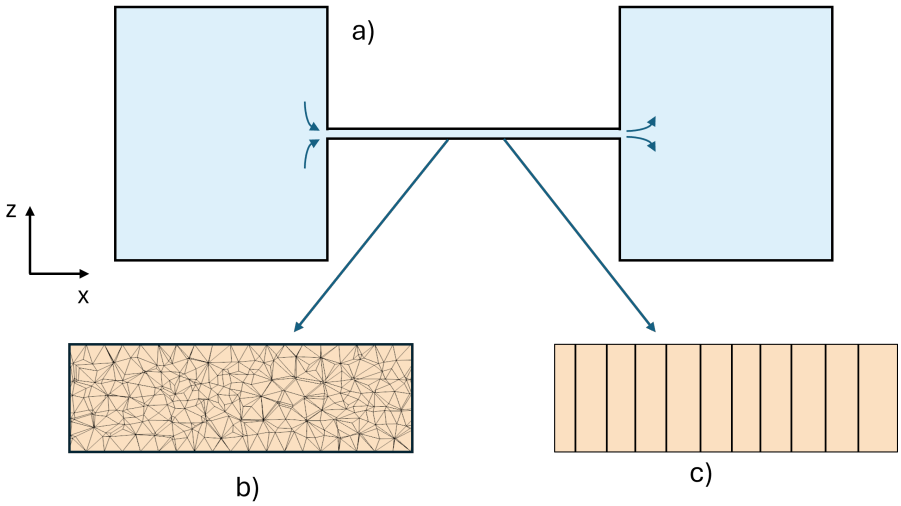

Figure 1.1: A simplified sketch illustrating the following aspects: a) the geometry and demonstrated flow path; b) unstructured 3D mesh in the *thin* subdomain; and c) *Pseudo 2D* mesh, all respectively viewed in an xz-plane.

The above figure also depicts the flow path of air, which will be simulated for Reynolds numbers below 100. This was decided to consistently maintain laminar steady-state conditions, for simplicity and conformity with the industrial application. In the applications serving as inspiration for this project, where geometries in the scale of micrometers are common, molecular-level gas movement and the Knudsen number become too significant to neglect. As a result, the continuum-based Navier-Stokes equations are commonly replaced by the Boltzmann equation to govern the fluid motion for sub-continuum physics [21]. However, for this project, the geometrical size will be enlarged and generalized. This will be done to enable application for various pressure-induced flows occurring within confined spaces of low Reynolds numbers for an extended range of applications such as heating, ventilation, and air conditioning (HVAC) as well as the automotive industry.

The motivation of the project from a larger perspective is represented by the following factors:

- **Deeper understanding for 2D-models:** By constructing a 2D model for flow between plates, the understanding of how reduced dimensional models compared to more detailed 3D models is enhanced. This can provide insight into when such a model is sufficient and when limitations exist.
- **Optimize Simulations:** By quantifying the savings in cell count, it is easier to get an understanding of how to utilize resources more efficiently for other similar problems. This is particularly important in cases where speed and resource efficiency are crucial.
- **Identify limitations and applications:** When comparing reduced dimensional models with a more detailed 3D model, limitations can be quantified for various factors such as geometry type or flow velocity. This can provide insights into the models applicability.

1.3 Goals and Objectives

The goals and objectives underpinning this project include:

- Development of reduced dimensional models, with one cell between the walls in the thin spacing.
- Validation of the models against full 3D simulations.
- Implementation of, e.g., field functions to assist the simplified model.
- Quantification of the savings in terms of cell count.
- Quantification of potential limitations in terms of performance and applicability of the reduced dimensional models.

2 Theory

This section addresses the physics, tools and the underlying background information necessary for the succeeding discussions. These aspects are presented concerning the flow features, transportation of fluid properties, quantifying measures, and previous works.

2.1 Literature Review

This section provides an overview of existing research and developed techniques relevant to the topic of reduced dimensional/order models and overall reduction of computational cost. This is highly relevant for the project conducted in this thesis and has served as an inspiration for the development of the models. On the topic of reduced dimensionality/order, Sun et al. [28] presents a way to transition from a three-dimensional model to a reduced planar model based on fully developed flow assumptions. A reduced planar model is a simplified two-dimensional representation of a system, decreasing the complexity of its three-dimensional nature. The paper discusses how to accurately analyze stacked plate heat exchangers in thermal energy storage systems for optimal performance. Due to the plate surface complexity, it is computationally expensive to make a full three-dimensional simulation. A reduced-dimensional model is utilized which is described by complex mathematical models and is an extension of that proposed by Alexandersen [2]. The reduced-dimensional model is extended to consider transient flows and works well for simulations between stacks of plates. This model displayed satisfactory results compared to the three-dimensional model while reducing computational cost.

Others like Haertel et al. [12] have used so-called "Pseudo 3D models". In this particular case the "Pseudo 3D model" was used for the optimization and simulation of finned heat sinks. The full 3D model was replaced with the "Pseudo 3D model" which is comprised of a 2D modeled conducting metal base layer and a thermally coupled 2D model representing the thermofluid design layer. Simulations were conducted in the study and the results showed strong agreement between the optimized model and the validation models, which confirms the validity of the "Pseudo 3D model". This demonstrates an indication of the applicability of these types of models.

The literature review has also been extended to provide a foundation of the topic of the flow present in this thesis project's simulations. The reviewed studies have extensively investigated steady laminar flows in sudden expansions, especially in the field of industrial processing applications. Experimentally sudden expansion flows have been the focus of several studies, e.g., those of Hung and Macagno [14], Macagno and Hung [18] and Durst et al. [8]. A study made by Baloch et al. [3] aims to investigate flows with low Reynolds numbers to maintain steady-state solutions, as higher Reynolds numbers lead to time-dependent, unsteady solutions. This study explores phenomena like separation and reattachment behaviors where different expansion ratios are considered.

This literature review highlights important aspects in terms of modeling simplification and reduction of computational costs in various applications. These insights resultingly contributed to the conceptual development of the reduced dimensional model

2.2 Computational Fluid Dynamics

Computational fluid dynamics (CFD) is the main tool used to analyze the fluid behavior in this project. It approximates equations that govern the motions of fluids. The steps required to analyze a fluid problem are the following: A mathematical formulation describing the fluid flow is written. This is done using partial differential equations. Secondly, these equations are discretized to obtain a numerical representation of the equations. In the third step, the domain is divided into system of small elements, often referred to as a grid system or mesh. The equations are then solved using initial and boundary conditions for the specific problem. A program to solve CFD problems consists of three main elements which can be divided following Zawawi et al. [31]:

- A pre-processor is used for inputting the desired geometry, generating the grid, and defining the boundary conditions.
- A discretization method is used to solve the governing equations of the problem. The discretization method can differ between applications. The most common examples are the finite element method, finite difference method, and the finite volume method. In this analysis, the finite volume method is employed.

- Lastly a post-processor, which is used to present the data and the different results of the simulation.

Computational fluid dynamics involves analyzing systems where heat transfer, fluid flow, and other types of phenomena occur through computer-based simulations. In this thesis, CFD was used to conduct numerous simulations to gain a better understanding of the gas flows within narrow gaps subject to sudden expansion.

2.3 Governing Equations

The governing equations that are used in CFD are based on the conservation law of physics and the equations of state. The conservation laws of physics state [29]:

- The total mass of a fluid element is conserved.
- The sum of the forces acting on a fluid element equals the change of momentum.
- The rate of change in thermal energy and the work that is done on a fluid element is equal to the total energy change for the element.

These, are called the conservation of mass, momentum, and energy and are the basis of the governing equation called the Navier-Stokes equations. The cases examined in this thesis assume isothermal and incompressible conditions. Resultingly, the energy equation is irrelevant and also decoupled from the mass and momentum equations. Thus, it is excluded as a governing equation. One of the first requirements that arises for the Navier-Stokes equations to apply is that the fluid is Newtonian, meaning that the viscosity is unaffected by the shear rate. The previous, in combination with the assumption of incompressible flow, yields the following relations:

2.3.1 Mass Equation

The equation of mass is based on the mass balance for the examined fluid. By comparing the rate of increase of mass in a fluid element to the net rate of mass flow into the fluid element, the mass equation can be formulated according to Equation (2.1) [29]:

$$\frac{\partial u}{\partial x} + \frac{\partial v}{\partial y} + \frac{\partial w}{\partial z} = 0. \tag{2.1}$$

Equation (2.1) can also be rewritten to a more compact vector notation form:

$$\nabla \cdot \mathbf{u} = 0, \tag{2.2}$$

where both forms are commonly interpreted as the divergence of the velocity vector.

2.3.2 Momentum Equation

The momentum equation is equivalent to Newton's second law. Herein the sum of forces on a fluid particle is equal to the rate of increase of momentum of the fluid particle [29]. Represented by vector form, the final equation becomes:

$$\rho \frac{D\mathbf{u}}{Dt} = \nabla \tau - \nabla p + S_M, \tag{2.3}$$

where S_M is the momentum source term, $\nabla \tau$ the stress components, ∇p the pressure gradient and $\rho \frac{D\mathbf{u}}{Dt}$ the product of mass and acceleration per unit volume.

2.4 Numerical Discretization

The finite volume (FV) discretization, discretizes a domain into a mesh that contains cells. In this method, the governing partial differential equations (PDEs) are integrated over a control volume. By applying Gauss' divergence theorem, the resulting volume integrals are converted into surface integrals. The fluxes on the faces of the control volumes are then calculated, making it possible to improve the exchange of mass and momentum between adjacent cells.

Equations (2.1) and (2.3) in Section 2.3 can also be written as a vector transport equation where a generic variable ϕ is introduced:

$$\frac{\partial \rho \phi}{\partial t} + \nabla \cdot (\rho \phi \mathbf{u}) = \nabla \cdot (\Gamma \nabla \phi) + S_\phi. \tag{2.4}$$

The generic variable ϕ can be substituted with transported variables, in this case mass (ρ) and momentum ($\rho\mathbf{u}$). Γ is a diffusion coefficient and S_ϕ the source term due to rate of increase of ϕ. The physical meaning of the different terms from Equation (2.4) are described as follows [29]: rate of increase of ϕ of fluid element + net rate of flow of ϕ out of fluid element = rate of increase of ϕ due to diffusion + rate of increase of ϕ due to sources.

To perform a finite volume discretization, the transport equation needs to be integrated over the three-dimensional control volume (**CV**) [29]:

$$\int_{CV} \frac{\partial \rho\phi}{\partial t} dV + \int_{CV} \nabla \cdot (\rho\phi\mathbf{u}) dV = \int_{CV} \nabla \cdot (\Gamma \nabla\phi) dV + \int_{CV} S_\phi dV. \tag{2.5}$$

Gauss's divergence theorem is applied and resultingly converts the volume integrals into surface integrals. The general form of Gauss's divergence theorem for a vector $\mathbf{a}$ can be seen in Equation (2.6).

$$\int_{CV} \nabla \cdot (\mathbf{a}) dV = \int_A \mathbf{n} \cdot \mathbf{a} dA, \tag{2.6}$$

where $\mathbf{n} \cdot \mathbf{a}$ is the component of vector $\mathbf{a}$ in the direction of vector $\mathbf{n}$, which is normal to the surface element dA. Applying Gauss's divergence theorem to Equation (2.5) results in Equation (2.7).

$$\frac{\partial}{\partial t}\left(\int_{CV} \rho\phi dV\right) + \int_A \mathbf{n} \cdot (\rho\phi\mathbf{u})\, dA = \int_A \mathbf{n} \cdot (\Gamma\nabla\phi)\, dA + \int_{CV} S_\phi dV. \tag{2.7}$$

The first term on the left-hand side describes the rate at which ϕ increases within the control volume and the second term illustrates the net decrease of ϕ through convection across its boundaries. The first term on the right-hand side represents the net increase of ϕ due to diffusion across the control volume boundaries and the second term describes the net generation of ϕ within the control volume.

2.4.1 Steady-State Problems

In steady-state problems, which will encompass the simulations in this project, the change in time is zero, because the properties in the system are constant over time. This makes the first term in Equation (2.7) redundant, which results in the following steady state transport equation:

$$\int_A \mathbf{n} \cdot (\rho\phi\mathbf{u})\, dA = \int_A \mathbf{n} \cdot (\Gamma\nabla\phi)\, dA + \int_{CV} S_\phi dV. \tag{2.8}$$

2.4.2 Transient Problems

Transient problems are time dependent problems, thus it is essential to integrate over a small time interval, Δt, from a starting time, t, to a slightly later time, $t + \Delta t$. Applying this to Equation (2.7) gives the following:

$$\begin{aligned}\int_t^{t+\Delta t} \frac{\partial}{\partial t}\left(\int_{CV} \rho\phi dV\right) dt + \int_t^{t+\Delta t} \int_A \mathbf{n} \cdot (\rho\phi\mathbf{u})\, dA dt = \int_t^{t+\Delta t} \int_A \mathbf{n} \cdot (\Gamma\nabla\phi)\, dA dt \\ + \int_t^{t+\Delta t} \int_{CV} S_\phi dV dt,\end{aligned} \tag{2.9}$$

where all variables are defined in Section 2.4 for both Equation (2.8) and (2.9).

2.4.3 Discretization Schemes

Since discrete values are stored at the cell centers, interpolation is necessary for handling convection and diffusion terms. The following sections outline the most frequently used schemes in CFD. In STAR-CCM+, the primary discretization schemes employed are upwind, second-order upwind and central differencing.

To illustrate how the different schemes are formulated, Figure 2.1 is used and depicts the adopted cell-related notations. Face values are denoted by lowercase letters and cell centers are named with uppercase letters. W, E, P stand for west, east and the cell center value of interest, respectively. The distance between the faces is assumed to be the same. For simplicity, the elements are assumed to be uniform but the same discretization schemes can also be applied for an unstructured mesh.

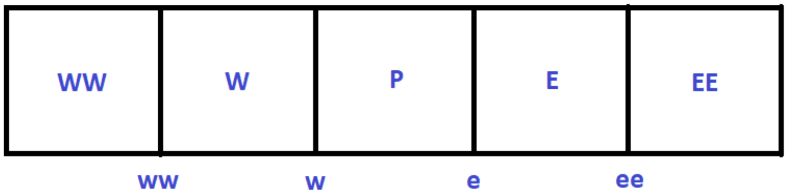

Figure 2.1: Illustration of cells and faces with quadrilateral elements.

2.4.4 Upwind

The upwind differencing scheme, also known as the "donor cell" differencing scheme, considers the direction of flow when calculating the value at a cell face [29]. It assigns the convected value of ϕ at a cell face to be the same as the value at the upstream node. With the adoption of the notations displayed in Figure 2.1, this means that when a flow has a direction from west to east, the upwind scheme becomes:

$$\phi_e = \phi_P \ , \ \phi_w = \phi_W .$$

This scheme is first-order accurate and relies on backward difference and is widely considered simple compared to others. As a consequence, a significant limitation is the entailing numerical diffusion, and also the susceptibility to false diffusion. The latter, discussed further by Versteeg and Malalasekera [29], is caused by a misalignment between the flow and grid system, resulting in inaccurate outcomes.

2.4.5 Second-Order Upwind

The linear upwind scheme can be viewed as a second-order equivalent of the previously discussed upwind scheme, with an added correction. The scheme incorporates an additional term which is the gradient of the upstream cell multiplied by the distance from the center of the upstream cell to the center of the face. A second order upwind differencing, with the notations from Figure 2.1, involving two upstream values yields the following for ϕ_e [29]:

$$\phi_e = \phi_P + \frac{(\phi_P - \phi_W)}{\delta x}\frac{\delta x}{2} = \phi_P + \frac{1}{2}(\phi_P - \phi_W) . \tag{2.10}$$

2.4.6 Central Differencing

The central differencing scheme calculates the value of a cell center by interpolating linearly between the two neighboring cell center values, east and west, which makes it second-order accurate. There are some instances where this scheme experiences stability issues due to it being susceptible to dispersive error. This is prominent in simulations based on Reynolds-averaged Navier-Stokes equations (RANS) for convective terms, where the central differencing scheme is not a suitable method. Despite having major drawbacks for flows with a high ratio between convective to diffusive transport rate (high Peclet number) [21], it performs well for large-eddy simulations (LES). The main reasons are that the turbulent kinetic energy is preserved when discretizing the convective term [24], and as the scheme is second order and free of numerical diffusion, it supports the sub-grid modelling used in large eddy simulations [16].

In STAR-CCM+, the central differencing scheme is defined as follows:

$$\phi_f = (f\phi_0 + (1-f)\,\phi_1) , \tag{2.11}$$

where ϕ_f is the face quantity and V the cell volume, while index 0 and 1 refers to the cells sharing the same face. f refers to the mesh stretching and is defined as $f = \frac{\Delta V_1}{\Delta V_0 + \Delta V_1}$. For a uniform grid $f = 0.5$, the face property ϕ_e according to Figure 2.1 can be written as [29]:

$$\phi_e = \frac{(\phi_P + \phi_E)}{2} . \tag{2.12}$$

2.4.7 Temporal Discretization

Time becomes an additional dimension for transient simulations. It is divided into small time steps, similar to the division in space. Solving the governing equations involves calculating a solution at

various time steps, where each solution at time t requires solutions from one ore more previous time steps.

The Euler implicit-scheme, which is a first order temporal scheme, approximates the transient term in semi-discrete transport equations as follows [24]:

$$\frac{\partial}{\partial t}\left(\rho\phi\Delta V\right) \approx \frac{\left(\rho\phi\Delta V\right)^{n+1} - \left(\rho\phi\Delta V\right)^{n}}{\Delta t}. \tag{2.13}$$

Here, $n+1$ denotes the solution at the current time step and n the solution from the previous time step.

For a basic second order temporal discretization, the current time step is used, $n+1$ as well as the previous, n and the solution from two previous time steps, $n-1$. The second order temporal discretization is defined as follows [24]:

$$\frac{\partial}{\partial t}\left(\rho\phi\Delta V\right) \approx \frac{\frac{3}{2}\left(\rho\phi\Delta V\right)^{n+1} - 2\left(\rho\phi\Delta V\right)^{n} + \frac{1}{2}\left(\rho\phi\Delta V\right)^{n-1}}{\Delta t}. \tag{2.14}$$

In addition to the schemes described above, there are numerous others of higher order or with different constructions, examples of some of these schemes can be found in Huynh et al. [15]. These schemes are adequate for providing the reader with a fundamental understanding of CFD methods, particularly concerning this thesis.

2.5 Flow Between Plates and Confined Spaces

In this section, fundamental information regarding flow dynamics between plates and confined spaces such as ducts is presented. Concepts that are explained in this section are hydraulic diameter, Reynolds number, wall-boundary conditions, hydrodynamic entrance length, and head losses. These fundamental principles give valuable insights into the fluid behavior which is essential for the subsequent analysis.

2.5.1 Hydraulic Diameter

Hydraulic diameter is a characteristic length used in many engineering applications when analyzing flows in non-circular channels and tubes. The hydraulic diameter is calculated using the following formula, which is described by Embiale et al. [9]:

$$D_h = \frac{4A}{P}, \tag{2.15}$$

where A is the duct cross sectional area and P the perimeter of the geometry. For a rectangular duct, the hydraulic diameter becomes:

$$D_h = \frac{2ab}{a+b}. \tag{2.16}$$

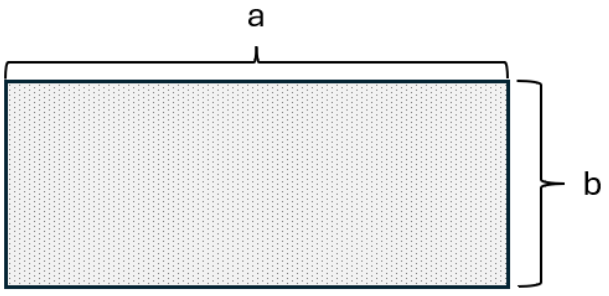

Figure 2.2: Rectangular duct.

Here, a is the width of the duct and b the height of the duct. In the case of an infinitely wide duct, e.g., in the span-wise direction where $a \gg b$, the hydraulic diameter is given by:

$$D_h = \lim_{a\to\infty} \frac{2ab}{a+b} = 2b. \tag{2.17}$$

2.5.2 Reynolds Number

The Reynolds number is a dimensionless number widely used in the analysis of fluid dynamics. Dimensionless quantities aids the removal of dependencies on specific geometrical parameters and the overall scaling of different cases. The explanation found in this section resembles that of Rapp [21]. It is most often used to determine the type of flow regime and by extension the applicability of governing mathematical and numerical concepts. The physical interpretation can be expressed as the ratio between the forces of inertia and the viscous forces, in mathematical terms:

$$Re = \frac{\rho U L_{char}}{\mu},$$

where ρ, U, L_{char} and μ are the density, velocity, characteristic length, and the dynamic viscosity of the fluid, respectively. In internal flow analysis, particularly in the discussion of pipes or ducts the characteristic length is often referred to or replaced by a hydraulic diameter D_h, see Section 2.5.1. This results in the finalized format of the Reynolds number used in this analysis:

$$Re = \frac{\rho U D_h}{\mu}. \tag{2.18}$$

Small values of Re indicate that the viscous forces are predominant and for large values, the inertial forces become the main driving agent of the fluid. Laminar flows are governed by the viscous forces such that the acceleration of the fluid is sufficiently small, i.e., small Re. Conversely, turbulent flows are dominated by inertia and cause instabilities in the flow field, i.e., large Re. In this thesis, the critical Reynolds numbers governing laminar-to-turbulent transition experimentally deduced by Chang et al. [5] are adopted. For flow between parallel plates, considered for an infinitely wide duct, the critical Reynolds number is:

- $Re <\sim 2689$.

Correspondingly, with an aspect ratio of $b/a = 1/1.5$ for the duct, the cross-sectional area-dependent critical value becomes:

- $Re <\sim 1200$.

2.5.3 Wall Boundary Conditions

The employment of various wall boundary conditions proved to be highly essential for the development of the reduced dimensional model and the need to theoretically clarify the conditions thus became evident. The two conditions employed as wall boundary conditions are the no-slip boundary condition and the slip boundary condition. The first, states that the velocity at the walls is assumed to be zero. The speed of the fluid layer that directly touches the boundary matches the boundary itself, resulting in no relative movement between the boundary and the fluid layer [21]. Resultingly, a parabolic velocity profile is formed. The second, the slip condition, assumes that the fluid and the wall experience a relative movement. This means that for perfect slip conditions, which are assumed, the shear stress between the fluid and the wall is zero [4]. Ultimately, this results in a planar flow front equal to the inlet boundary condition. For visualization of both boundary conditions see Figure 2.3.

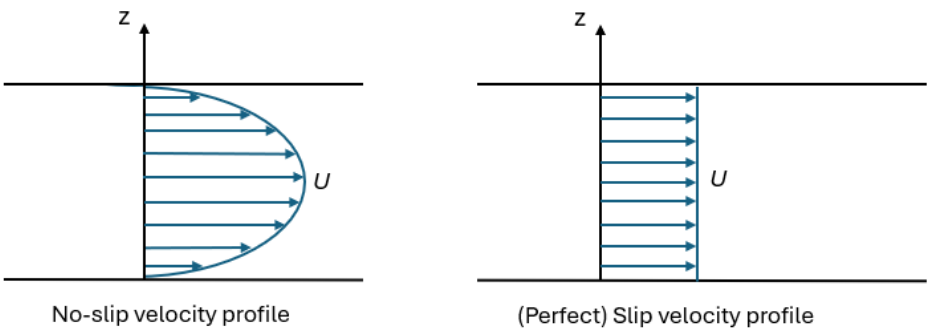

Figure 2.3: Illustration of the difference between the no-slip and (perfect) slip condition for a velocity profile.

2.5.4 Entrance Length

The hydrodynamic entrance length is of importance in CFD applications. As described by Okiishi et al. [7], the hydrodynamic entrance length is the distance over which the flow profile in a channel transitions from the inlet to a region where the flow is fully developed. When a fluid enters a channel there is initially a behavior of unsteadiness until it reaches the entrance region. At this point, the flow achieves a near-uniform state, leading to a uniform velocity distribution. As the fluid flows through the channel, viscous effects cause it to stick to the channel walls, which is known as the no-slip condition, see Section 2.5.3. A boundary layer is then formed along the channel, changing the velocity profile until the fluid reaches the end of the entrance region and transitions to the fully developed region. In this domain, the velocity profile becomes fully established and does not change further as the fluid moves along the channel, see Figure 2.4.

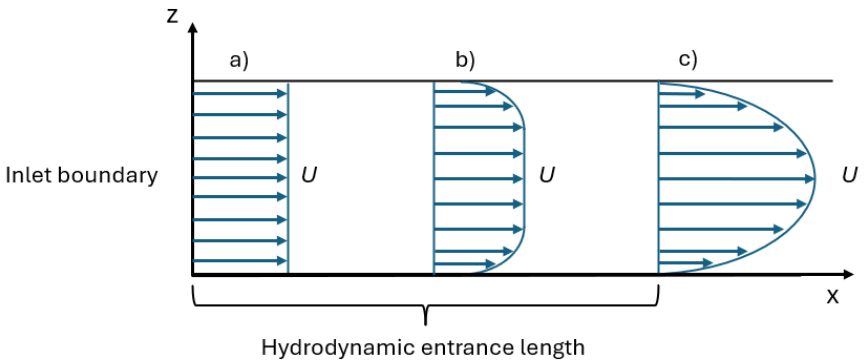

Figure 2.4: The velocity profile of various developing stages: a) velocity profile at the inlet; b) developing velocity profile; c) fully developed velocity profile.

The hydrodynamic entrance length L_e, is a function of the Reynolds number Re, and the hydraulic diameter D_h. Thus it is dependent on the flow velocity and the channel size. In the case of laminar flow, the entrance length is expressed by Equation (2.19):

$$L_e = 0.06 \cdot Re \cdot D_h. \tag{2.19}$$

2.5.5 Head Loss in a Confined Domain

The forthcoming discussion is relevant to this thesis, as it addresses the origin of one of the main result features later observed: the pressure distribution throughout the domain. Following the theory established by Young et al. [7], the discussion aims to clarify the contributing aspects to pressure drop throughout a confined space. In the mentioned literature the classification of losses in terms of major and minor ones is initially presented. The first includes the (head) loss due to the viscous friction-related effects of the fluid flowing in straight geometries, and the latter, the (head) loss due to the changes in geometry. Further, drawing from the discussion by Nguyen et al. [20] on laminar flows; the minor losses are commonly formulated as comprised of a loss coefficient, $\xi(Re)$ and a factor proportional to U^2. This ultimately demonstrates that the loss is largely velocity-dependent. The contributions stemming from various geometrical components vary in significance for the later analyzed cases and are addressed respectively in each section.

Additionally, the pressure drop for larger than micro scale flows has been found by Moody [19] to be unaffected by the roughness of the surface of the confining walls for laminar flows. This justifies the modeling of assumed infinitely smooth walls for all the laminar simulations.

2.6 Laminar Jets

The phenomenon that is formed due to the presence of the sudden geometrical expansion and thereby flow separation, is a laminar jet. It governs the essential resulting velocity image in the larger spacing beyond the channel flow. The theory serving as foundation for this is thus highly relevant for the remaining result feature: the velocity of the fluid in the sudden expansion, which is discussed in this section.

For laminar jets in sudden expansions, the solution becomes time-dependent and unsteady for

higher Reynolds numbers. In a study conducted by Hajji et al. [13], Reynolds numbers up to $Re = 40$ were examined in steady-state simulations. Another study covered Reynolds numbers ranging from $1 \leq Re \leq 75$ for 2D simulations and $10 \leq Re \leq 200$ for 3D simulations [3]. The study also demonstrated that the flow starts experiencing oscillatory behaviors at Reynolds numbers exceeding 50 for both the 2D and 3D simulations. This suggests that the jet in the expansion region becomes unsteady at low Reynolds numbers, even if the jet is laminar. These oscillations likely arise due to an instability known as Kelvin-Helmholtz instability. Following an explanation proposed by Lee and Kim [17], the phenomena occurs at the interface between two fluid layers of different velocities (or densities). In the case of jet formation due to sudden expansion, the jet of air moving through the surrounding air creates a velocity difference at the interface. When the velocity difference between the static fluid and the jet is sufficiently high and overcomes the destabilizing effect of surface tension, the Kelvin-Helmholtz instabilities start to develop, characterized by the formation of rolling vortices or waves along the interface. These instabilities have also been claimed by Fletcher et al. [11] to be highly dependant on the conditions of the nozzle and by equivalence for this study, the channel to room expansion. Herein, a Reynolds number of $Re = 90$ is presented to provide stable results.

In conclusion, the studies referenced shed light on the dynamic and unpredictable behavior of laminar jets in sudden expansions, particularly concerning the tendency of unsteadiness and oscillatory behavior at higher Reynolds numbers. While the literature suggests that even as low Reynolds numbers as $Re < 50$ may lead to the onset of what is believed to be Kelvin-Helmholtz instabilities, the conducted analysis indicates that stability and steadiness can be safely assumed and achieved for Reynolds numbers up to $Re = 100$. As mentioned previously, it is important to note that the stability and steadiness of such jets may still be influenced by various factors including channel or nozzle geometries, as highlighted by Fletcher et al. [11].

3 Computational Setup and Method

This section details the configuration of the initial computational domain of the *Simple Geometry* case. This later served as the domain of the development of the reduced dimensional model. The section also covers the boundary conditions, physics, and solver settings used in the simulations. The construction and setup of the meshes are described, including details of the mesh configurations, volumetric controls, and specific meshing techniques. Lastly, a mesh sensitivity analysis was performed to ensure an accurate representation of the solution while maintaining optimal computational efficiency.

3.1 Computational Domain - Simple Geometry

The initial aim was set on constructing a simple geometry for the development of *Pseudo 2D* model, which denotes the initial uncorrected version of the reduced dimensional model. The *Simple Geometry* was created to serve as a reference for the reduced dimensional model, as well as a foundation for the later implemented geometrical features. It was constructed to conform with the initial sketch motivating this project, see Figure 1.1. Nonetheless, levels of generality were still intended, due to the purpose of the study being applicable for multiple applications and fields. Below are the geometry and resulting dimensions of the *Simple Geometry* case for both the parallel plate and duct configurations:

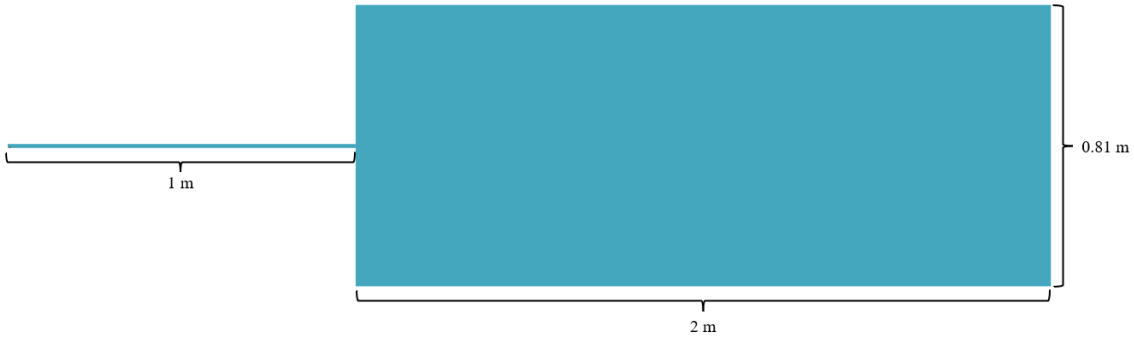

Figure 3.1: Dimensions of analyzed geometry, xz plane (parallel plates and duct).

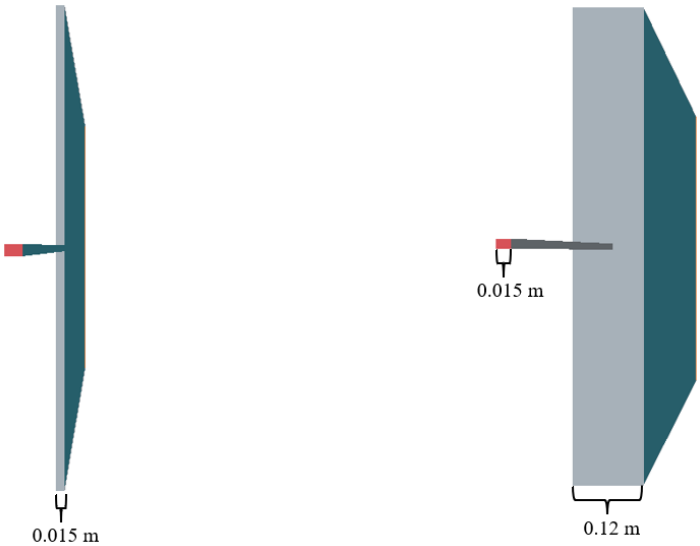

Figure 3.2: Dimensions of analyzed geometry, side view (parallel plates and duct, respectively).

Figure 3.3: Channel height in xz plane for parallel plates and duct.

The construction of the geometry was performed based on fulfilling the following criteria:

- The channel subdomain should be long enough such that a fully developed flow can be attained for a wide range of inlet and gas conditions. The height and length were set to $0.01\,m$ and $1\,m$ respectively, see Figure 3.1 and 3.3, resulting in an aspect ratio of $1:100$. Thus, conforming with the corresponding encountered in the semi-conductor industry.

- The aspect ratio between the channel height and the height of the room should be large enough to fully capture the flow entering the room subdomain. This allows proper accommodation of the jet without interference from any walls and enables observation of the outflow from the channel.

- The flow after the transition between the subdomains of the channel and the room should be able to fully develop without being affected by the boundaries of the latter. This condition was fulfilled in an iterative manner, where the domain of the room was expanded in both the main flow direction, but also in the direction perpendicular to the flow for both the *3D* and *Pseudo 2D* model. In later simulations involving ducts, the third depth dimension, y, was similarly expanded for these geometries. For cases containing parallel plates, it was necessary to have the channel and room subdomains of the same width, since the concept of an infinitely wide channel subdomain thus must align with the notion of an equally wide or wider room. This was no issue for the low range of Reynolds numbers analyzed, as it did not influence the steadiness of the jet. The two main aspects under consideration during this process were maintaining a small enough domain to limit the computational cost while still preserving the required space for the outflow without it being obstructed by, e.g., undesired back-flow. After several attempts, the dimensions of the room for the *Simple Geometry* were established as $0.81\,m$ for the height, and $2\,m$ for the length, see Figure 3.1. For the studies regarding the modeling of parallel plates, the y-dimension was set to $0.015\,m$ for the channel and the room subdomains. However, in the studies focusing on duct modeling, the channel subdomain maintained a depth of $0.015\,m$, while the room subdomain's depth was set to $0.12\,m$, see Figure 3.2. Furthermore, to avoid large levels of potential non-laminar flow and jet instabilities, in the room, the inlet velocity was set significantly below the Reynolds number threshold for unstable jets. For a more detailed description of this, see Section 2.6. As mentioned in Section 1, this also conforms with the industrial application serving as inspiration for this project. The resulting aspect ratio was set to $1:81$.

- To initially consider the simplest possible flow-case, steady-state laminar, imposed some constraints to the inlet velocity and the geometry in terms of Reynolds number. This resulted in the inlet velocity, and bulk velocity, being $0.02\,m/s$ for the parallel plate geometries to maintain low local Reynolds numbers in both subdomains so that the flow can be infallibly considered as laminar and steady. The prior approach was solely determined by the constraints imposed by the undesired jet instabilities. This led to the following Reynolds number for the channel:

$$Re = \frac{\rho U D_h}{\mu} = \frac{\rho u_b 2h}{\mu} = \frac{1.184 \cdot 0.02 \cdot 2 \cdot 0.01}{1.855 \cdot 10^{-5}} \approx 25, \tag{3.1}$$

  with the properties of air taken at approximately $25\,^{\circ}\mathrm{C}$ atmospheric pressure, for the density ρ, dynamic viscosity μ, bulk velocity u_b and hydraulic diameter D_h. Subsequently, the hydraulic entrance length was computed using Equation (2.19), which gives:

$$L_e = 0.06 \cdot 25 \cdot 2 \cdot 0.01 = 0.031\,m. \tag{3.2}$$

  To maintain consistency between the two types of considered geometries, the inlet velocity for configurations involving ducts was determined based on the Reynolds number for parallel plates, i.e., $Re \approx 25$. Using the Reynolds number equation together with the equation for hydraulic diameter, see Equation (2.17), resulted in an inlet velocity of $0.033\,m/s$. Additionally, the hydraulic entrance length was calculated using Equation (2.19), which led to the following:

$$L_e = 0.06 \cdot 25 \cdot \frac{2 \cdot 0.015 \cdot 0.01}{0.01 + 0.015} = 0.018\,m. \tag{3.3}$$

3.2 3D Model - Boundary Conditions

Figure 3.4 is used to visualize the various boundaries in the *Simple Geometry* scenario for both the parallel plate and duct models.

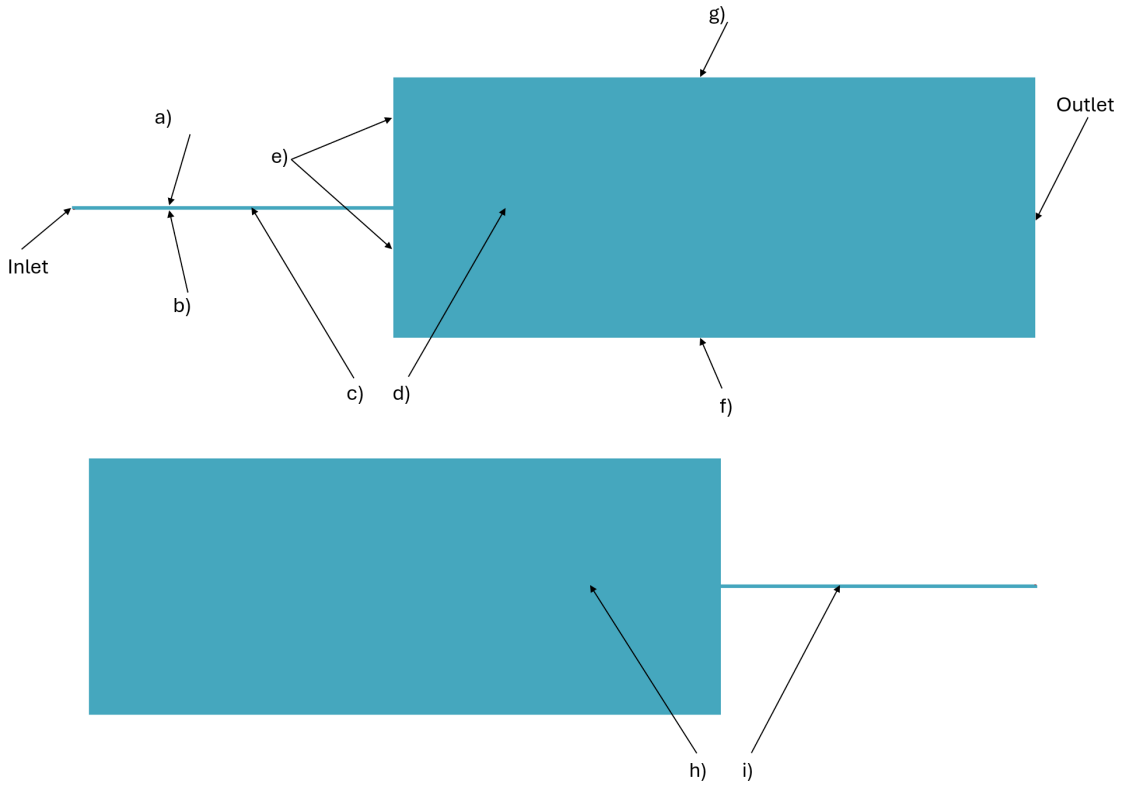

Figure 3.4: Boundary names in the xy plane for the front side (top) and back side (bottom), respectively.

The set boundary conditions for the *Simple Geometry* are presented in Table 3.1.

Table 3.1: Type of boundary conditions for *Simple Geometry* for parallel plates.

Boundary	**Condition**
Inlet	Velocity Inlet
c, d, h, **i**	Symmetry Plane
a, b, e, f, g	Wall, No-Slip
Outlet	Pressure Outlet

In the initial setup, the velocity inlet was set to $U = 0.02\,m/s$, as previously mentioned, while the pressure outlet was maintained at a static (relative) pressure of $p = 0\,Pa$ to imitate atmospheric conditions.

Symmetry boundary condition assumes that the same physical processes exist on both sides of the boundary and are described in more detail by Denton and Hu [6]. The choice of using the symmetry boundary condition was motivated by the fact that the geometry is considered to be infinitely wide but also fully uniform and thereby symmetrical. However, the specified wall boundary condition is set to the no-slip condition, see Section 2.5.3. The choice of using this boundary condition for the channel walls/plates was motivated by the fact that the plates are considered stationary, featuring a Poiseuille flow. Additionally, the room subdomain was considered large and stationary, serving as the outlet of the flow.

The boundary conditions for the *Simple Geometry*, when the channel is regarded as a duct, are outlined in Table 3.2.

Table 3.2: Type of boundary conditions for *Simple Geometry* for ducts.

Boundary	**Condition**
Inlet	Velocity Inlet
d, h	Symmetry Plane
a, b, **c**, e, f, g, **i**	Wall, No-Slip
Outlet	Pressure Outlet

The difference between Table 3.1 and 3.2 is that the symmetry boundary condition was applied for the parallel plate scenario within the channel, while the no-slip boundary condition was employed for the duct cases. This is highlighted by the bold-faced letters "**c**" and "**i**", representing the channel wall boundaries comprising the height dimension. The reason for this is that the depth is assumed to be infinite for the parallel plate case, which means that it is symmetrical and the same physical processes exist on both sides of the boundary. For the duct scenario, viscous effects are present in all faces of the channel, except the inlet. This means that viscous effects are present along the depth and height, leading to the implementation of the no-slip condition on the faces that were considered symmetrical in the parallel plate analysis. This adjustment accounts for the relative motion between the boundary and the fluid layer within the channel.

3.3 Physics Modeling and Solver Settings

The last unaddressed aspect, serving as a prerequisite for CFD simulations, is the incorporated physics. The following settings, displayed in Figure 3.5, were used to model the physics continuum:

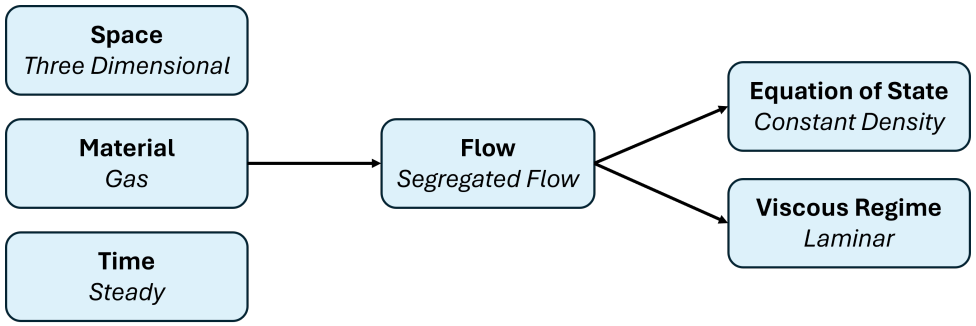

Figure 3.5: A flow chart illustrating the physics continuum settings in STAR-CCM+.

Herein, the gas was set as air. Incompressible flow and constant density were initially assumed, as they align well with the approach to attain simple flow characteristics as well as the targeted industrial applications. The velocities observed in the domain are significantly lower than the threshold for where gases are considered compressible, Mach number ≈ 0.3 [25], thus justifying the simplifying assumption.

3.4 Mesh

The construction and setup of the meshes, both the reduced dimensional model and *3D*, were done concurrently, ensuring that some of the constraints of the reduced dimensionality were accounted for in both meshes. An example of this was to verify that the mesh in the room attained high conformity between the two models without negatively impacting, e.g., element quality and the mesh transition between the two sub-domains.

3.4.1 3D Model

A mesh study was conducted for the *Simple Geometry* of the parallel plates, for the 3D mesh. This was done to obtain a mesh-independent solution, as well as a balance between accuracy and computational efficiency. The resulting chosen mesh was later implemented in the *3D* model, which in turn served as verification to the reduced dimensional models. The former was also of value for quantification reasons, such that the comparison between the reduced dimensional model and the full *3D* model is performed without bias in terms of computational resources.

The construction of the grid system and the study were carried out by implementing different volumetric controls and decreasing the mesh size within those volumetric controls. The elements used in the mesh are of tetrahedral type for both the room and channel subdomains. In the channel, five inflation layers, referred to as prism layers in STAR-CCM+, were applied to the walls. This was to ensure a precise representation of near-wall features and maintain the y^+ value, which is the dimensionless distance from the wall to the first grid point, within acceptable limits. However, due to the relatively low Reynolds number for all simulations, sufficiently accurate results can be achieved without specific near-wall treatment. The resulting choices for the *Automated Mesher* are displayed in Figure 3.6.

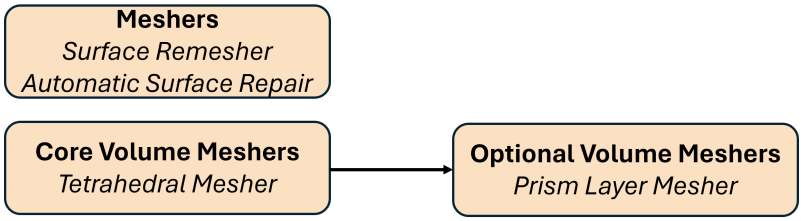

Figure 3.6: A flow chart illustrating the mesh configuration in STAR-CCM+ for *3D* model.

Three volumetric regions were implemented on the mesh, serving as cell-size controls. The initial control extended from the channel to half of the room. The second control spanned from the room entrance to half of the room but covered a larger area in the room compared to the first volumetric control. The third control covered a big part of the remaining room subdomain. These were denoted as: *VC-CA* (volumetric control channel A), *VC-CR* (volumetric control channel-room), and *VC-R* (volumetric control room), conforming with the above order. The objective was to accurately capture the flow in the channel and the resulting jet, hence the use of volumetric controls. They were also implemented to make sure of a smooth transition between smaller element sizes to bigger ones, especially in the vicinity of the sudden expansion. Seven meshes were generated with a base size of 0.05 m with varying volumetric control settings, each set as a percentage of the base size. Table 3.3 illustrates the mesh settings for the different volumetric controls and Table 3.4 shows the number of cells for the different mesh configurations.

Table 3.3: Volumetric control settings for different mesh types.

Mesh Type	**Base Size**	***VC-CA***	***VC-CR***	***VC-R***
mesh1	0.05m	9%	18%	72%
mesh2	0.05m	6%	12%	48%
mesh3	0.05m	4.5%	9%	36%
mesh4	0.05m	3%	6%	24%
mesh5	0.05m	2.5%	5%	20%
mesh5.5	0.05m	2.25%	4.5%	18%
mesh6	0.05m	2%	4%	16%

Table 3.4: Number of cells for different mesh types.

Mesh Type	**Number of cells: channel**	**Number of cells: Total**
mesh1	27 690	340 847
mesh2	70 838	579 959
mesh3	134 260	886 432
mesh4	342 457	2 025 383
mesh5	539 311	3 197 726
mesh5.5	723 562	4 126 512
mesh6	987 266	5 437 440

Figure 3.7-3.8 illustrates the meshes: the coarsest mesh with 340 847 cells; and the finest one with 5 437 440 cells.

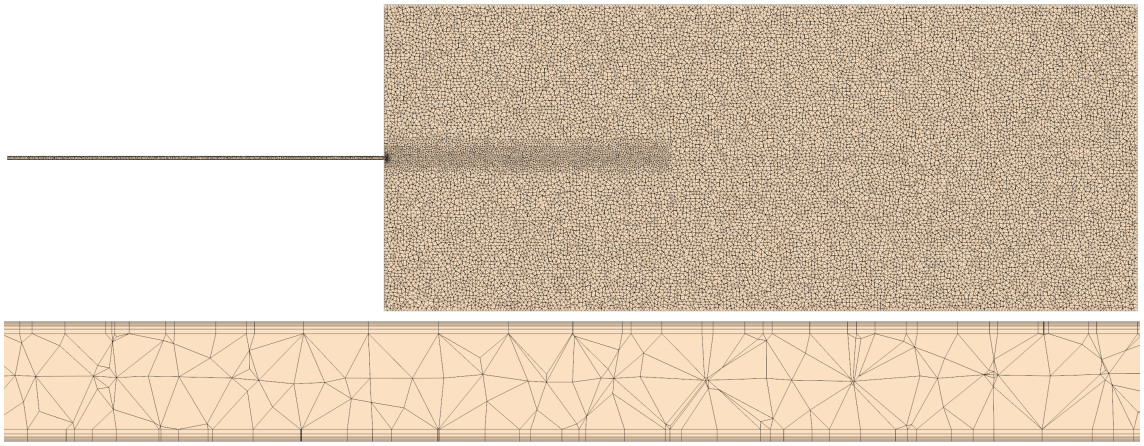

Figure 3.7: mesh1, internal mesh in xz plane for full mesh and channel.

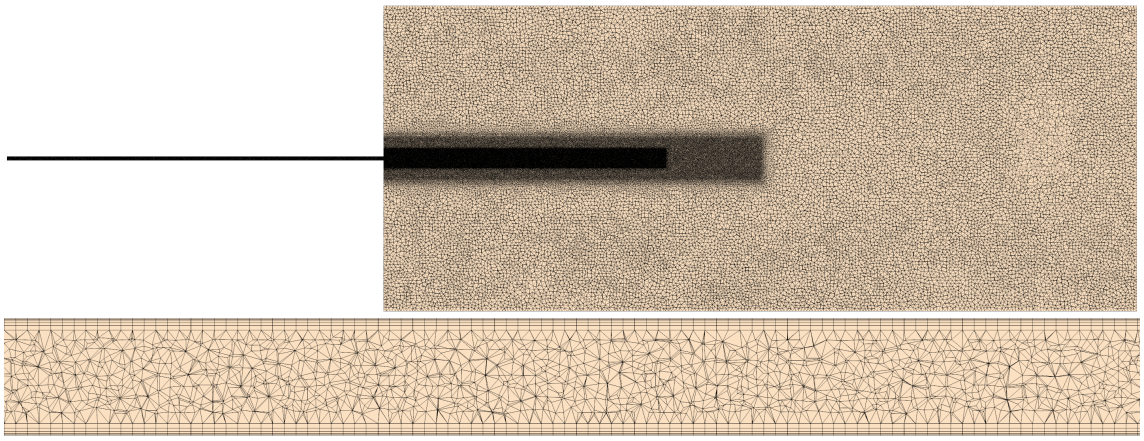

Figure 3.8: mesh6, internal mesh in xz plane for full mesh and channel.

3.4.2 Pseudo 2D Model

The construction of the mesh for the *Pseudo 2D* model, was performed concurrently with its *3D* counterpart, as mentioned. The enforcement of one cell in height along the channel limits the choice of meshers to *Tetrahedral Mesher* and *Thin Mesher* with the *Automated Mesher* as a predecessor. Consequently, to avoid bad mesh transitions, the grid-system type of the latter subdomain was permitted to comprise a small section of the channel in the near region of the sudden expansion, see Appendix A. The mesh configuration of the *Automated Mesher* is displayed in Figure 3.9.

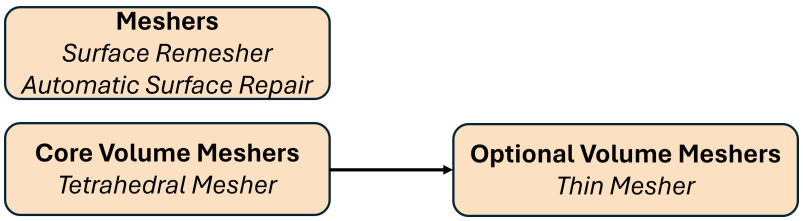

Figure 3.9: A flow chart illustrating the mesh configuration in STAR-CCM+ for *Pseudo 2D* model.

The other aspects and features of the *Pseudo 2D* model, mostly in terms of the latter subdomain, were constructed as similarly as possible to the mesh of the *3D* model. This was to provide as much of the mesh independence achieved from the preceding mesh sensitivity study and conformity between models.

3.5 Mesh Sensitivity Analysis

The overall mesh is based on an unstructured algorithmic generation approach. Thus, in the sense of quantifying the mesh convergence, no direct measurement or index is employed. Instead, plots and chosen data values throughout the domain are used in the analysis of the mesh convergence.

To ensure that the results are mesh-independent, different grid system types were evaluated and analyzed. The physics and solver settings used for conducting the simulations regarding the sensitivity analysis are described in Section 3.3. Since the regions of interest are comprised of the channel and jet, a specific focus was placed on analyzing results within these areas. Pressure distribution along the channel, shown in Figure 3.11, was examined using values obtained at the channel center line along the flow direction, see Figure 3.10. Furthermore, the velocity magnitude in the flow direction was analyzed along the entire domain and is represented by the a-line in Figure 3.10. Additionally, the velocity profile spanning the height dimension in the channel was analyzed. This was captured, orthogonal to the flow direction, just before entering the room, along the b-line in Figure 3.10. All this was done on the *Simple Geometry* for the flow between plates. Comparisons with the exact solution of the Poiseuille show the differences among the different mesh types which are illustrated in Figure 3.13.

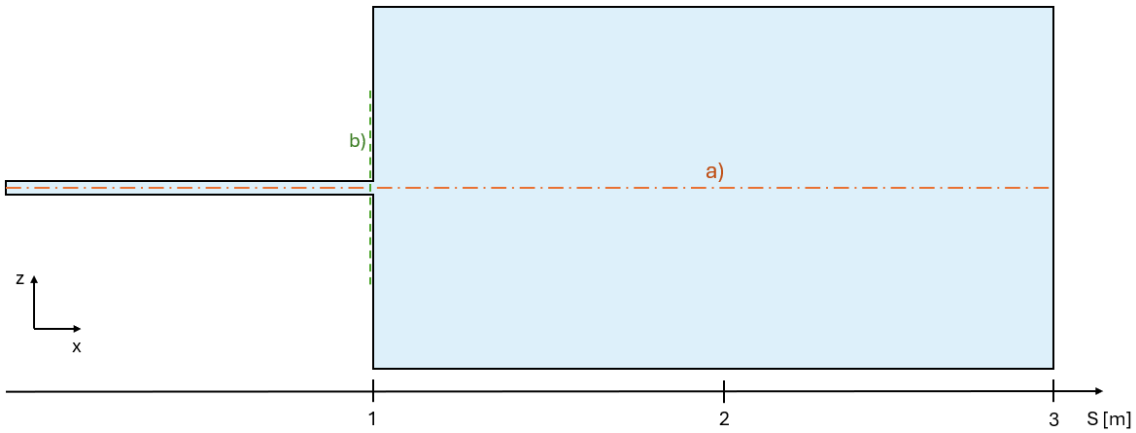

Figure 3.10: A sketch illustrating where the datasets are taken from: a) Position along center-line s; b) position between the plates z, before entering the room subdomain. Both views are in the xz-plane.

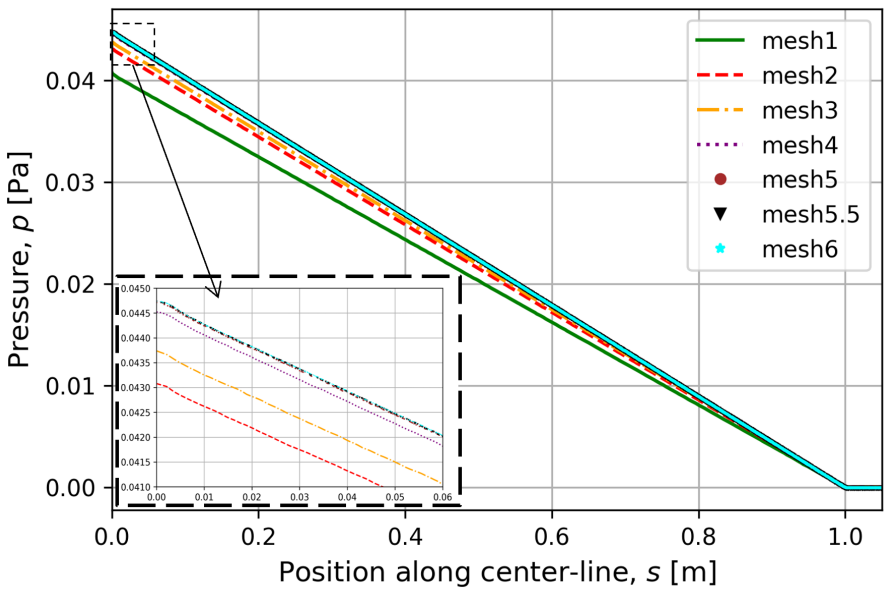

Figure 3.11: Pressure p along channel and a small section of the room.

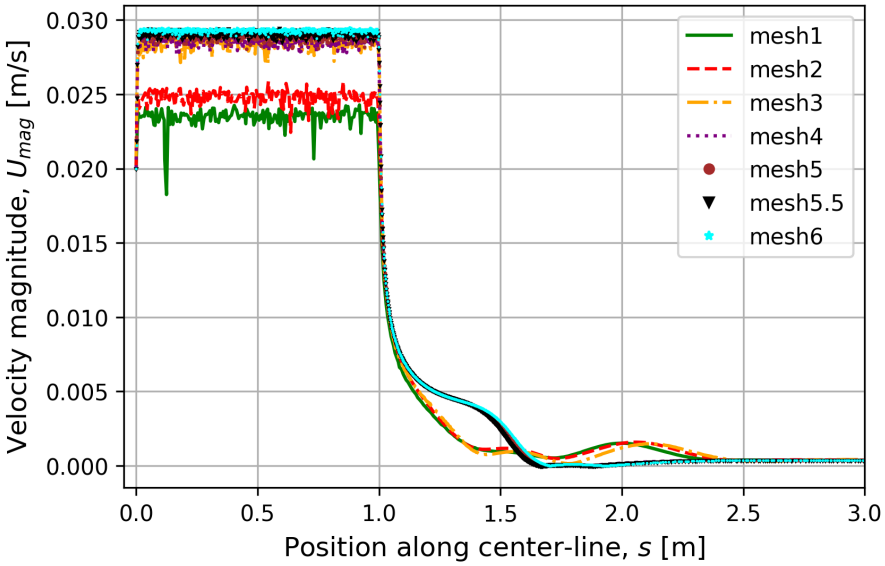

Figure 3.12: Velocity magnitude U_{mag} along domain.

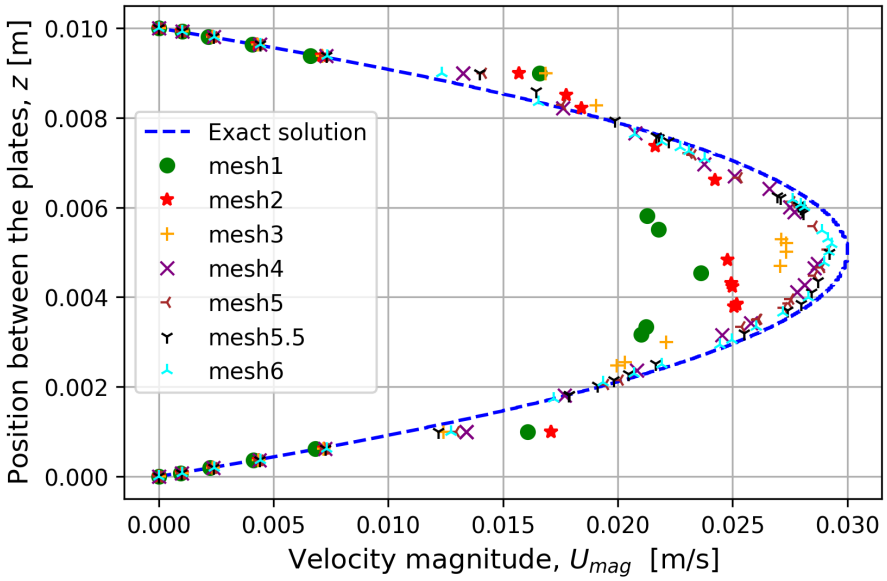

Figure 3.13: Velocity magnitude U_{mag} between plates $0.01\,m$ before entering the room subdomain.

To ensure result convergence, assessments were made on regions of importance for the different meshes. These assessments included evaluating the above plots, such as the pressure drop in Figure 3.11, and the maximum velocity normal to the flow direction at distances of $0.01\,m$ and $0.05\,m$ beyond the channel exit, in the room. The data regarding the former are shown in Figure 3.14-3.15.

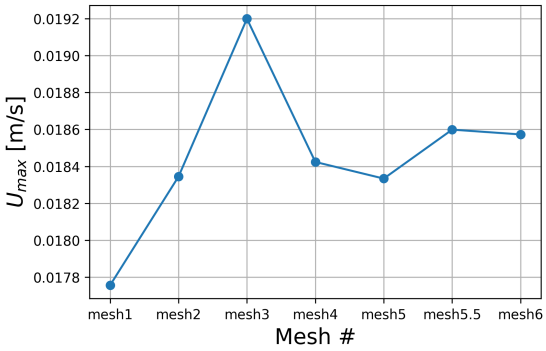

Figure 3.14: Maximum velocity U_{max} at $1.01\,m$.

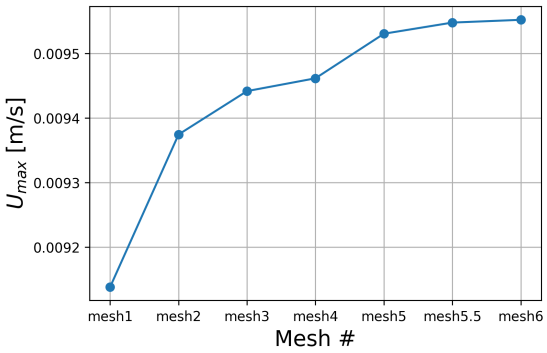

Figure 3.15: Maximum velocity U_{max} at $1.05\,m$.

In CFD (analyses), it is important to have a balance between computational cost and accuracy. Having a coarse mesh can result in inaccuracies due to poor resolution of flow features. On the other hand, an excessively fine mesh can result in a significant increase in computational time without necessarily improving the solution.

In this thesis, the evaluation between the different meshes indicated that mesh5.5, seen in Figure 3.16, offers the best results, considering accuracy and computational time. This was based on the observation of the consistent decrease in change between the finer meshes, indicating convergence. However, both mesh4 and mesh5 displayed sufficiently good results, but choosing mesh5.5 was justified by the reason that the analyzed problem was of a steady-state nature which results in manageable and acceptable computational time. Despite the higher computational expense associated with simulating this mesh compared to coarser ones, the decision to proceed with it was supported by the need to ensure strictly accurate results. Since other geometrical features were to be evaluated in this project, choosing a fine mesh was concluded to ensure that the same configuration would be sufficient.

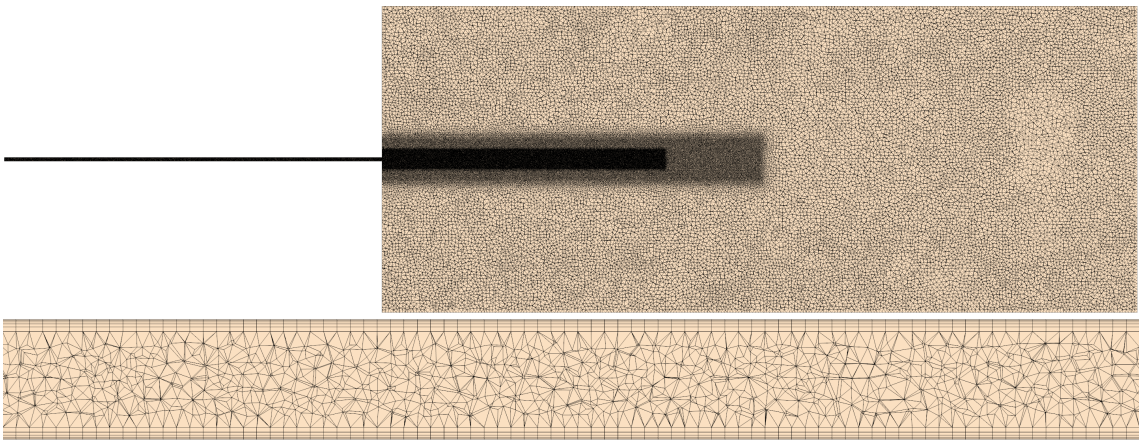

Figure 3.16: mesh5.5, internal mesh in xz plane for full mesh and channel.

3.6 Mesh Generation - Duct

To achieve a stable, converged steady-state solution, the room subdomain had to be widened in the duct models to ensure full accommodation of the three-dimensional jets forming. Since the room subdomain was significantly extended compared to the parallel plate models, the mesh settings had to be adjusted so that the maintained mesh count was reasonable. Changes to the volumetric controls were made. First, the *VC-CA* volumetric control was reduced, it now extended from the channel to a quarter of the room because it was evident that the jet did not extend beyond one-fifth of the room in the flow direction. The other volumetric controls, the *VC-CR* and the *VC-R* spanned the same length downstream compared to the parallel plate case but were extended in the depth direction, conforming with the widening of the room subdomain. The size of the volumetric controls was adjusted to maintain sufficient accuracy while simultaneously reducing the total cell count. Table 3.5 illustrates the mesh size for the different volumetric controls as a percentage

of the base size and Table 3.6 shows the number of cells in the channel and the whole domain respectively.

Table 3.5: Volumetric control settings for *Simple Geometry* - Duct.

	Base Size	***VC-CA***	***VC-CR***	***VC-R***
***Simple Geometry* - Duct**	0.05m	2.5%	6%	18%

Table 3.6: Number of cells for *Simple Geometry* - Duct.

	Number of cells: channel	**Number of cells: Total**
***Simple Geometry* - Duct**	629 116	6 541 842

4 Development of Reduced Dimensional Model

This section presents the general theory of the Poiseuille flow, detailing how it is derived for the configuration of parallel plates and ducts respectively. The theoretical pressure drops were calculated for both cases and served as benchmarks for the simulated results. The theoretical pressure drop between two parallel plates with one cell between the plates was also computed. Lastly, the implementation of the *momentum source*, to artificially correct the pressure in the reduced dimensional model, is detailed.

4.1 Poiseuille Flow

A fundamental part of the methodology and model development relies on the implementation of mathematical relations to the *Simple Geometry*. From a theoretical perspective, this provides the need to discuss some aspects regarding the simulated flows. The focus of this thesis, in line with the aforementioned industrial applications, is exclusively on pressure-induced flows. This leads to the classical example of Poiseuille flow which mathematically governs one of the simplest possible pressure-induced flows, theoretically applicable in thin domains, such as in the channel subdomain for both configurations.

4.1.1 Parallel plates

The discussion and the general notation in this section highlight the most essential aspects of Poiseuille flows and follow the description of Rowe [22]. Poiseuille flow is a flow induced by a pressure at one end of a, typically, elongated geometry in the form of a pipe, or, as considered in this thesis, between two parallel plates. The laminar flow which occurs is withstood by the stresses in the fluid caused by shear. Additionally, as the velocities orthogonal to the flow direction are zero, i.e., $v = w = 0$; and with the flow is laminar, no significant lateral forces in the fluid exist [30]. Thus, the pressure across the flow is constant, i.e., $\frac{\partial p}{\partial z} = 0$. Along with the assumption of no-slip along the walls, the force balance can be seen in Figure 4.1. Noteworthy is that the following derivations can be conducted from the governing momentum equation directly, but for illustratory reasons, are herein instead based on the graphical representation of the force balance below.

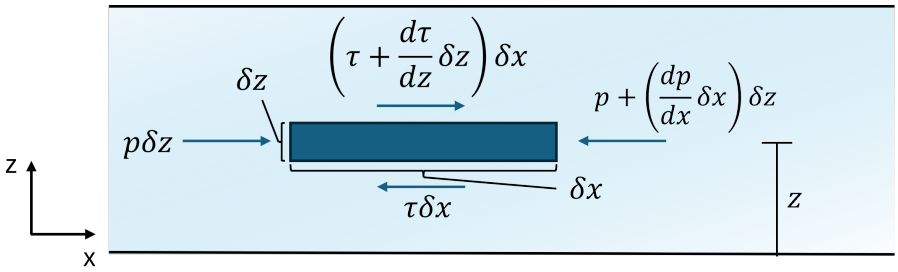

Figure 4.1: Poiseuille flow, with forces acting on a fluid element (adaption of [22]).

Based on Figure 4.1, the following (force) equilibrium equation of a fluid element of depth y takes the following form:

$$py\delta z - (p + \frac{dp}{dx}\delta x)y\delta z - \tau y\delta x + (\tau + \frac{d\tau}{dz}\delta z)y\delta x = 0, \tag{4.1}$$

where p is the pressure and τ the shear stress. Simplification of Equation (4.1) gives:

$$\frac{d\tau}{dz} = \frac{dp}{dx}. \tag{4.2}$$

By utilizing that $\tau = \mu(du/dz)$, where μ is the dynamic viscosity of the fluid, the following is given:

$$\mu\frac{d^2u}{dz^2} = \frac{dp}{dx}. \tag{4.3}$$

With the use of the following boundary conditions $du/dz = 0$ for $z = h/2$ and $u = 0$ for $z = 0$ and $z = h$ and subsequently integration twice, the velocity distribution along the channel height becomes:

$$u = \frac{1}{2\mu}\frac{dp}{dx}(zh - z^2). \tag{4.4}$$

Integration of Equation (4.4), w.r.t., z from 0 to h and subsequently dividing by h, the final expression for the bulk velocity u_b is given:

$$u_b = \frac{h^2}{12\mu}\frac{dp}{dx}. \tag{4.5}$$

Thus, concluding and displaying the simplest expressions of the governing physics for Poiseuille flow.

4.1.2 Duct

A similar derivation is made for the Poiseuille flow in a duct. While it draws upon the principles of flow in a pipe, the duct scenario employs the concept of the hydraulic diameter, see Section 2.5.1. Therefore, the discussion and the general notation follow the description of the flow in a pipe [7], with the hydraulic diameter being integrated at the end of the analysis. Similarly to the flow between plates, the pressure across the flow is constant, i.e., $\frac{\partial p}{\partial r} = 0$. Following the no-slip assumption for the walls, the illustration below applies.

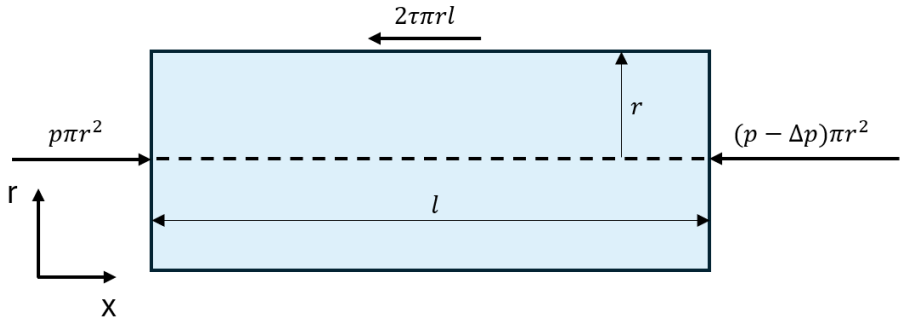

Figure 4.2: Cylinder flow, with acting forces (adaption of [7]).

Based on Figure 4.2, a force balance is made between the pressure p and shear stress τ acting on the fluid, which can be written as:

$$p\pi r^2 - (p - \Delta p)\pi r^2 - \tau 2\pi r l = 0, \tag{4.6}$$

where l is the cylinder length and r the radius. After simplification, the following relation is obtained:

$$\frac{\Delta p}{l} = \frac{2\tau}{r}. \tag{4.7}$$

With the previously mentioned dynamic viscosity μ and by utilizing that $\tau = \mu(du/dr)$, which is the general notation associated with flow in a pipe, and Equation (4.7), the following is obtained:

$$\frac{du}{dr} = \frac{\Delta p}{2\mu l}r. \tag{4.8}$$

By integrating and utilizing the boundary condition that the fluid sticks to the pipe wall, so that $u = 0$ at $r = D/2$, the following expression is obtained:

$$u_b = \frac{D^2}{32\mu}\frac{dp}{dx}, \tag{4.9}$$

where u_b is the bulk velocity. The final expression, upon replacing the pipe diameter with the hydraulic diameter of a duct D_h, transforms into:

$$u_b = \frac{D_h^2}{32\mu}\frac{dp}{dx}. \tag{4.10}$$

4.1.3 Analytical Solution of Pressure Drops

For validation purposes, the exact analytical solution to the Poiseuille flow, concerning both parallel plates and duct, was computed in the initial stages of the analysis. The calculation was initiated

by computing the pressure drop using Equation (4.5) for the scenario involving flow between the plates. After rearrangement, this equation provides the following relation:

$$\frac{dp}{dx} = \frac{12\mu u_b}{h^2}, \tag{4.11}$$

where $h = 0.01\,m$ and $\mu = 1.855 \cdot 10^{-5}\,Pa \cdot s$. The bulk velocity was set to $u = 0.02\,m/s$, which corresponds to the inlet velocity. This is based on the incompressibility assumption, i.e., negligible density change of the fluid and preservation of mass throughout the channel. Meaning, that the inlet velocity is equal to the mean (bulk) velocity of the fully developed flow. Inserting into Equation (4.11) yields the following value:

$$\frac{dp}{dx} = \frac{12\mu u_b}{h^2} = \frac{12 \cdot 1.855 \cdot 10^{-5} \cdot 0.02}{0.01^2} \approx 0.045\,Pa/m. \tag{4.12}$$

Further, with the use of the obtained result from Equation (4.12) the exact analytical velocity profile for the flow was computed. It was done by generating a large data series of z-values ranging from 0 to $0.01\,m$. By inserting the dynamic viscosity of air into Equation (4.4) along with the previously discussed variables, the velocity profile was obtained, see Appendix B.

The exact analytical solution of the Poiseuille flow in the duct was also computed. Equation (4.10) was used to calculate the pressure drop in the channel. For this case, the inlet velocity was set to $u = 0.033\,m/s$, to maintain consistency between the two configurations in terms of Reynolds number of $Re \approx 25$. The width of the channel y was set to $0.015\,m$ and the height of the channel h was set to $0.01\,m$ according to Section 3.1. The hydraulic diameter is denoted by D_h. This provided the following pressure drop in the channel for the duct-related case:

$$\frac{dp}{dx} = \frac{32\mu u_b}{D_h^2} = \frac{32\mu u_b}{(\frac{2 \cdot h \cdot y}{h+y})^2} = \left(\frac{32 \cdot 1.855 \cdot 10^{-5} \cdot 0.033}{(\frac{2 \cdot 0.01 \cdot 0.015}{0.01+0.015})^2} \right) \approx 0.136\,Pa/m. \tag{4.13}$$

Here, the room subdomain was assumed to be large enough to impose a negligible minor head loss, see Section 2.5.5, and that the pressure would be almost equal to the outlet conditions of $p = p_{atm}$. This leads to the assumption that the fluid flowing into the room is essentially a free jet. This supports the exclusion of the room subdomain in the above pressure drop calculations.

4.1.4 Pressure Drop for Pseudo 2D - Parallel Plates

In the *Pseudo 2D* model, featuring one cell between the plates within the channel, a force equilibrium equation was derived in a similar way as in Section 4.1. This was performed to gain insight into how the pressure drop is approximated with reduced dimensionality. In STAR-CCM+, the values are extracted from the midpoint of the cell [24], consequently forming the triangular velocity profile in Figure 4.3.

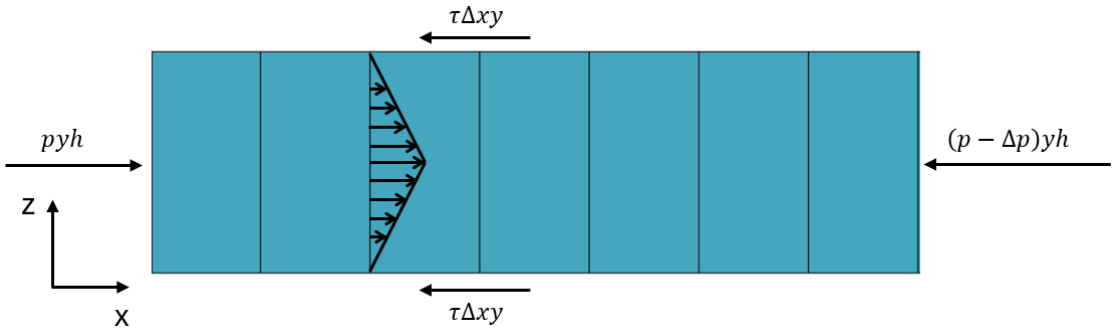

Figure 4.3: Flow between plates with one cell along the height.

Based on Figure 4.3, the equilibrium equation of a fluid element with depth y is described by the following:

$$pyh - (p - \Delta p)yh - 2\tau y \Delta x = 0, \tag{4.14}$$

where p is the pressure and τ the wall shear stress. Simplification and reformulation of the expression gives:

$$\Delta p = \frac{2\tau \Delta x}{h} \rightarrow \frac{dp}{dx} = \frac{2\tau}{h}, \tag{4.15}$$

with the reoccurring general definition of the wall shear stress $\tau = \mu \frac{du}{dz}$. By applying the no-slip boundary condition: $u = 0$ for $z = 0$ and $z = h$, and utilizing the bulk velocity: u_b for $z = h/2$, the slope of the velocity profile du/dz in the z-direction becomes:

$$\frac{du}{dz} = \frac{2u_b}{h}. \tag{4.16}$$

Combining equation (4.16) with the expression of the shear stress and Equation (4.15) gives the following:

$$\frac{dp}{dx} = \frac{4\mu u_b}{h^2}. \tag{4.17}$$

This shows that the pressure drop along the channel with the resolution of the *Pseudo 2D* mesh is one-third of that in the full *3D* model. This validated the later achieved results of the *Pseudo 2D* model, during the early stages of the model development, which differs significantly from the final version of the reduced dimensional models. The approach after the conclusion in this section is further addressed in Section 4.3.

4.2 Field Function Implementation

The pressure drop approximated by the *Pseudo 2D* model proved to be fundamentally inaccurate, as derived in the previous section, due to the poor resolution in the channel. This was remedied with the implementation of field functions, specifically to correct the momentum equation. The explored options rely on modification of the source terms in the regarded Navier-Stokes equation, enabled by user-defined field functions in STAR-CCM+. The initial idea was to add the missing pressured drop contribution via a field function specified to govern the whole channel subdomain. Through evaluation of both *mass source* and *momentum source*, the prior resulted in undesired features and proved to be more complex in its implementation due to its volume dependence in terms of its specification in the software. Furthermore, since the mass was already conserved properly, the approach to modify the momentum conservation became more feasible. In Sections 4.2.1 and 4.3 the implementation of *momentum source* is described in more detail, concerning its mathematical formulation and the adaption of boundary conditions. Where the latter aspect specifically supports the adopted mathematical formulation of *momentum source*, presented below, as it is fundamentally based on reformulating the standard form of the momentum conservation law, see Section 2.3.2.

4.2.1 Momentum Correction for Flow between Parallel Plates

The *momentum source* S_M for flow between plates, implemented in the *momentum source* field function in STAR-CCM+, is mathematically derived based on the conservation of momentum in the Navier-Stokes equations, see Section 2.3.2. Utilizing the following:

$$(1): \quad \frac{D\mathbf{u}}{Dt} = 0, \quad (2): \quad \tau = 0.$$

Here (1) is based on steady-state assumption and (2) on the implementation of slip along the walls and laminar flow, resulting in no shear occurring. This is addressed in Section 4.3. Based on Equation (2.3) this leads to the following:

$$-\nabla p + S_M = 0$$

$$S_M = \nabla p = -\frac{12\mu \mathbf{u}}{h^2}, \tag{4.18}$$

Here, h is the distance between the plates, $\mathbf{u}$ the velocity vector and μ the dynamic viscosity. Furthermore, the local velocity vector $\mathbf{u}$ conforms with the syntax of the *momentum source* in STAR-CCM+ [26]. The corresponding *momentum source derivative*, w.r.t., velocity, needing specification in STAR-CCM+, becomes:

$$\frac{\partial S_{Mx}}{\partial u} = -\frac{12\mu}{h^2}\frac{\partial u}{\partial u} = -\frac{12\mu}{h^2}, \tag{4.19}$$

$$\frac{\partial S_{My}}{\partial v} = -\frac{12\mu}{h^2}\frac{\partial v}{\partial v} = -\frac{12\mu}{h^2}, \tag{4.20}$$

$$\frac{\partial S_{Mz}}{\partial w} = -\frac{12\mu}{h^2}\frac{\partial w}{\partial w} = -\frac{12\mu}{h^2}. \tag{4.21}$$

Equations (4.18) and (4.19)-(4.21) were employed for the channel subdomain only, performed by utilizing the range of the x-axis and limiting it to apply only for $x \in [0, a]$, where a is the point where the *denser mesh region* begins.

An example illustrating the resulting formulation for the *Simple Geometry* case, is detailed in the following. Due to the flow direction being consistently aligned with a x-axis throughout the domain, the following is attained for the *momentum source*:

$$S_M = [S_{Mx}, S_{My}, S_{Mz}]^T = \left[-\frac{12\mu u}{h^2}, 0, 0\right]^T,$$

and the corresponding *momentum source derivative* becomes:

$$\frac{\partial S_{Mx}}{\partial u} = -\frac{12\mu}{h^2}\frac{\partial u}{\partial u} = -\frac{12\mu}{h^2}.$$

$$\frac{\partial S_{My}}{\partial v} = 0,$$

$$\frac{\partial S_{Mz}}{\partial w} = 0.$$

4.2.2 Momentum Correction for Flow in Ducts

Following the same approach as for parallel plates, the *momentum source* S_M for flow in ducts is mathematically expressed by the following:

$$S_M = \nabla p = -\frac{32\mu \mathbf{u}}{D_h^2}, \tag{4.22}$$

once again leveraging that the loss of momentum is equal to the pressure drop. Here, the previously addressed variables, D_h is the hydraulic diameter, $\mathbf{u}$ the velocity vector, and μ the dynamic viscosity. Herein, Equation (4.22), governing the loss of momentum, is also equated to the derived pressure drop, see the above in Section 4.2.1 for full derivation. It is also applied for all three orthogonal directions in a similar way as the case with parallel plates, see Section 4.2.1.

After differentiation, w.r.t., velocity, the *momentum source derivative* becomes:

$$\frac{\partial S_{Mx}}{\partial u} = -\frac{32\mu}{D_h^2}\frac{\partial u}{\partial u} = -\frac{32\mu}{D_h^2}, \tag{4.23}$$

$$\frac{\partial S_{My}}{\partial v} = -\frac{32\mu}{D_h^2}\frac{\partial v}{\partial v} = -\frac{32\mu}{D_h^2}, \tag{4.24}$$

$$\frac{\partial S_{Mz}}{\partial w} = -\frac{32\mu}{D_h^2}\frac{\partial w}{\partial w} = -\frac{32\mu}{D_h^2}. \tag{4.25}$$

The Equations 4.22 and 4.23-4.25 were then employed in exact same way as in Section 4.2.1.

4.3 Modification of Boundary Conditions in Pseudo 2D-C Model

For the resulting reduced dimensional model, denoted as *Pseudo 2D-C* model, a slip boundary condition was implemented along the channel walls/plates, along a distance where the channel maintained a single cell configuration before it transitioned to the *denser mesh region*, see Figure 4.4. For the parallel plate analyses, the slip boundary condition was employed on two faces within the channel, while the remaining two faces retained the symmetry boundary condition. For geometries involving ducts, the slip boundary condition was implemented on all four faces in the single-cell configured region. This means that all four no-slip faces in the *3D* model were replaced with the slip boundary condition in the *Pseudo 2D-C* model in the single cell region. This resulted in the removal of the contribution gained from the *Pseudo 2D* model in regards to pressure drop, seen in Section 4.1.4 and instead based on theory, the contribution being solely integrated based specified field functions. This aids the accuracy for cases where the generated *Pseudo 2D* mesh is not fully comprised of a one-cell structure between the spacing, as the improved resolution will potentially deviate from the demonstrated one-third of value in terms of pressure. In the slip boundary condition region, the *momentum source* and *momentum source derivative* were applied, thus fully comprising the above conditions necessary for the loss of momentum to be equal to

the pressure drop in Equations (4.18) and (4.22). However, in the smaller region, denoted as the *denser mesh region*, which is characterized by more cells in the z-direction, a no-slip condition was employed, see Figure 4.5. In consequence, the channel was divided into two segments, the *denser mesh region*, and the region containing one cell in the z-direction. The field functions were then implemented in the latter region while a no-slip condition was maintained in the former.

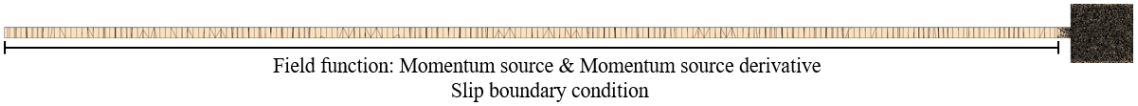

Figure 4.4: Implementation of slip boundary condition and *momentum source*.

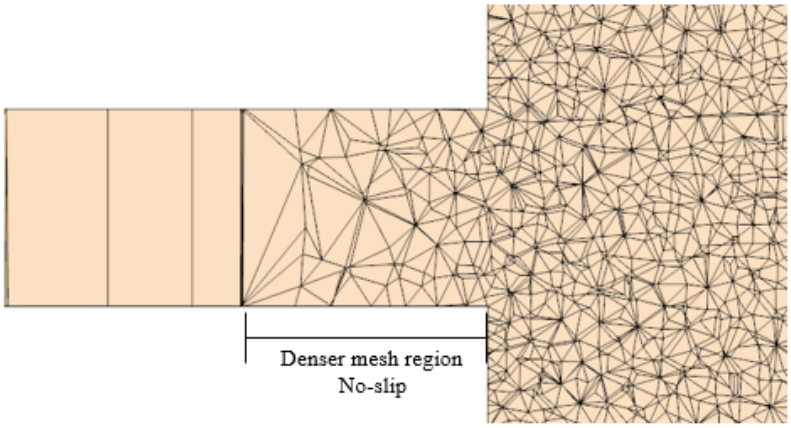

Figure 4.5: Implementation of no-slip boundary condition at *denser mesh region*.

5 Case Study - Parallel Plates

In the following section, the simulated results of the parallel plate configurations are presented. The conducted evaluation is presented in terms of the *Simple Geometry* and the results of the developed model, followed by the implementation of the following geometrical features: *Single Sharp Bend*, *Single Smooth Bend*, *Multiple Sharp Bends*, and *Multiple Smooth Bends*.

5.1 Mesh Density Adjustment for Momentum Conservation

Given the significance of conserving momentum to the greatest extent possible in the developed reduced dimensional model, a segment of the channel near the sudden expansion region needed a denser mesh region to suffice. This adjustment was also necessary to prevent poor mesh transition at the interface between the channel and room subdomain, as mentioned previously in Section 3.4.2. In the following analysis, the *Pseudo 2D*, i.e., the uncorrected version, was chosen to represent the reduced dimensional model variants, as the velocity aspects are virtually identical to the ones with implemented field functions and boundary conditions alterations.

The analysis was initially conducted for the parallel plates, to determine the optimal position for transitioning from a single cell configuration to multiple cells for the *Pseudo 2D* model (*denser mesh region*), ensuring that the maximum velocity and momentum residual remain within acceptable limits in comparison to the full *3D* model. Four different inlet velocities were set for the simulations: 0.02, 0.04, 0.06, and 0.08 m/s, corresponding to Reynolds numbers ranging from approximately 25 to 100. The conducted simulations were specifically carried out for a case where the length of the *denser mesh region* was minimal. The critical length was determined to be 0.0133 m, meaning that the channel maintained a single cell configuration between the plates for roughly 0.9867 m, along the domain before transitioning to a *denser mesh region* for the final length of 0.0133 m. Accordingly, the channel mesh composition resulted in 98.67% of reduced dimension and 1.33% of a *3D* mesh. The velocity profiles between the reduced dimensional models and *3D* models were then analyzed for various velocities just before leaving the spacing between the parallel plates, see Figure 5.1. Specifically 0.001 m before entering the room subdomain, where Figure 3.10 illustrates the position between the plates where the datasets are taken from. These depict the simulations for various inlet velocities from $U = 0.02\, m/s$ to $U = 0.08\, m/s$, illustrating the gradually increasing residual of the velocity when approaching higher Reynolds numbers. Further detail, in regards to the increasing residual value, is addressed below.

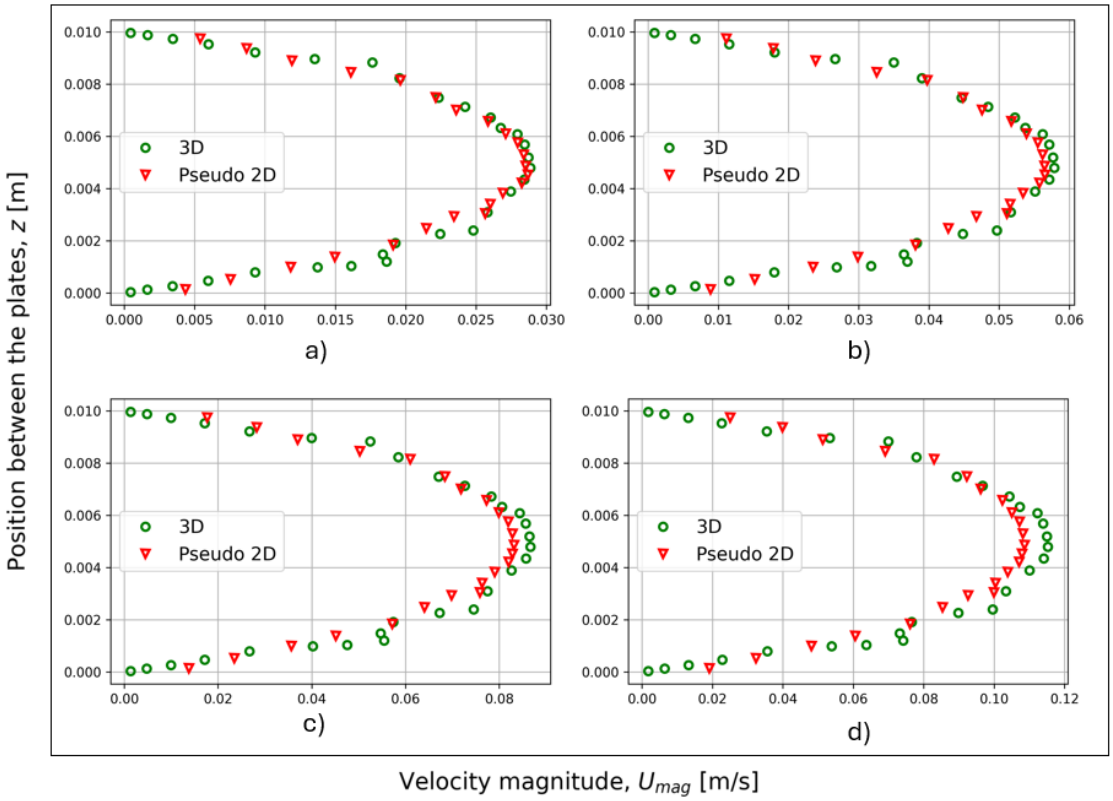

Figure 5.1: Velocity profiles for several inlet velocities: a) $U = 0.02\,m/s$; b) $U = 0.04\,m/s$; c) $U = 0.06\,m/s$; and d) $U = 0.08\,m/s$.

To provide a clearer depiction of the discrepancies between the *Pseudo 2D* and *3D* models, Tables 5.1 and 5.2 are presented. These tables outline the following parameters: the Reynolds number Re; entrance length L_e; maximum velocity for *Pseudo 2D*, denoted as $U_{max,2D}$, and for the *3D* model, denoted as $U_{max,3D}$; momentum flow rate per unit width for *Pseudo 2D*, represented as p'_{2D}, and for the *3D* model, represented as p'_{3D}; maximum velocity residual ϵ_v; and momentum flow rate residual $\epsilon_{p'}$. These parameters were used as the basis of the comparison of the models. The momentum was calculated by establishing velocity functions based on the points that define the velocity profiles. The velocity functions, derived from polynomial regression from the datasets, were subsequently used in the integration, in Equation (5.1), along the channel length by utilizing the conservation of momentum integral which was inspired by [7]:

$$p' = \rho \int_0^h u(z)^2 dz. \tag{5.1}$$

Here, p' is the concerned momentum flow rate per unit width, ρ the density of the fluid, $u(z)$ the velocity as a function of the position between the plates z, and h the distance between the plates.

Table 5.1: Parameter values for $U = 0.02\,m/s$ and $U = 0.04\,m/s$.

Velocity inlet	**0.02 m/s**	**0.04 m/s**
Re	25.53	51.07
L_e	3.06 cm	6.13 cm
$U_{max,2D}$	0.029 m/s	0.057 m/s
$U_{max,3D}$	0.029 m/s	0.058 m/s
p'_{2D}	5.196e-6 kg/s^2	2.016e-5 kg/s^2
p'_{3D}	5.258e-6 kg/s^2	2.114e-5 kg/s^2
ϵ_v	0.645%	2.35%
$\epsilon_{p'}$	1.18%	4.64%

Table 5.2: Parameter values for $U = 0.06$m/s and $U = 0.08$m/s.

Velocity inlet	**0.06 m/s**	**0.08 m/s**
Re	76.6	102.13
L_e	9.19 cm	12.26 cm
$U_{max,2D}$	0.083 m/s	0.109 m/s
$U_{max,3D}$	0.087 m/s	0.115 m/s
p'_{2D}	4.363e-5 kg/s^2	7.445e-5 kg/s^2
p'_{3D}	4.742e-5 kg/s^2	8.390e-5 kg/s^2
ϵ_v	4.08%	5.8%
$\epsilon_{p'}$	8%	11.26%

The maximum residuals in velocity and momentum within the velocity range of $U = 0.02-0.08 m/s$ are plotted in Figures 5.2-5.3 as a function of the entrance length, which is directly related to Reynolds number according to Equation (2.19). The following plots display the simulated results with a *denser mesh region* length of 0.0133 m.

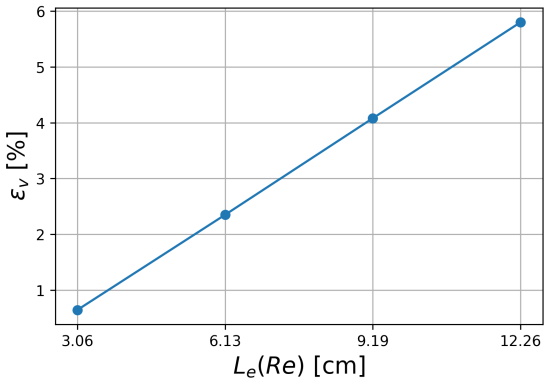

Figure 5.2: Maximum velocity residual ϵ_v as a function of entrance length.

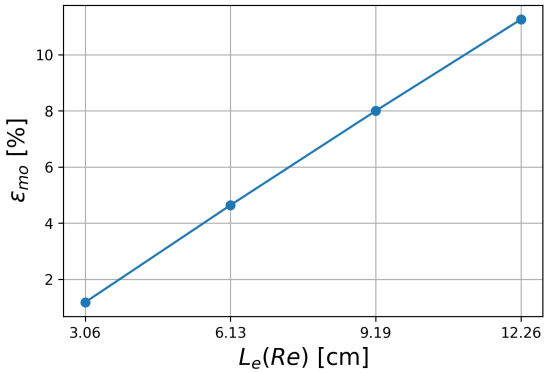

Figure 5.3: Momentum residual ϵ_{mo} as a function of entrance length.

It is evident that the maximal velocity residual, as well as the momentum residual follow a linear trend. The linear function, attained based on linear regression, approximates the residual of the maximal velocity, and the momentum residual as a function of the entrance length. By analyzing these trends, the relationship between the length of the channel's end, where the transition from a single cell to more cells occurs, and the entrance length can be determined depending on the desired accuracy of the results. The residuals as a function of the entrance length for Reynolds numbers up to 100 are described in Equations (5.2) and (5.3). This range is chosen because the applications of interest, discussed in Section 1, experience low Reynolds numbers:

$$\epsilon_v(L_e) = 0.56L_e - 1.069, \tag{5.2}$$

and

$$\epsilon_{mo}(L_e) = 1.096L_e - 2.174, \tag{5.3}$$

where ϵ_v and ϵ_{mo} denote the residual of maximum velocity and momentum, respectively, based on the entrance length for a *denser mesh region* length of 0.0133 m at the channel end in the reduced dimensional model. To consistently obtain a residual below 5% of the regarded values, the following should be adopted, based on Equation (5.2) and (5.3):

$$L_{DSM} \geq \frac{1}{5}L_e, \tag{5.4}$$

where L_{DSM} is the *denser mesh region* length and L_e the entrance length. The proposed relation was further validated for a higher Re in Section 5.2. Aside from the maximum residuals concerned, the overall influence of the velocity profile on the jet formation was considered. The evaluation is discussed in Appendix C, where a brief comparison between a planar and a parabolic velocity profile with equal mass flow was conducted. This demonstrates an attempt to evaluate the differences between the desired profile and a planar equivalent. Ultimately, displaying the need for the *denser mesh region*, in contrast to a full slip-condition along the whole channel subdomain.

5.2 Validation of Denser Mesh Region for Higher Reynolds Numbers

Based on the study presented in Section 5.1, using a *denser mesh region* length equivalent to 1/5 of the entrance length at the end of the channel is sufficient to maintain a maximum deviation of approximately 5% for both momentum and maximum velocity before entering the room subdomain when compared to the fully resolved *3D* model. To ensure that this relation also applies to higher velocities characterized by a high laminar Reynolds number, a test simulation was performed for an inlet velocity of $U = 0.5\,m/s$ with the following specifications:

Table 5.3: Data for $U = 0.5\,m/s$.

Velocity inlet	**0.5 m/s**
Re	638.33
L_e	76.6 cm

Based on Table 5.3, the *denser mesh region* was utilized at a distance of $0.153\,m$ across the channel end, equivalent to 1/5 of the entrance length. Figure 5.4 shows the velocity profile in the channel, between the plates, $0.001\,m$ before entering the room, see Figure 3.10.

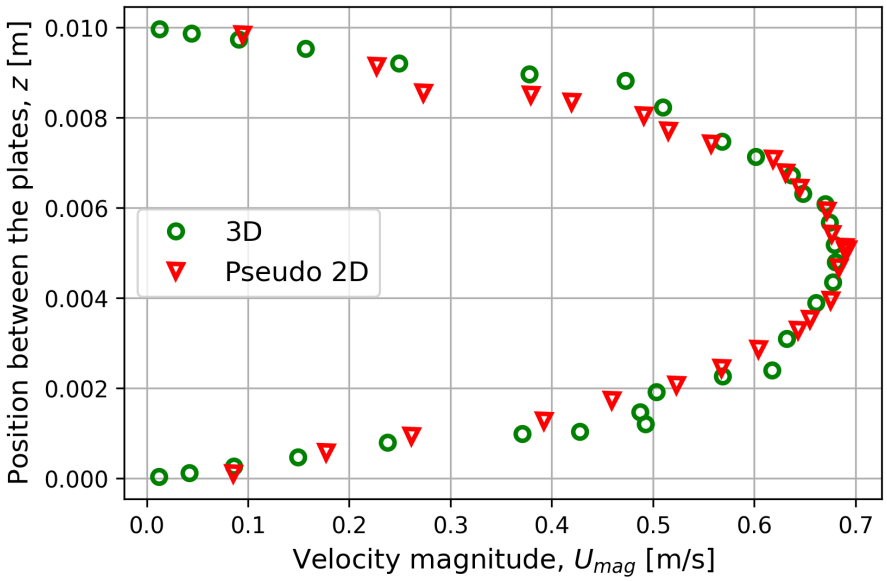

Figure 5.4: Velocity profile for $U = 0.5\,m/s$.

The maximum velocity $U_{max,2D}$ for *Pseudo 2D* and $U_{max,3D}$ for *3D* model; momentum flow rate per unit width p'_{2D} for *Pseudo 2D* and p'_{3D} for *3D* model; maximum velocity residual ϵ_v; and momentum flow rate residual $\epsilon_{p'}$, is for both models depicted in Table 5.4 respectively.

Table 5.4: Data for $U = 0.5\,m/s$.

Velocity inlet	**0.5 m/s**
$U_{max,2D}$	0.692 m/s
$U_{max,3D}$	0.680 m/s
p'_{2D}	3.024e-3 kg/s^2
p'_{3D}	2.923e-3 kg/s^2
ϵ_v	1.71%
$\epsilon_{p'}$	3.46%

The results confirm that the residuals for both momentum and maximum velocity are below the specified limit of 5%. This demonstrates that the applied relationship of 1/5 of the entrance length also applies to laminar flows with higher Reynolds numbers for parallel plate configurations.

5.3 Simple Geometry

After concluding the specific parallel plates model development aspects, this section presents the simulation results for the *Simple Geometry* case. The highlighted results are based on $Re \approx 25$ in the channel subdomain, corresponding to an inlet velocity of $U = 0.02\,m/s$. In this analysis, all models, i.e., the *3D*, *Pseudo 2D* and *Pseudo 2D-C* are evaluated and discussed.

5.3.1 Evaluation and Discussion

The results show that the *Pseudo 2D-C* model closely aligns with the results obtained from the *3D* model. This is particularly evident in the plots for the pressure along the channel and the velocity in the room subdomain. Figure 5.5 illustrates the velocity distribution in the xz plane along the whole domain for the *3D* model. Most of the room subdomain has velocities close to $0\,m/s$, therefore the part of the room where the velocity is very close to zero is excluded. Consequently, all models and analyses in the subsequent sections will reflect this adjustment, as illustrated in Figure 5.6. Figure 5.7 displays the results of the pressure contour plots in the channel subdomain for the *3D* model, *Pseudo 2D* model and *Pseudo 2D-C* model. The pressure in the room subdomain is negligible, due to its large size, thus only the pressure in the channel subdomain is displayed. This holds for all models and analyses in the subsequent sections.

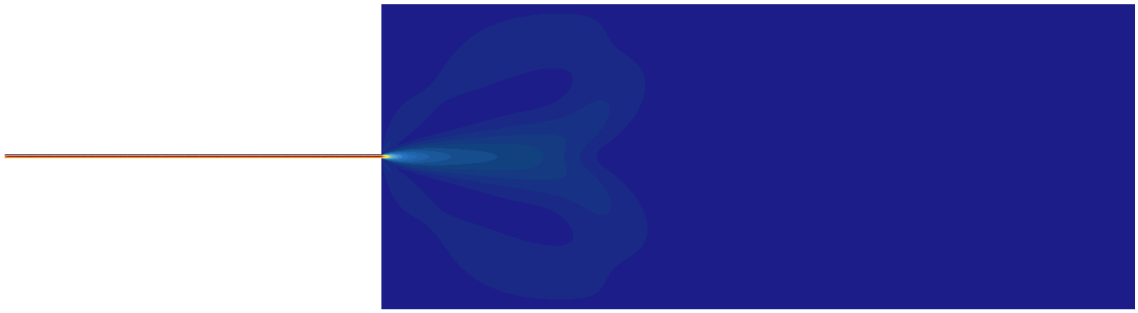

Figure 5.5: Contour plot; Velocity magnitude for *3D* model.

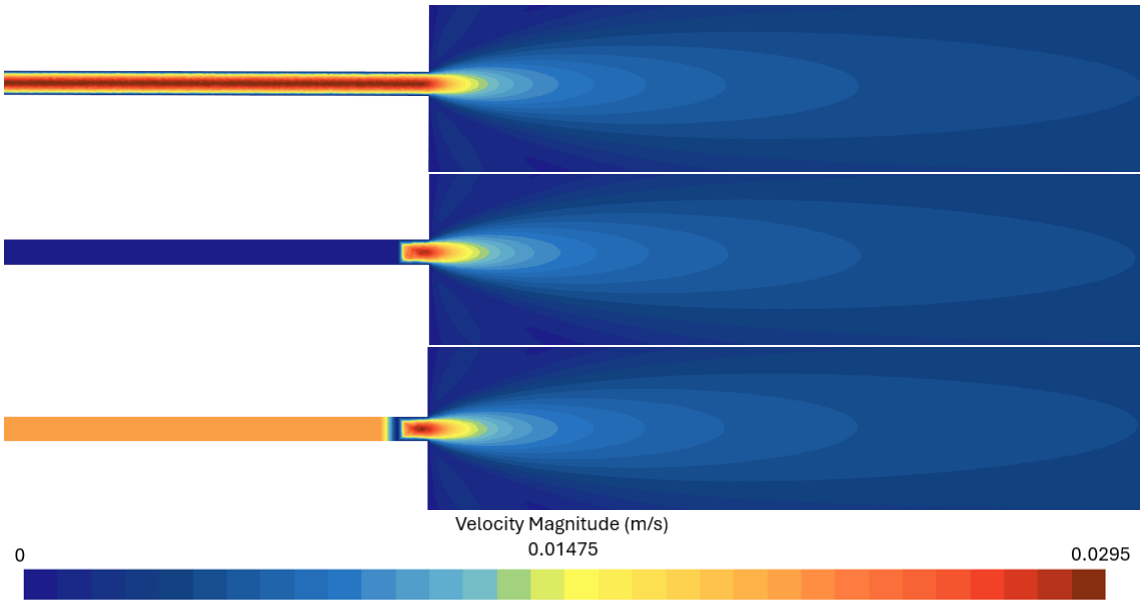

Figure 5.6: Contour plot; Velocity magnitude for *3D* model (top), *Pseudo 2D* model (middle) and *Pseudo 2D-C* model (bottom), respectively.

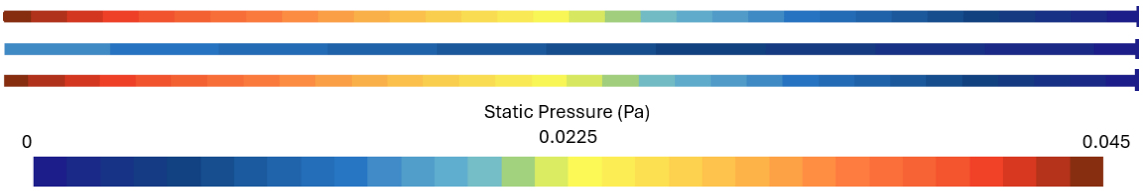

Figure 5.7: Contour plot; Static pressure for *3D* model (top), *Pseudo 2D* model (middle) and *Pseudo 2D-C* model (bottom), respectively.

To provide a clearer representation of the results, graphs depicting the pressure and velocity along the center-line of the domain were generated, see Figures 5.8-5.9. The center-line of the domain is illustrated in Figure 3.10.

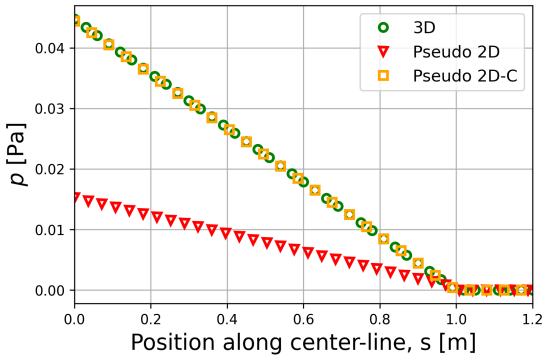

Figure 5.8: Pressure p along center-line of domain.

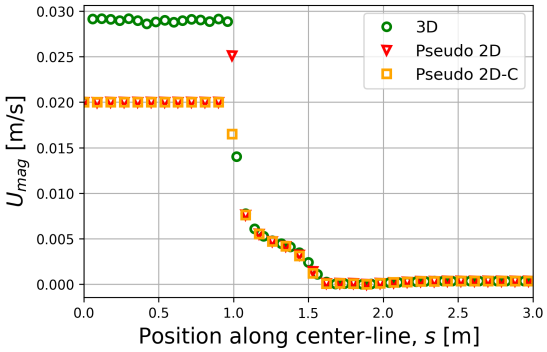

Figure 5.9: Velocity magnitude U_{mag} along center-line of domain.

The depicted results show that the *Pseudo 2D* model has a pressure three times lower than the *3D* model. This outcome is, however, expected based on the theory describing the pressure drop for the *Pseudo 2D* model configuration in Section 4.1.4. Furthermore, the results also indicate that the pressure diminishes to zero before the sudden expansion, which is expected considering the static pressure set to zero (relative to atmospheric pressure) at the room outlet and its large size compared to the precursor. To further evaluate the pressure, due to the superimposition of data between the *3D* and the *Pseudo 2D-C*, a residual plot was created, as shown in Figure 5.10, illustrating the pressure residuals compared to the *3D* model. The pressure residuals were calculated by computing the absolute difference between the model under consideration and the *3D* equivalent and dividing by the pressure value of the *3D* model, accordingly:

$$\text{Pressure Residual} = \frac{|P_{2D*} - P_{3D}|}{P_{3D}}, \tag{5.5}$$

where P_{2D*} is the pressure of the concerned reduced dimensional model and P_{3D} the pressure value of the *3D* simulation.

All three models display similar results for velocities along the center line of the domain. In the channel, the velocity across the center-line is $U = 0.02\,m/s$ for the *Pseudo 2D* cases, which is expected because of the one cell configuration between the plates. With only one cell existing between the plates, all cells get assigned the same value based on continuity. In this case, it means that they attain the mean (bulk) velocity value, corresponding to the specified inlet condition of $U = 0.02\,m/s$. A conclusion that can be drawn is that the velocity profiles across the room are similar across all three cases. The *Pseudo 2D* case performs notably well due to the low velocity/Reynolds numbers analyzed. Since there is a significant deviation in pressure, it is of utmost importance to artificially correct it which was done in alignment with the method described in Section 4.3. This method ensures that the *Pseudo 2D-C* model closely aligns with the obtained results of the full 3D model in terms of both pressure and velocity. See Figure 5.11 for a more accurate representation of the velocity residual compared to the *3D* model. The velocity residuals are calculated by computing the difference between the model under consideration and the *3D* equivalent and dividing by the velocity value of the *3D* model, accordingly:

$$\text{Velocity Residual} = \frac{|U_{2D*} - U_{3D}|}{U_{3D}}, \tag{5.6}$$

where U_{2D*} is the velocity of the concerned reduced dimensional model and U_{3D} the velocity value of the *3D* simulation.

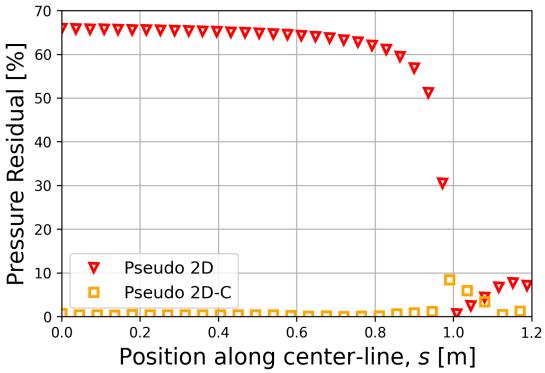

Figure 5.10: Pressure residuals, w.r.t., *3D*.

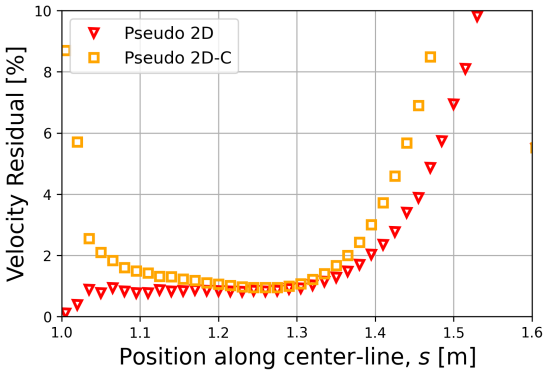

Figure 5.11: Velocity residuals, w.r.t., *3D*.

The pressure residual plot for the *Pseudo 2D-C* model is nearly zero throughout the entire channel subdomain, except near the end where the pressure values are very close to zero. This confirms the effectiveness of the *momentum source* and *momentum source derivative* correction applied in the *Pseudo 2D-C* model. The numerical pressure difference in terms of absolute values is also plotted, see Figure 5.12. The pressure numerical difference is calculated by computing the absolute difference between the model under consideration and the *3D* equivalent, accordingly:

$$p_{diff} = |P_{2D*} - P_{3D}|\,, \tag{5.7}$$

where p_{diff} is the pressure numerical difference, P_{2D*} is the pressure of the concerned reduced dimensional model and P_{3D} the pressure value of the *3D* simulation.

It is evident from the velocity residual plot, see Figure 5.11, that the residuals are small for the reduced dimensional models, for positions below $1.5\,m$, which is considered satisfactory. This further confirms that the *denser mesh region* is sufficiently large for the flow to develop before entering the room subdomain. However, the residuals start to increase beyond $1.5\,m$. This is due to the velocity dropping close to zero after this position. Relying on percentage deviation when dealing with small numbers can be misleading since it is sensitive to small changes. The result is that the residual in percent could appear to be very large but the actual numerical difference could still be very low. To avoid misrepresentation, the actual numerical difference is displayed alongside the residual. The numerical velocity difference in terms of absolute value is thus plotted in Figure 5.13. The velocity numerical difference is calculated by computing the absolute difference between the model of consideration and the *3D* equivalent, accordingly:

$$U_{diff} = |U_{2D*} - U_{3D}|\,, \tag{5.8}$$

where U_{diff} is the velocity numerical difference, U_{2D*} is the velocity of the concerned reduced dimensional model and U_{3D} the velocity value of the *3D* simulation.

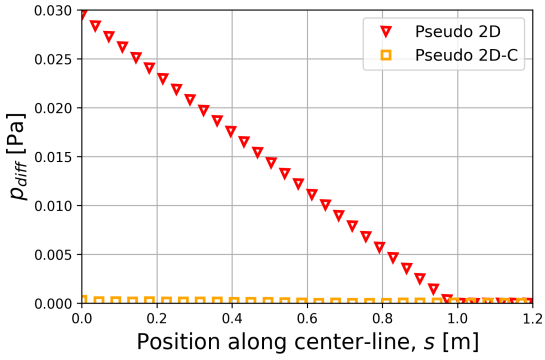

Figure 5.12: Pressure diff. p_{diff}, w.r.t., *3D*.

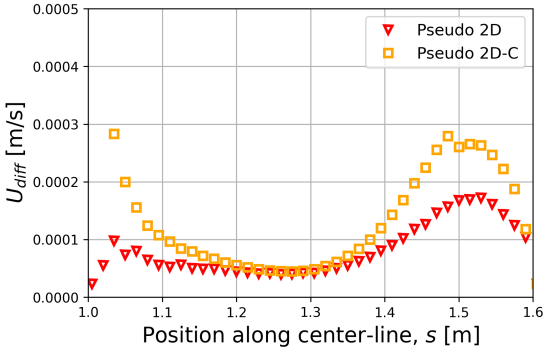

Figure 5.13: Velocity diff. U_{diff}, w.r.t., *3D*.

As observed, the numerical velocity difference is low, in the order of 10^{-4} across the entire room subdomain. Looking at the pressure difference plot, it becomes evident that there is a significant

difference between the *Pseudo 2D* and *Pseudo 2D-C* model. The pressure difference between the *3D* and *Pseudo 2D-C* model is nearly zero throughout the entire channel subdomain. The overall results are thus satisfactory for the reduced dimensional model, with a resulting significant cell count reduction compared to the *3D* model. Table 5.5 demonstrates the mesh count for the *3D* and *Pseudo 2D* model in the channel subdomain, which is the same as the *Pseudo 2D-C* model. It also shows the relative cell amount, i.e., the number of cells in the *Pseudo 2D* divided by the number of cells in the *3D* model. It is important to highlight that the relative cell amount is small, less than 1%, meaning that the number of cells in the *Pseudo 2D* is substantially lower than the *3D* mesh. Despite this, the results for the *Pseudo 2D-C* align well with the *3D* model. This demonstrates that significant computational resources and time can be saved while still maintaining a high level of accuracy, at least concerning the evaluated flow features: the pressure drop throughout the domain and the velocity of the jet.

Table 5.5: Cell count comparison (channel) - *Simple Geometry*.

3D	***Pseudo 2D***	**Relative cell amount [%]**
713 668	3 225	0.45

5.4 Single Sharp Bend

To evaluate and explore the applicability of the *Pseudo 2D-C* model, a geometrical component in the form of a 90° bend, elbow, was implemented. The geometry contains the same characteristics as the *Simple Geometry* but with the mentioned elbow at half the channel center-line length, totaling the center-line length to 1 m, see Figure 5.14 for full details. The previous explaining its earned name, *Single Sharp Bend*.

Figure 5.14: *Single Sharp Bend* geometry in xz plane.

5.4.1 Mesh Generation

The mesh was generated based on the results derived from the performed mesh convergence study on the *Simple Geometry*. Thus, the resulting choice of mesh settings was assumed to be suitable and were thereby adopted for the new geometry. The control volume set on the channel subdomain, *VC-CA*, in the *3D* model was adjusted to incorporate the vertical section of the channel. The resulting mesh with focus on the bend can be viewed in Figures 5.15-5.16. A three-dimensional unstructured mesh was unavoidably formed in the *Pseudo 2D* mesh for *Single Sharp Bend*, as a product of the geometrical change, and by extension the undefined thickness property of the discontinuous, sharp feature.

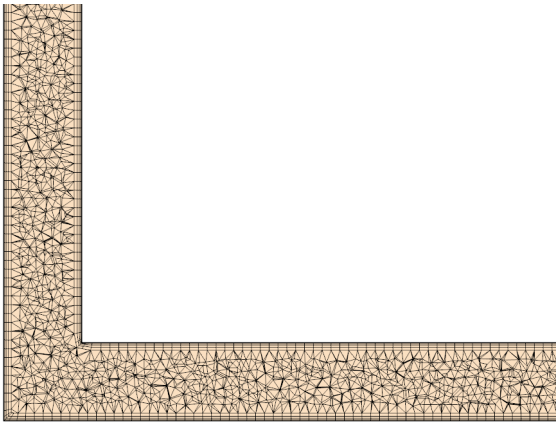

Figure 5.15: *3D* mesh for *Single Sharp Bend* in channel subdomain.

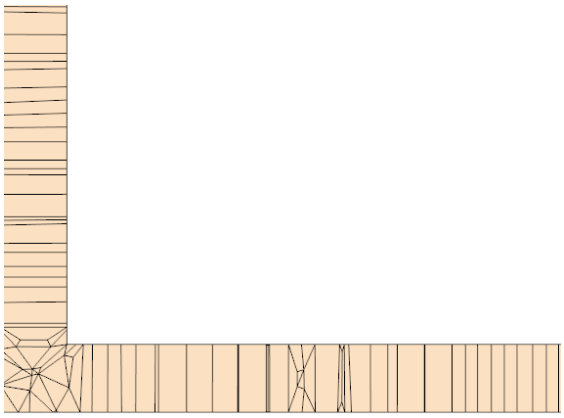

Figure 5.16: *Pseudo 2D* mesh for *Single Sharp Bend* in channel subdomain.

Table 5.6 shows the cell count and relative cell amount in the channel subdomain. Herein, the relative cell amount is small, less than 1%, meaning that the number of cells in the *Pseudo 2D* is substantially lower than the *3D* mesh.

Table 5.6: Cell count comparison (channel) - *Single Sharp Bend*.

3D	***Pseudo 2D***	**Relative cell amount [%]**
730 097	5 275	0.72

The configuration in regard to the physics and solver settings and field function implementation is identical to the ones used for the *Simple Geometry* case. As the *momentum source* is specified as a vector, the bending of the pipe, and the resulting flow direction change, is automatically accounted for in the correction. Meaning, that the momentum resistance is modelled for all directions at all points along the channel subdomain. Such that, if there is an existing velocity component there is resultingly a modelled (negative) contribution to the momentum. For specific details of the employment of field functions, see Section 3.3 and 4.2, respectively.

5.4.2 Evaluation and Discussion

The simulation of the *Pseudo 2D-C* model indicate that it is in close alignment with the results obtained from the *3D* model. To offer a clear depiction of the findings, graphs showing the velocity and pressure along the center-line of the domain are shown in Figure 5.17-5.18. Furthermore, Figure 3.10 illustrates the center-line position for the *Simple Geometry* case, which is similarly applicable here. The results show that the pressure and velocity are similar to the ones obtained for the *Simple Geometry*, see Section 5.3.1, particularly evident for the concerned properties along the center-line. In terms of pressure, this is partially due to the feature-imposed minor losses being negligible, attributable to the low velocity, discussed further in Section 2.5.5. This means that the resulting pressure drop is almost exactly equal to that of the *Simple Geometry* case and is expectedly captured accurately by the reduced dimensional model. The data in terms of velocity along the center-line jet-region shows a superimposed feature, indicating in detail that the formed jet is highly accurate.

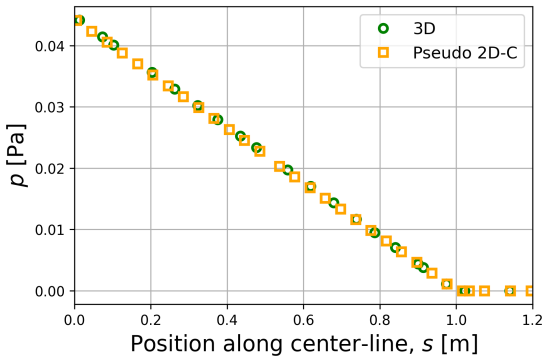

Figure 5.17: Pressure p along center-line of domain.

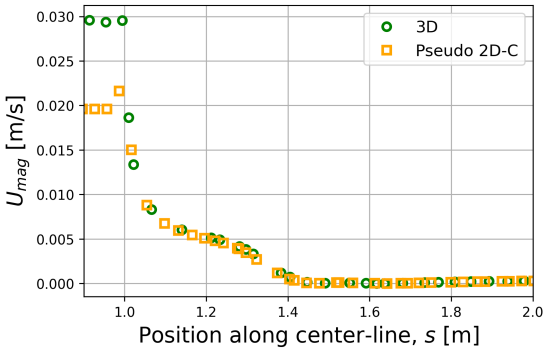

Figure 5.18: Velocity magnitude U_{mag} along center-line of domain.

The data plots indicate that the *Pseudo 2D-C* model achieves good results in comparison to the *3D* model concerning both flow aspects. This ultimately suggests that the constructed *Pseudo 2D-C* model is applicable to geometries featuring sharp bends in channels for low Reynolds number flows.

5.5 Single Smooth Bend

For further exploration and identification of potential inherent features in the sharp 90° bend, a continuously smooth bend equivalent was constructed, termed *Single Smooth Bend*. The geometry was constructed from the *Simple Geometry* and incorporates its elbow at approximately half the channel length. The room subdomain is geometrically identical to the *Simple Geometry* for consistency and simplification purposes. From the room, the channel extends by a horizontal part of 0.5 m, where the bend connects the perpendicular, vertical section via a channel center-line arc length of 0.0157 m. The vertical section of the channel contains the remaining length 0.4843 m which totals the channel center-line length to 1 m. The bend is based on a radius of 0.01 m and 90° turn, resulting in its aforementioned center-line length. The geometry can be seen in Figure 5.19.

Figure 5.19: *Single Smooth Bend* geometry in xz plane.

5.5.1 Mesh Generation

After the construction of the geometry, the mesh generation was done in accordance with the sharp bend geometry. The generated mesh in the channel subdomain differed as a result of the *Thin Mesher*, explained in Section 3.4.2, functioning properly and enabling the formation of a consistent configuration of *Pseudo 2D* mesh along the whole subdomain. This is because the channel thickness is constant and, by the algorithmic program used to generate the mesh, identifiable throughout the whole subdomain. The mesh, with focus on the geometrical feature, can be seen in Figures 5.20-5.21. For information regarding the difference in amount of cells for the channel subdomain, see Table 5.7.

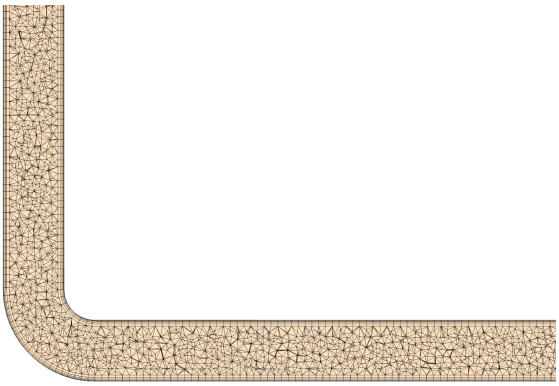

Figure 5.20: *3D* mesh for *Single Smooth Bend* in channel subdomain.

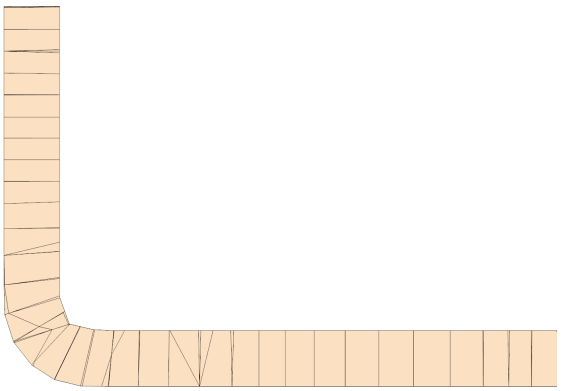

Figure 5.21: *Pseudo 2D* mesh for *Single Smooth Bend* in channel subdomain.

Table 5.7: Cell count comparison (channel) - *Single Smooth Bend*.

3D	***Pseudo 2D***	**Relative cell amount [%]**
707 011	3 132	0.44

The setup, encompassing physics, solver settings, and field function formulation follow the same implementation as in the *Simple Geometry* case, explained in Section 4.2. However, inevitable and evident adaptations exist, as a result of new boundaries arising due to the implemented geometrical feature, see Figure 5.19. For example, the previously implemented field functions now have to be extended to function for a larger range of z-values due to the vertical section of the channel.

5.5.2 Evaluation and Discussion

Similar to the sharp bend, the results show no significant difference. Theoretically, this is expected as smooth bends have a lower minor loss coefficient than sharp equivalents [7]. In terms of the formed jet and the pressure along the domain, the *Pseudo 2D-C* model and the *3D* are equivalent. It is also evident that the velocity and pressure closely match those of the *3D* model, indicating that whether it is a sharp or smooth bend, the overall results remain unaffected. The graphical representation of the pressure and velocity is presented along the center-line in Figure 5.22-5.23. The extraction of the data is similar to the *Simple Geometry* case, see Figure 3.10, where data is collected from the center-line position along the domain.

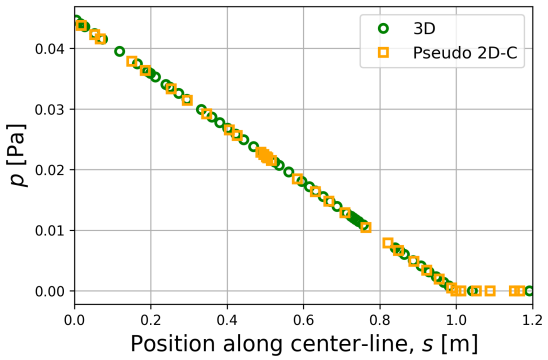

Figure 5.22: Pressure p along center-line of domain.

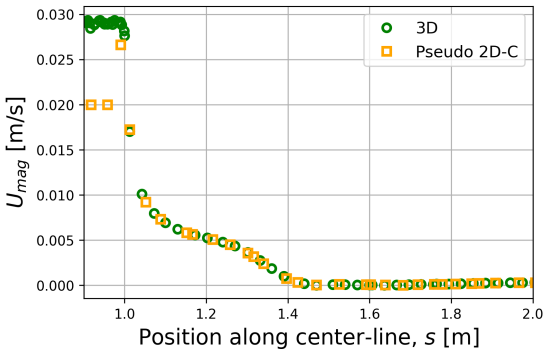

Figure 5.23: Velocity magnitude U_{mag} along center-line of domain.

As mentioned previously, it is, for the considered geometrical case, apparent that the pressure and velocity plots along the domain of the *Pseudo 2D-C* model exhibit satisfactory outcomes. Similarly to the previous bend-related geometrical feature, the *momentum source*, included in *Pseudo 2D-C* model, is applied for all directions throughout the whole channel subdomain, except for the *denser mesh region*. The *momentum source*, specified as a loss of momentum along the channel, thus accurately computes the pressure drop throughout the domain. Despite the minor losses being negligible, a demonstration of applicability is still exhibited in the previous and the reduced dimensional model shows potential for smooth bend geometries as well, especially in terms of meshing.

A deviant feature was noted in the *Pseudo 2D* model in the initial stages of the study concerning *Single Smooth Bend*. This affected the velocity magnitude of the flow beyond the channel bend. Ultimately, later realized, this had no impact on the corrected reduced dimensional model, *Pseudo 2D-C*, due to the change of boundary conditions to slip. For more information concerning this, as well as some meshing aspects worth consideration, see Appendix D.

5.6 Multiple Sharp Bends

To evaluate the applicability of the developed correction method and reduced dimensional model, a second geometrical feature was implemented. As insinuated by its name, *Multiple Sharp Bends*, it incorporates several sharp bends consecutively, with equal channel lengths after each bend. The specific details with regards to the geometry can be seen in Figure 5.24.

Figure 5.24: *Multiple Sharp Bends* geometry in xz plane.

The purpose of this geometry is to examine the effect of consecutive bends as the previous geometrical feature imposed a negligible minor head loss. Specific interest is reserved to evaluate if the effect is too substantial to not specifically address or correct, by determining if the *Pseudo 2D-C* model deviates significantly from the *3D* model.

5.6.1 Mesh Generation

The meshing follows an identical implementation as the one described for *Single Sharp Bend* and *Single Smooth bend*, except for the needed repositioning of the channel volume control, *VC-CA*, in the *3D* model to increase the resolution of the mesh. The result is displayed in Figure 5.25, and, as expected, exhibits a similar tendency towards three-dimensional unstructured cell-formation in the bends for the *Pseudo 2D* mesh, as seen in Section 5.4. See Table 5.8 for an illustration of the cell count and relative cell amount in the channel subdomain.

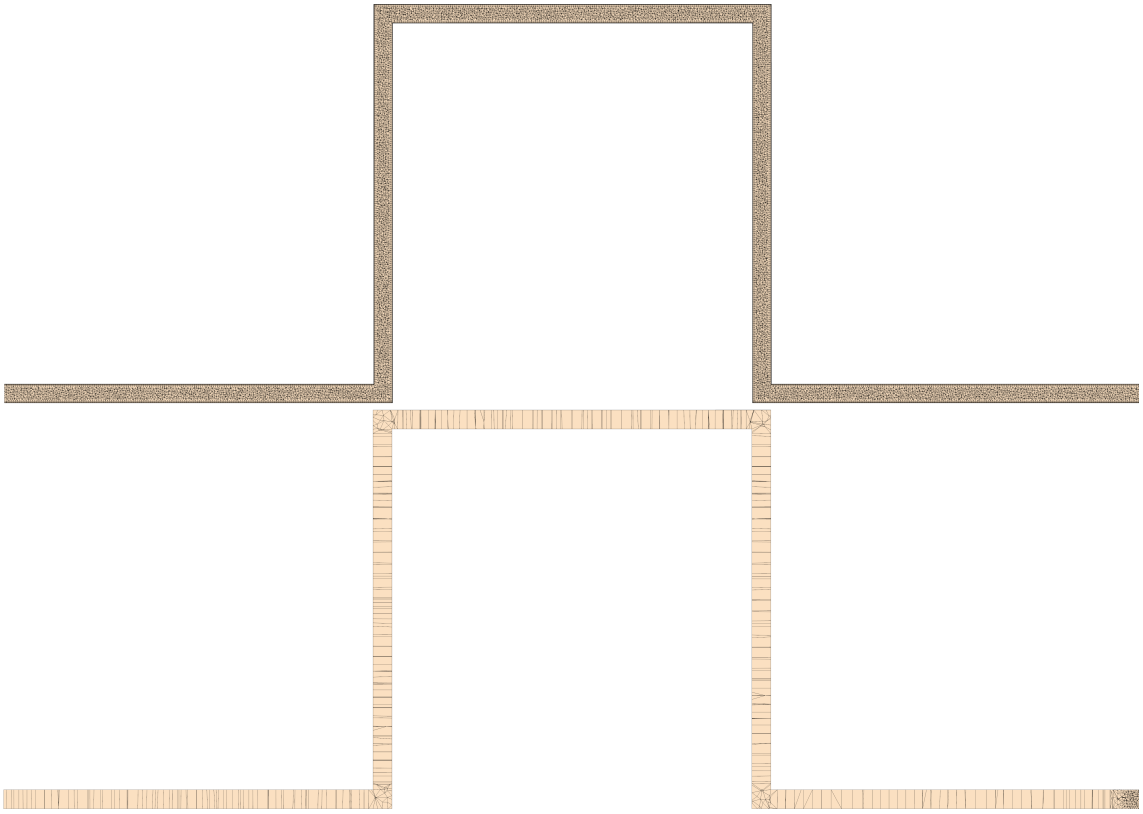

Figure 5.25: *Multiple Sharp Bends* for *3D* and *Pseudo 2D* mesh in channel subdomain.

Table 5.8: Cell count comparison (channel) - *Multiple Sharp Bends*.

3D	***Pseudo 2D***	**Relative cell amount [%]**
727 531	7 222	0.99

Even for this case, the relative cell amount, i.e., the number of cells in the *Pseudo 2D* model divided by the number of cells in the *3D* model is low, $\approx 1\%$. Despite this, the results for the *Pseudo 2D-C* align well with the *3D* model, see Section 5.6.2.

The solver settings, physics, and field functions are implemented in the same way as for the previous geometrical feature, with the natural exception of the change in treatment of some of the channel boundaries as a result of the geometrical alteration.

5.6.2 Evaluation and Discussion

The analysis for the multiple bend configuration showed that employing the same methodology as for the single bend yields satisfactory results. The findings indicate similar behavior between the two characteristically similar geometries: single and multiple bends. This can be noted by observation of the pressure and velocity, along the center-line of the channel and the room subdomain, depicted in Figure 5.26-5.27. This further validates the demonstrated negligible contribution from the minor losses for the simulated laminar airflow. The extraction of the data is similar to the *Simple Geometry* case, see Figure 3.10, where data is collected from the center-line position along the domain.

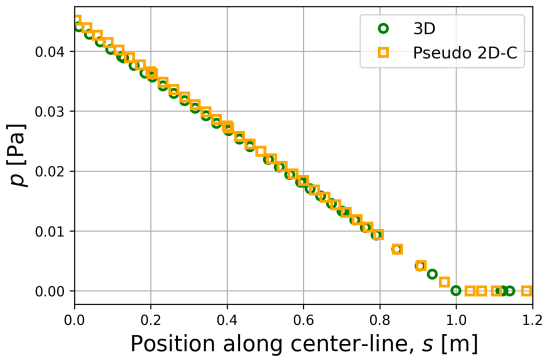

Figure 5.26: Pressure p along center-line of domain.

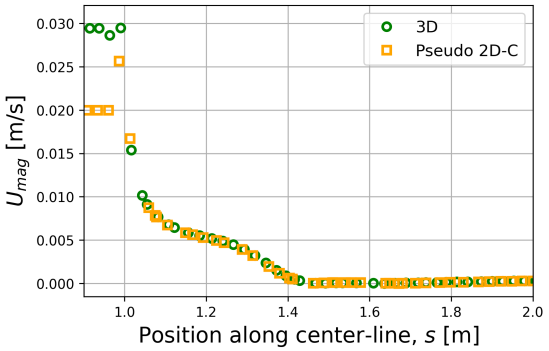

Figure 5.27: Velocity magnitude U_{mag} along center-line of domain.

The graphs illustrate that the *Pseudo 2D-C* model is in close alignment with the *3D* model in terms of pressure distribution and velocity along the domain. Minor discrepancies or irregularities occur at positions $x = 0.2,\ 0.4,\ 0.6,\ 0.8\,m$, corresponding to the locations of the bends. This is anticipated in terms of velocity, as the center-line velocity is no longer equal to the center value of the parabolic profile in a straight section. However, the irregularities do not affect the overall outcome of the simulations and the evaluation.

5.7 Multiple Smooth Bends

In alignment with previously considered geometrical features, a smooth bend equivalent was constructed for the analysis of multiple bends. The geometrical configuration differs slightly from the *Multiple Sharp Bends* geometry as the rounded bends contribute to the total length of the center-line. It was decided to construct the geometry such that it would contain part-wise straight sections of the length $0.2\,m$, originating from the room, and consequently, the last horizontal section would be comprised of the remaining center-line length to reach a total length of $1\,m$. For visualization of the geometry, see Figure 5.28.

Figure 5.28: *Multiple Smooth Bends* geometry in xz plane.

5.7.1 Mesh Generation

The mesh construction followed a similar approach to that of the *Multiple Sharp Bends* equivalent, and the mesh used can be seen in Figure 5.29.

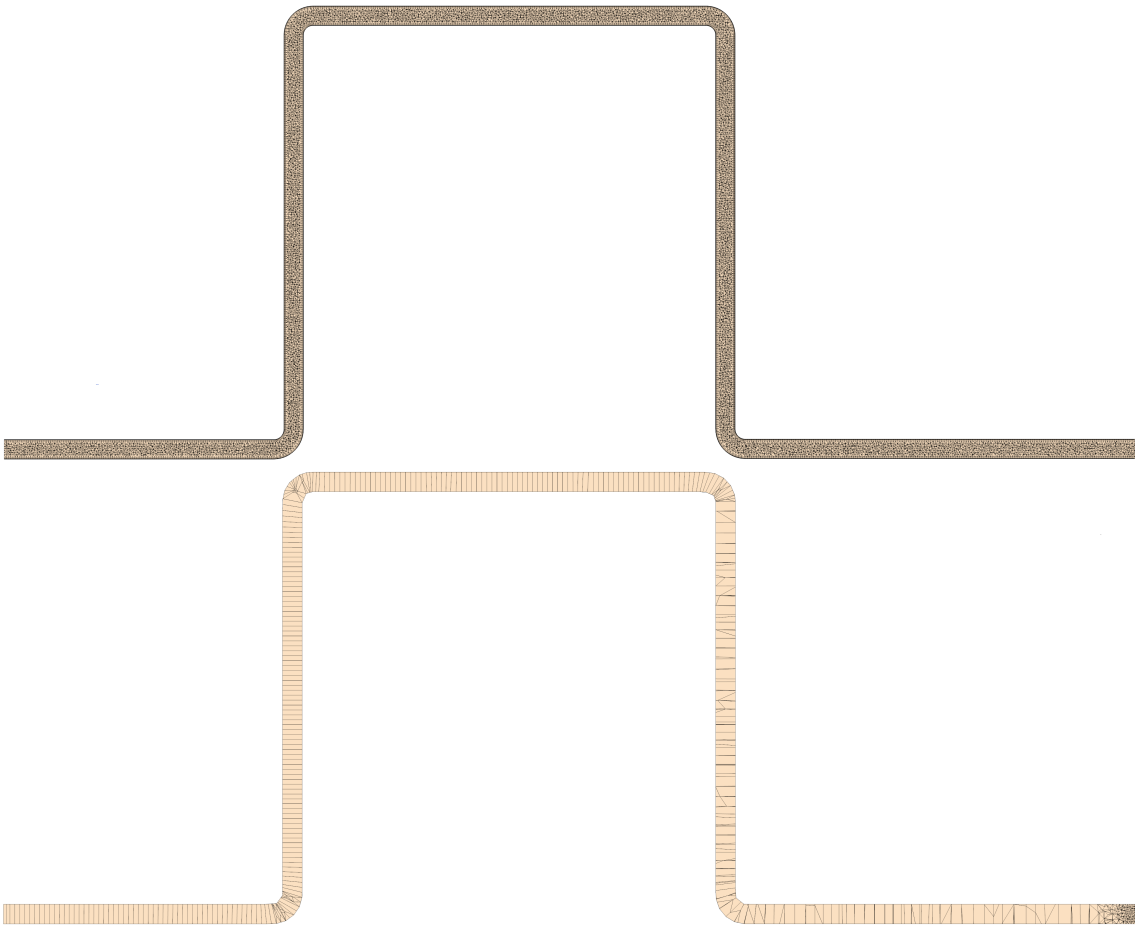

Figure 5.29: *Multiple Smooth Bends* for *3D* and *Pseudo 2D* mesh in channel subdomain.

The attained reduction in cell amount for the channel subdomain is displayed in Table 5.9. Displaying that the *Pseudo 2D* mesh contains $\approx 1\%$ of cells required in the *3D*.

Table 5.9: Cell count comparison (channel) - *Multiple Smooth Bends*.

3D	***Pseudo 2D***	**Relative cell amount [%]**
719 219	6 942	0.97

The resulting generated grid system displays, to some degree, a more inconsistent meshing attribute, as seen by comparing the different cell configurations in the various bends. The mesh in the bends closer to the room consists of the desired 2D meshing pattern. Whereas the irregularity and unstructuredness seem to increase the further away from the room subdomain, in the channel.

Similarly, as mentioned previously, the *momentum source* is permitted to act freely in all directions for the vast part of the channel subdomain, see Section 4.2.1, providing the appropriate setup for accurately capturing the pressure drop.

5.7.2 Evaluation and Discussion

The results exhibited no novel features in relation to its single-bend equivalent. As expressed previously, this also serves as a practical application illustrating that the geometrical features impose negligible minor losses. In terms of pressure and velocity along the center-line, the graphical representation can be seen in Figure 5.30-5.31. In this case the extraction of the data is similar to the *Simple Geometry* case, see Figure 3.10, where data is collected from the center-line position along the domain.

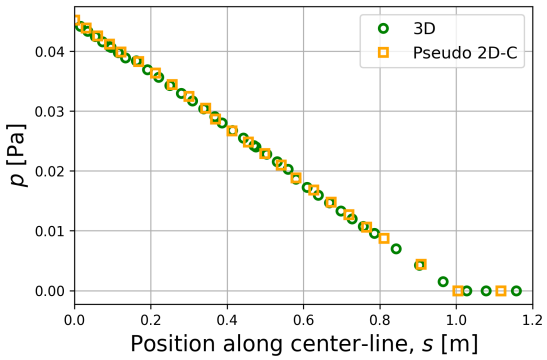

Figure 5.30: Pressure p along center-line of domain.

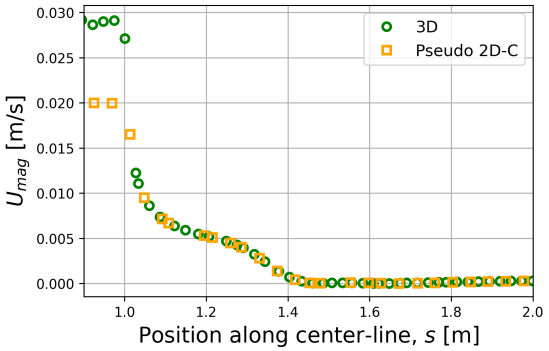

Figure 5.31: Velocity magnitude U_{mag} along center-line of domain.

In this instance, in alignment with the previous results, the *Pseudo 2D-C* model performs satisfactorily compared to the *3D* model. In terms of the pressure plot, larger irregularities can be noted compared to the sharp bend configuration at the location of the bends. The reason is that the lines constructed to serve as data extraction in STAR-CCM+, are not fully contiguous in the vicinity of the bends. Thus only the data from the straight sections of the channel are shown in the plots. Including data from the bends would have entailed needless complexity and was deemed unnecessary for the conducted analysis. Overall, based on examination of the sharp and smooth bend configurations for single and multiple bends, it was evident that the same momentum correction utilized in the *Simple Geometry* case, in Section 4.3, can be employed while achieving highly accurate results in terms of pressure drop and jet formation.

6 Case Study - Ducts

This section highlights the simulated results of the duct configurations. The conducted evaluation is presented in terms of the *Simple Geometry* and the results of the developed model using momentum correction, followed by the implementation of the geometrical features: *Multiple Bending Duct*, *Branching Duct* and *Constricted Duct*.

6.1 Evaluation of Momentum Corrections

An analysis, in accordance with the configuration of the parallel plates, was initially performed for the *Simple Geometry* case concerning ducts. This was done to evaluate if the correction of momentum in Section 4.2.2 is sufficient and yields satisfactory results in comparison to the *3D* model. The analysis was made for $Re \approx 25 - 100$ conforming with the applications of interest of Reynolds numbers typically below 100, see Section 1. To assess the validity of the initial momentum correction, i.e., the *Pseudo 2D-C* model, the obtained pressure along the channel using the momentum correction was analyzed and compared with the *3D* model. This was done by comparing the pressure gradients for various Reynolds numbers, specifically $Re \approx 25, 50, 75, 100$. The pressure gradient residual between the *Pseudo 2D-C* model, described in Section 4.2.2, and the *3D* model is depicted in Figure 6.1.

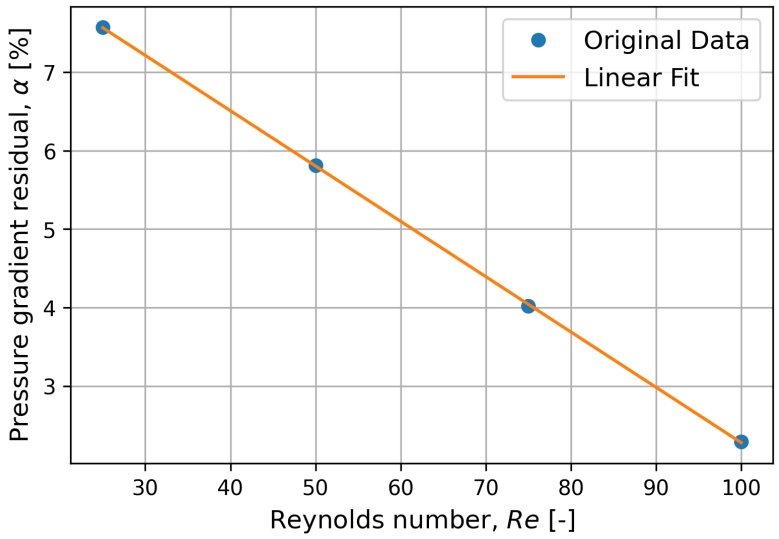

Figure 6.1: Pressure gradient residuals of *Pseudo 2D-C*, w.r.t *3D* for several Reynolds numbers.

As Figure 6.1 illustrates, there is a slight variation in pressure between the *Pseudo 2D-C* model and the *3D* model, particularly noticeable at lower Reynolds numbers. It is also evident that the residuals follow a linear trend for $25 \leq Re \leq 100$, but likely asymptotically approach zero for higher Reynolds numbers. This linear trend represents the pressure residual between the initial *Pseudo 2D-C* model and the *3D* model as a function of the Reynolds number with the range $Re \approx 25 - 100$. The resulting function, denoted as α, which is the pressure gradient residual of *Pseudo 2D-C* model w.r.t *3D* model, see Equation (6.1), serves as a correction factor additional to the field function in Section 4.2.2 to obtain better results:

$$\alpha = -0.07Re + 9.33. \tag{6.1}$$

The correction factor α was then used together with Equations (4.22) and (4.23)-(4.25), and resulted in the following *momentum source* and *momentum source derivative*:

$$S_M = -\frac{32\mu\mathbf{u}}{D_h^2} \cdot (1 - \frac{\alpha}{100}), \tag{6.2}$$

and

$$\frac{\partial S_{Mx}}{\partial u} = -\frac{32\mu}{D_h^2} \cdot (1 - \frac{\alpha}{100})\frac{\partial u}{\partial u} = -\frac{32\mu}{D_h^2} \cdot (1 - \frac{\alpha}{100}), \tag{6.3}$$

$$\frac{\partial S_{My}}{\partial v} = -\frac{32\mu}{D_h^2} \cdot (1 - \frac{\alpha}{100})\frac{\partial v}{\partial v} = -\frac{32\mu}{D_h^2} \cdot (1 - \frac{\alpha}{100}), \tag{6.4}$$

$$\frac{\partial S_{Mz}}{\partial w} = -\frac{32\mu}{D_h^2} \cdot (1 - \frac{\alpha}{100})\frac{\partial w}{\partial w} = -\frac{32\mu}{D_h^2} \cdot (1 - \frac{\alpha}{100}). \tag{6.5}$$

Using the above, Equations (6.2)-(6.5) and implementing the corresponding field functions, resulted in the following pressure along the center-line of the channel (Figure 3.10), for $Re \approx 25, 50, 75, 100$, see Figure 6.2:

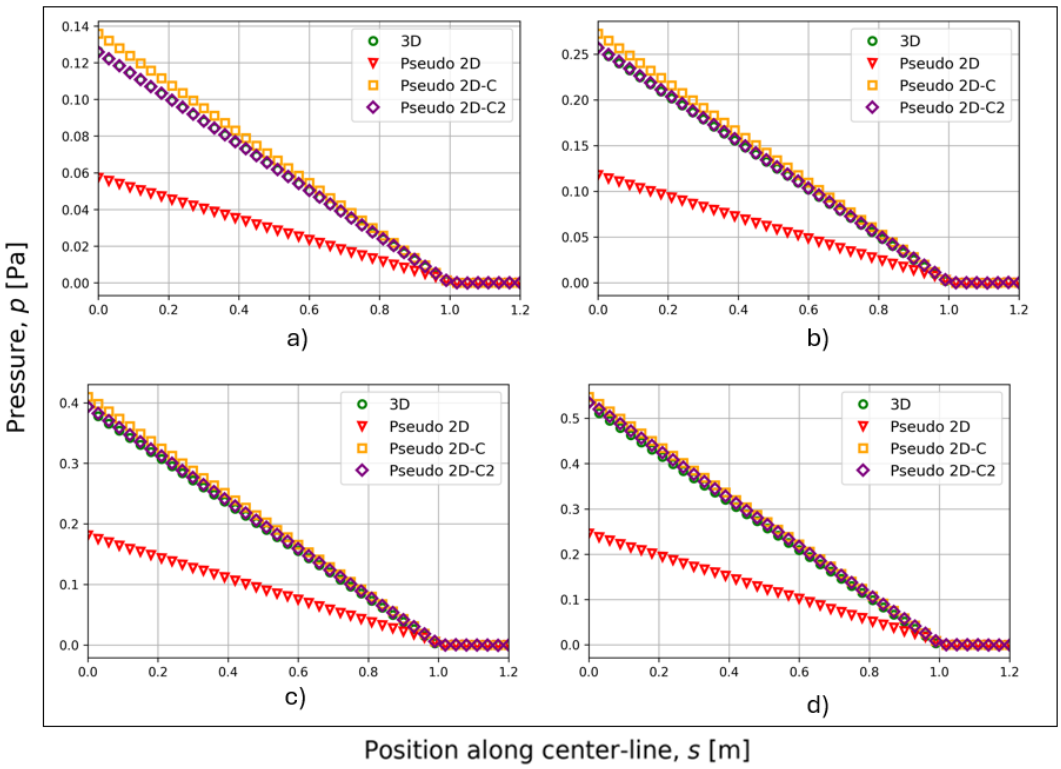

Figure 6.2: Pressure along domain for several Reynolds numbers: a) $Re \approx 25$; b) $Re \approx 50$; c) $Re \approx 75$; and d) $Re \approx 100$.

It is evident that the updated momentum corrected model, denoted as *Pseudo 2D-C2* model, is more in line with the *3D* model compared to the initial applied correction. This is anticipated as the correction is fundamentally based on the deviation between the prior model and the *3D* equivalent. It is worth noting that the *3D* data points are unseen due to the overlay of the *Pseudo 2D-C2* model data points. The slight deviation occurring for increasing Reynolds number becomes evident by comparing the figures, and the *3D* data points become revealed. The pressure residuals were plotted, based on Equation (5.5), to determine the extent of the improvement offered by the new momentum correction for the analyzed models against the *3D* model for different Reynolds numbers, see Figure 6.3.

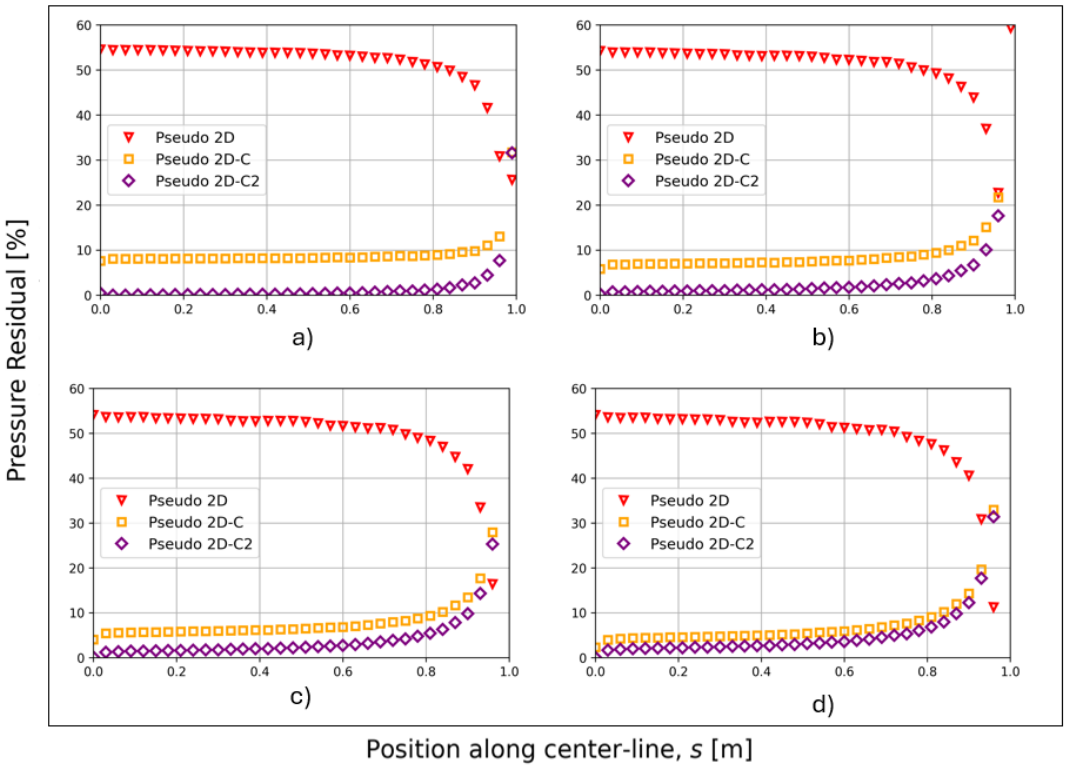

Figure 6.3: Pressure residuals w.r.t 3D, for several Reynolds numbers: a) $Re \approx 25$; b) $Re \approx 50$; c) $Re \approx 75$; and d) $Re \approx 100$.

Based on the residual plots, it becomes evident that the *Pseudo 2D-C2* model showcased better performance compared to the *Pseudo 2D-C* model, especially for lower Reynolds numbers. It is also evident that the residuals are very small, below 5% for positions below $x = 0.7\,m$ in the channel for all cases, which is considered satisfactory. However, beyond approximately $x = 0.8\,m$, the residuals start to increase significantly. This is due to the pressure dropping significantly after this position, close to zero. The pressure numerical difference in terms of absolute value is thus plotted in Figure 6.4, see Equation (5.7) on how the pressure difference is computed.

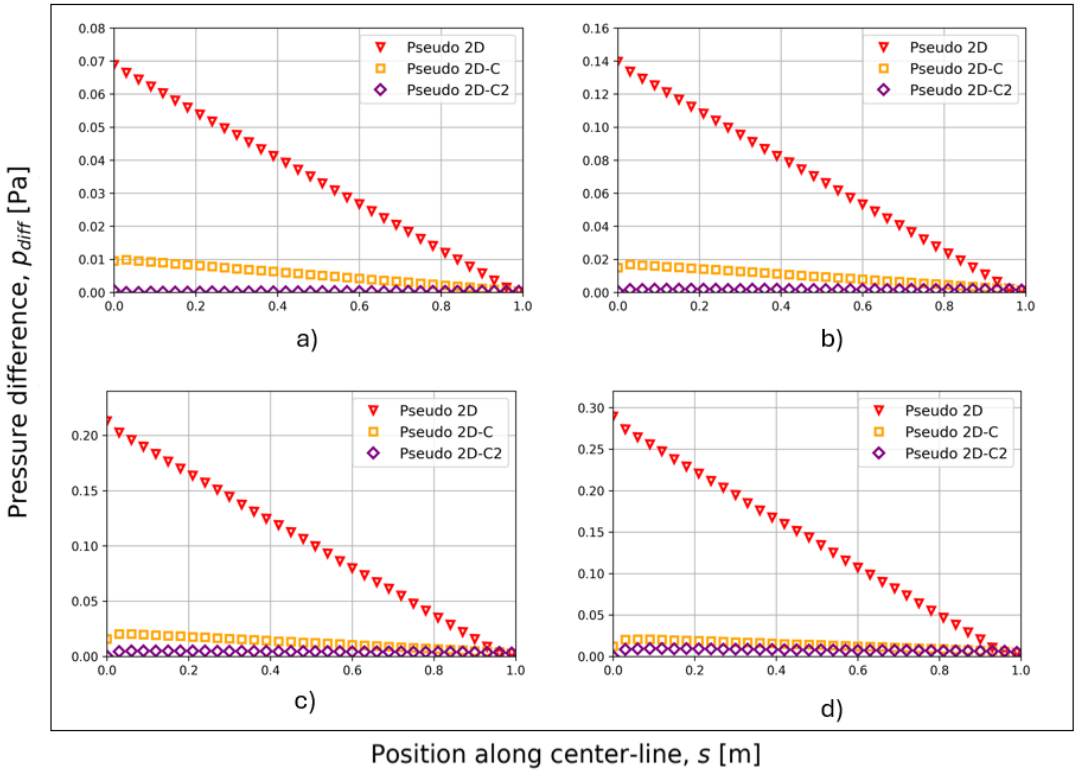

Figure 6.4: Pressure difference, p_{diff}, w.r.t *3D* for several Reynolds numbers: a) $Re \approx 25$; b) $Re \approx 50$; c) $Re \approx 75$; and d) $Re \approx 100$.

Expectedly, the pressure difference graphs further verifies that the *Pseudo 2D-C2* model behaves best in comparison to the *3D* model. As can be noted, the numerical pressure difference is significantly lower for both corrected versions in relation to the *Pseudo 2D* model. Additionally, these plots validate that the numerical pressure difference between the *Pseudo 2D-C2* model and the *3D* model is low for all cases, less than 0.01 Pa along the entire channel subdomain.

Lastly, a brief evaluation for the influence of the *denser mesh region* was conducted for the case where the channel is modeled as a *duct*. It revealed that the length of the *denser mesh region* should be equal to the entrance length of the parallel plates or approximately one and a half times the entrance length of the duct configuration, in order to get satisfactory results. Meaning, that the velocity in the room shows little to no difference when comparing the *Pseudo 2D-C* model and *Pseudo 2D-C2* model with the *3D* model. Consequently, it implies that the *denser mesh region* must be extended further for ducts than parallel plate geometries.

In conclusion, the initial momentum corrected model, the *Pseudo 2D-C* model, was evaluated and compared with the *3D* model. The comparison was made for $Re \approx 25 - 100$ and the results showed minor differences between these two models with regards to pressure and velocity along the domain. These differences were especially evident for lower Reynolds numbers. This is potentially due to the the viscous effects in the *denser mesh region* of the duct being of higher significance for lower Reynolds numbers, see Section 2.5.2, resulting in a higher pressure gradient. In order to compensate for this and achieve higher accuracy for the reduced dimensional models, the initial corrected version in Section 4.2.2 was adjusted using a correction factor α. The updated momentum correction, denoted as *Pseudo 2D-C2* model, demonstrated closer alignment with the *3D* model for all evaluated Reynolds numbers, as expected due to its derivation originating from the residual difference. Visualization of residual plots were compared and revealed satisfactory results, with residuals below 5% throughout most of the channel subdomain. Numerical pressure difference plots confirmed once again the advantage of using the updated correction model over the initial one. Overall, the updated model confirmed its effectiveness in giving satisfactory results that align well with the results obtained from the *3D* model. Lastly, a brief evaluation of the influence of the *denser mesh region* was conducted. It revealed that the length of the region should be equal to three halves times the hydraulic entrance length for ducts, in Section 2.5.4, to maintain a high accuracy.

6.2 Simple Geometry

This section highlights the findings of simulations for the *Simple Geometry* case, focusing on $Re \approx 25$ in the channel subdomain, which corresponds to an inlet velocity of $U \approx 0.033\, m/s$. In this analysis, all models, i.e., the *3D*, *Pseudo 2D*, *Pseudo 2D-C* and *Pseudo 2D-C2* are evaluated and discussed.

6.2.1 Evaluation and Discussion

For this case, the obtained contour plots show that the *Pseudo 2D-C2* model is in close alignment with the *3D* model for the pressure in the channel subdomain, demonstrated in Figure 6.6. It can also be noted that the *Pseudo 2D* model shows considerable deviation from the "correct" pressure, which is anticipated given the coarse mesh. However, upon examining Figure 6.5, it becomes apparent that the jet entering the room does not behave the same for all cases. The jet in the *3D* model deflects downwards relative to the flow direction compared to the other two cases. Several factors could contribute to this disparity, for example, undesired variation in the room's mesh or incomplete convergence of the results. Nevertheless, these differences do not affect the overall analysis and conclusions, since the deflected part of the jet is comprised of almost negligible velocity values, and the specifically evaluated data is the center-line velocity.

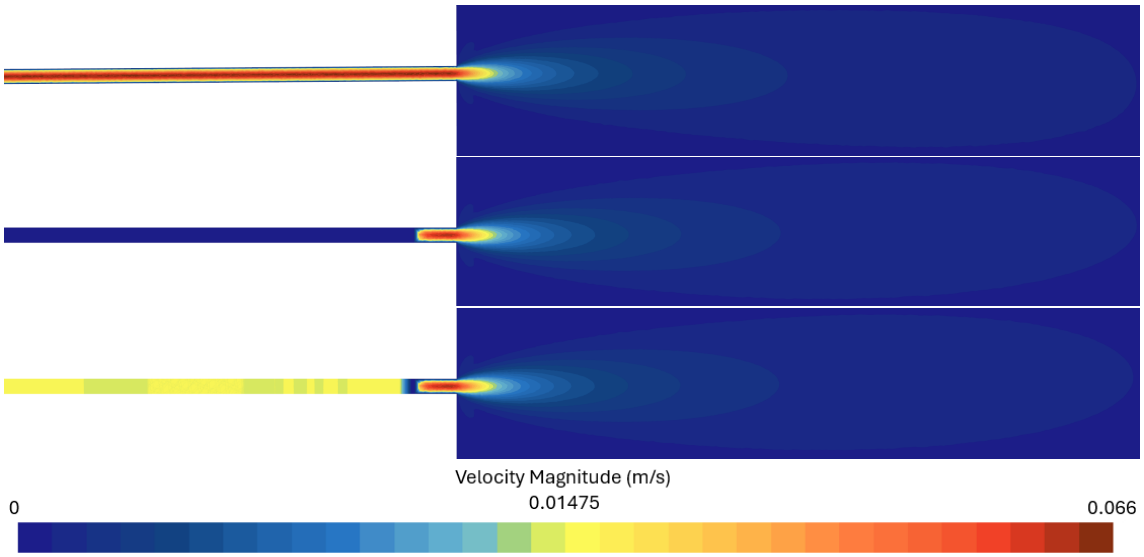

Figure 6.5: Contour plot; Velocity magnitude for *3D* model (top), *Pseudo 2D* model (middle) and *Pseudo 2D-C2* model (bottom), respectively.

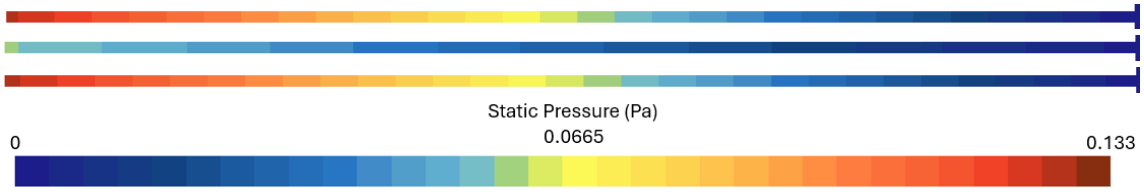

Figure 6.6: Contour plot; Static pressure for *3D* model (top), *Pseudo 2D* model (middle) and *Pseudo 2D-C2* model (bottom), respectively.

To provide a more detailed representation of the obtained results, graphs depicting the pressure and velocity along the center-line of the domain (Figure 3.10) were created, see Figure 6.7-6.8.

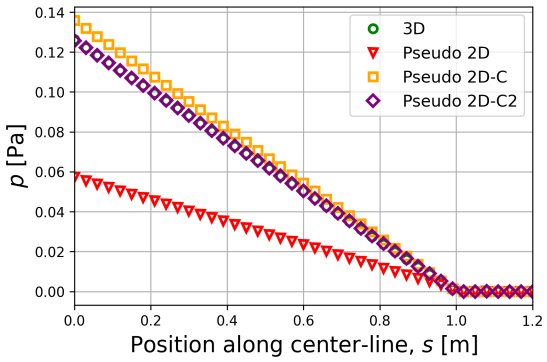

Figure 6.7: Pressure p along center-line of domain.

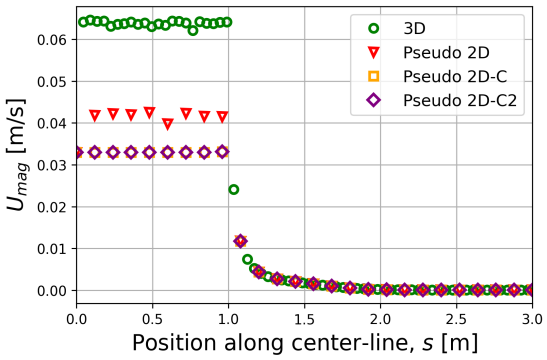

Figure 6.8: Velocity magnitude U_{mag} along center-line of domain.

The pressure values along the channel in the *Pseudo 2D* model are significantly lower in comparison to the *3D* model. This is however expected because the pressure cannot be fully resolved when employing one cell between the walls/plates, as described in Section 4.1.4. From the pressure graphs, it becomes evident that the *Pseudo 2D-C2* model exhibits the most accurate behavior, which is consistent with the expected value along the channel subdomain. See Figure 6.9 for a more accurate representation of the pressure residual, w.r.t., the *3D* model.

The velocity distribution along the center-line of the room subdomain, seen after position $x = 1\,m$ shows similar results for all the models. This indicates that the corrected models align with the fully resolved *3D* model. To further assess the velocity, a residual plot was created, see Figure 6.10, which displays the velocity residual for all models compared to the *3D* model. However, an additional, new exhibited behavior in the duct has risen, this regards the velocity magnitude for the *Pseudo 2D* model in Figure 6.8 for $x \leq 1\,m$. The difference in velocity magnitude between the models is minor, as the concern of velocity is scoped around the jet region and also reserved for the *Pseudo 2D-C* model. The noticeable difference, however, is due to one main reason. Namely, that the y-direction comprising the depth dimension is (at least) partially resolved. This means that the flow will develop a pseudo-parabolic profile in the regarded dimension due to the no-slip condition. Consequently the velocity magnitude at the center of the *Pseudo 2D* model is higher than the mean (bulk) velocity of the *Pseudo 2D-C/C2* model.

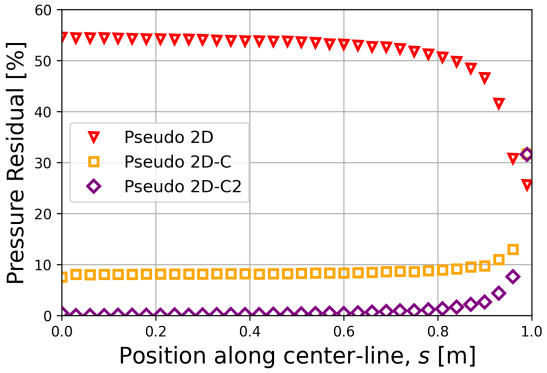

Figure 6.9: Pressure residuals, w.r.t., *3D*.

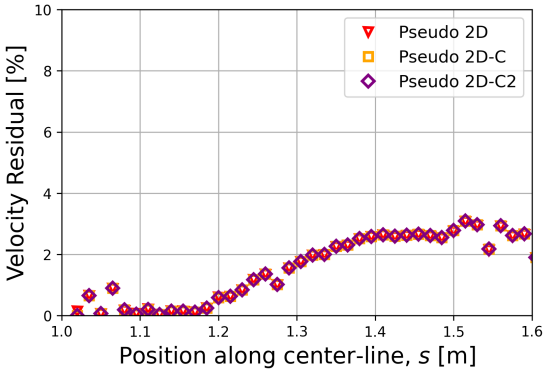

Figure 6.10: Velocity residuals, w.r.t., *3D*.

Regarding the pressure, the *Pseudo 2D-C2* showcased better performance compared to the *Pseudo 2D-C* model based on the residual plots. The residuals are also within acceptable margins, below 5% for positions below $0.9\,m$. However, at the channel end the residuals start to increase exponentially due to the pressure dropping to values near zero. The velocity residuals are also within an acceptable limit, below 3% for all models from position $x = 1\,m$ (where the jet enters the room) until position $x = 1.6\,m$, $0.6\,m$ downstream in the room from the jet entrance. After this point, the residuals start to increase significantly since the velocity values drop near zero. In order to get a representation of the actual numerical difference for the pressure and velocity by comparing the *Pseudo 2D-C/C2* models and the *3D* model, Figures 6.11- 6.12 are shown.

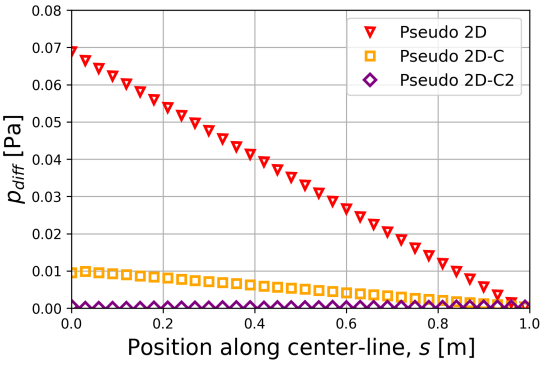

Figure 6.11: Pressure diff., p_{diff}, w.r.t., *3D*.

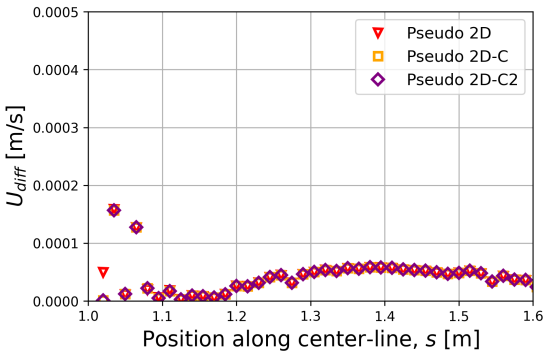

Figure 6.12: Velocity diff., U_{diff}, w.r.t., *3D*.

The graphs depicting the numerical difference for the pressure and velocity further validate that the *Pseudo 2D-C2* model is an appropriate replacement of the *3D* model. As can be noted, the numerical pressure difference is significantly lower for both corrected versions compared to the *Pseudo 2D* model. The plot illustrating the pressure difference shows that the numerical pressure difference between the *Pseudo 2D-C2* model and the *3D* model is minimal, meaning that it could be considered negligible. It is also worth noting that the velocities across all models are identical as a consequence of the same mesh settings employed within the room subdomain. This is also supported by having a sufficiently large *denser mesh region*. This allows the flow to develop fully for the *Pseudo 2D* models before entering the room subdomain. The cell count in the channel subdomain is significantly lower for the *Pseudo 2D* mesh compared to the *3D* counterpart, as shown in Table 6.1.

Table 6.1: Cell count comparison (channel) - *Simple Geometry*.

3D	***Pseudo 2D***	**Relative cell amount [%]**
629 116	9 023	1.43

In summary, this section presents an analysis conducted for $Re \approx 25$ in the channel subdomain, corresponding to an inlet velocity of $U \approx 0.033\,m/s$. The contour plots illustrating the pressure show that the *Pseudo 2D* model deviates significantly compared to the *3D* model. The *Pseudo 2D-C2* does, however, match the *3D* model with high accuracy. The velocity contour plots reveal that the jet for the *3D* model experiences a downward deflection compared to the other models, but this does not affect the overall analysis. This was confirmed after evaluating the velocity values along the center-line of the domain. Residual plots were also constructed and showcased the residuals (in percent) between the analyzed models in comparison with the *3D* model. According to these plots, the *Pseudo 2D-C2* model displayed a slight increase in accuracy compared to the *Pseudo 2D-C* model. Graphs illustrating the numerical difference of the velocity and pressure in comparison to *3D* model were also plotted, revealing the advantage of using the *Pseudo 2D-C2* model over both the *Pseudo 2D-C* and the *Pseudo 2D* model, see Figures 6.11-6.12 . The low relative cell amount also shows promise of a potential in attaining high computational efficiency and faster simulations for this type of geometrical configuration.

6.3 Multiple Bending Duct

To evaluate the performance of the developed models for duct-related features, a new geometrical component was constructed. This feature incorporates four smooth bends, where all three dimensions are utilized. Here, the multi-dimensional aspect serves as the unexplored attribute between this geometry and the ones incorporated in Section 5.6 and 5.7. The main reason of utilizing all three dimensions is to assure that all arbitrarily bent channel-related geometries are applicable for the *Pseudo 2D-C/C2* models and that no novel undesired features are attained. The channel subdomain contains part-wise straight sections of $0.25\,m$ in length, originating from the room and consequently, with an exception of the last section's length corresponding to the remaining center-line length of $1\,m$. The details in regards to the geometry can be seen in Figure 6.13.

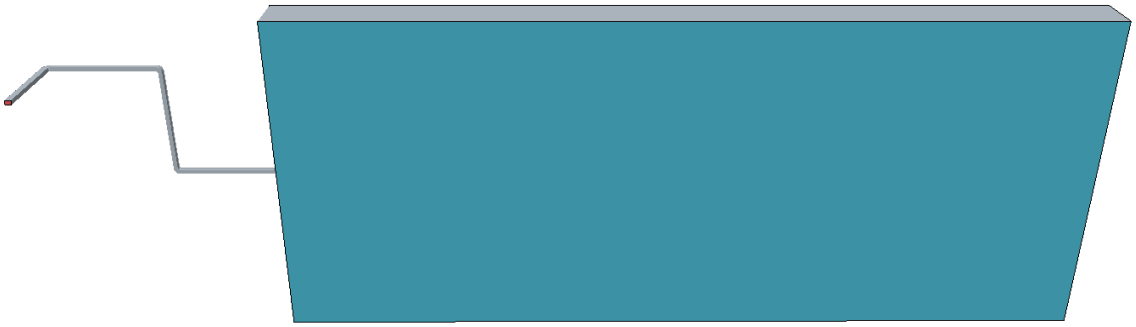

Figure 6.13: *Multiple Bending Duct* geometry.

6.3.1 Mesh Generation

The mesh implementation is similar to that of the *Simple Geometry* for the duct, see Section 3.6. The same settings in the channel and room subdomain were employed herein and the same mesh aspects apply. Namely, that the *3D* and *Pseudo 2D* mesh for the *Multiple Bending Duct* case contain matching mesh settings for the room subdomain. Furthermore, in the *Pseudo 2D* mesh, one cell was attained between the walls, in the orthogonal direction of the flow, through most of the channel except in the bends, where small tetrahedral elements were unavoidably obtained. The unstructured characteristic in the mesh is potentially stemming from the increased coherent geometrical channel complexity. This feature was also exhibited in the bend-related geometries of the parallel plates configuration, to various extents, varying between the *Single Smooth Bend* and the *Multiple Smooth Bends* geometries. The resulting mesh is visualized in Figure 6.14. See Table 6.2 for an illustration of the cell count and relative cell reduction in the channel subdomain.

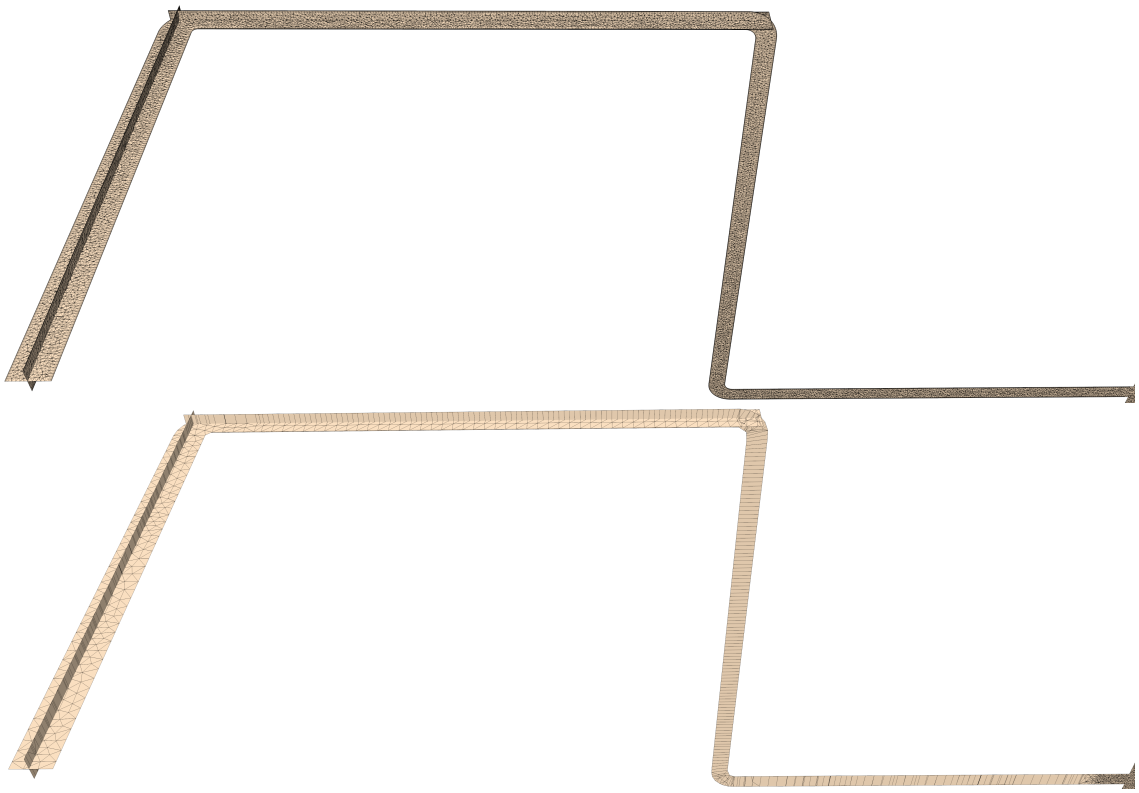

Figure 6.14: *Multiple Bending Duct*, *3D* and *Pseudo 2D* mesh in channel subdomain.

Table 6.2: Cell count comparison (channel) - *Multiple Bending Duct*.

3D	***Pseudo 2D***	**Relative cell amount [%]**
639 235	9 304	1.46

The *momentum source* and *momentum source derivative* field functions were applied within the channel subdomain except the intermediate *denser mesh region*, consistent with the equivalent utilized in the *Simple Geometry* for the duct, as described in Section 6.1.

6.3.2 Evaluation and Discussion

The analysis of multiple bends in a three-dimensional setting, showed, in alignment with the previously tested geometries, that the same method employed in the *Simple Geometry* for the duct produces good results for the *Pseudo 2D-C/C2* models. The *Pseudo 2D-C2* model is in close alignment with the *3D* model both in terms of pressure and velocity along the center-line of the channel and the room subdomain, as illustrated in Figures 6.15 and 6.16. These graphs also confirm that the corrected versions are applicable even when the flow is exerted by all three directions. The difference between the corrected models and the *3D* model is depicted by the maximum residual at the inlet pressure. This is calculated using Equation (5.5). For the *Pseudo 2D-C* model, the calculated residual is $\epsilon^* \approx 7.4\%$, while for the *Pseudo 2D-C2* model, it is approximately 0.4%, showing that the correction factor α improves the accuracy of the approximated pressure drop. In this case, the data displays the center-line properties, similar to the *Simple Geometry* case, see Figure 3.10 for an illustration of the domain location of the data.

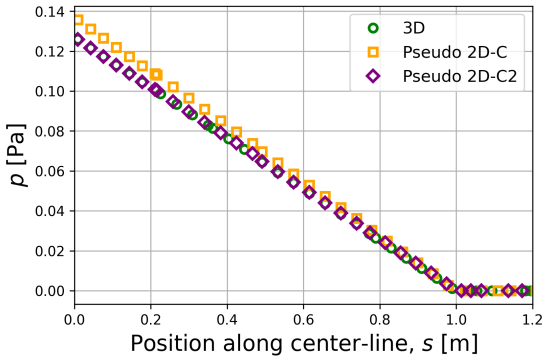

Figure 6.15: Pressure p along center-line of domain.

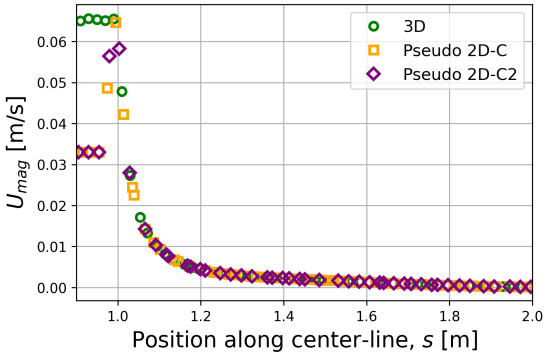

Figure 6.16: Velocity magnitude U_{mag} along center-line of domain.

6.4 Branching Duct

Further evaluation of the developed model's applicability was conducted. A branching duct-system was modeled to extend the perspective of the tests as it is entailed by a feature unseen in the prior configurations, namely a division of mass flow. This idea was believed to provide new insights to the reduced dimensional modeling. Consequently, the *Branching Duct* geometry was created.

For preserving generality and a high degree of applicability, a simple T-junction with a bend was constructed. As a result of this, the room subdomain was widened to ensure full accommodation of the, two three-dimensional jets forming. The details regarding the geometrical configuration are displayed in Figure 6.17.

Figure 6.17: *Branching Duct* geometry.

6.4.1 Mesh Generation

The construction of the mesh was performed in alignment with that of the *Simple Geometry* for the duct. However, due to the branching of channels and the slight alterations in terms of the room subdomain, the control volumes were adjusted to encompass the important regions. Through an iterative process, involving readjustment of the mentioned controls and observation of the formed jets, significant reductions in cell count were attained, mainly in the jet regions. Resultingly, the computational resources were optimized for the significantly smaller jets. The resulting mesh and specific details can be found in Figure 6.18. The resulting *Pseudo 2D* mesh displayed, to a varying extent, regions of unstructured characteristics. Despite having a continuously identifiable thickness, due to its increased geometrical complexity, it failed to retain a single cell configuration in the z-direction throughout large parts of the channel subdomain. The reduction of cell amount is highlighted in Table 6.3 and shows that the required amount of cells in the *3D* mesh becomes higher as the total volume of the channel increases as a result of the branching of the duct. However, a slight increase in both meshes can be seen and the resulting relative cell amount becomes similar to the previously seen statistics for the other geometrical features.

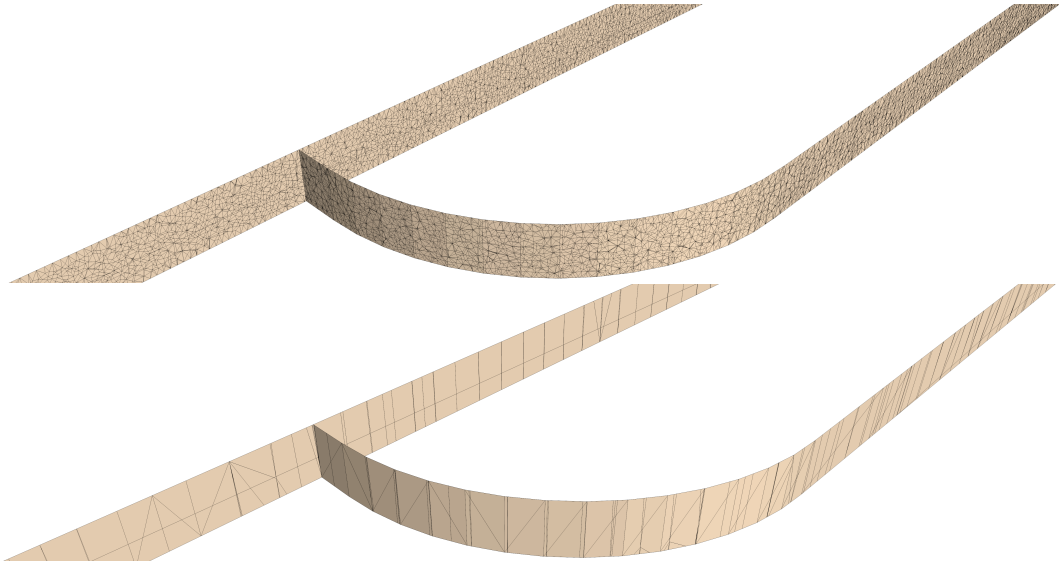

Figure 6.18: *Branching Duct*, *3D* and *Pseudo 2D* mesh showing branched part.

Table 6.3: Cell count comparison (channel) - *Branching Duct*.

3D	***Pseudo 2D***	**Relative cell amount [%]**
811 505	6 797	0.84

The *momentum source* and *momentum source derivative* field functions were applied throughout the channel subdomain with the exception of the *denser mesh region*, consistent with the one utilized in the *Simple Geometry* for the duct, described in Section 6.1. The implemented *momentum source* in the *Pseudo 2D-C2* model, is displayed in the Section 4.2.2. Noteworthy, is that no specific concern to the geometrical feature was taken and thus remained identical to the *Simple Geometry* of the duct in the regarded aspect.

6.4.2 Evaluation and Discussion

The results of the conducted simulations are graphically depicted in this section. Due to the branching of the duct, the display of data differs from the other analyzed geometrical features. Instead, the data are presented for each flow path; the straight path and the curved path, see Figure 6.19.

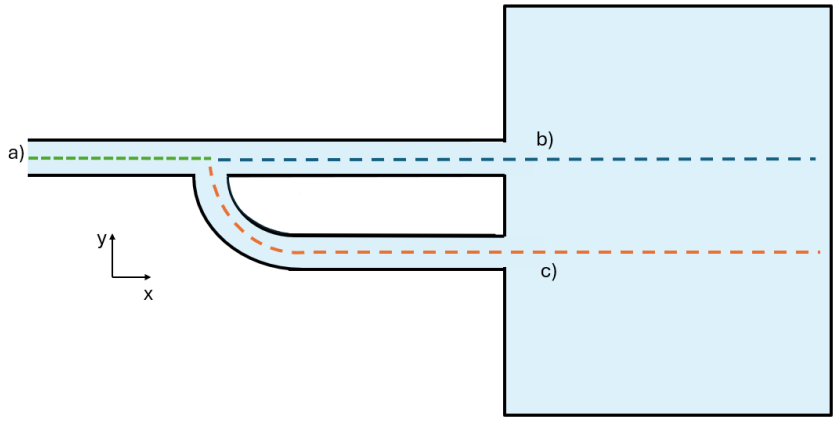

Figure 6.19: Sketch of *Branching Duct* with an illustration of flow paths. The composition, w.r.t., path is as follows: the straight path of a) and b); the curved path of a) and c).

Figures 6.20-6.21 show the data extracted from the straight flow path, the data for the curved flow path are displayed in Figures 6.22-6.23.

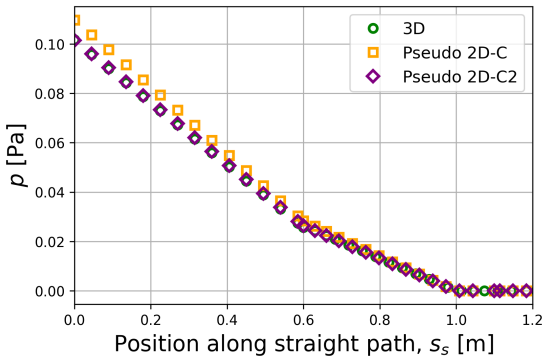

Figure 6.20: Pressure p along center-line of straight path.

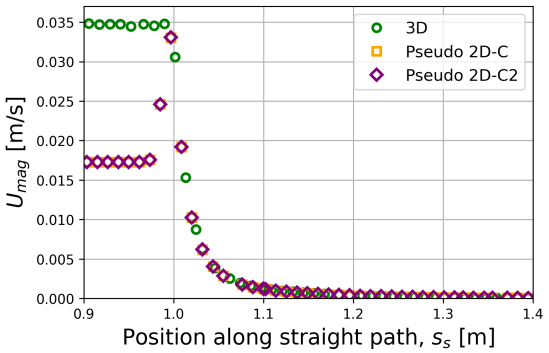

Figure 6.21: Velocity magnitude U_{mag} along center-line of straight path.

From the above plots, displaying the pressure and velocity distribution along the straight path, it can be concluded that both *Pseudo 2D-C/C2* models are similar in comparison to the *3D* model. The *Pseudo 2D-C2* model which utilizes the correction factor α, described in Section 6.1, further improves the obtained results in terms of pressure and almost fully coalign with the benchmarking data points of the simulated *3D* model. The difference between the corrected models and the *3D* model is further depicted by the maximum residual at the inlet pressure. This was calculated using Equation (5.5). For the *Pseudo 2D-C* model, the calculated residual became $\epsilon^* \approx 7.8\%$, while for the *Pseudo 2D-C2* model it was approximately 0.3%, showing that the correction factor α improves the accuracy of the approximated pressure drop in this case as well.

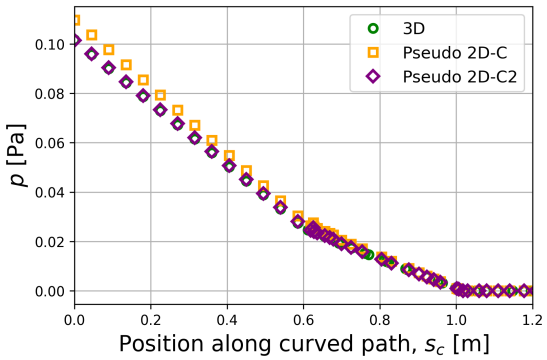

Figure 6.22: Pressure p along center-line of curved path.

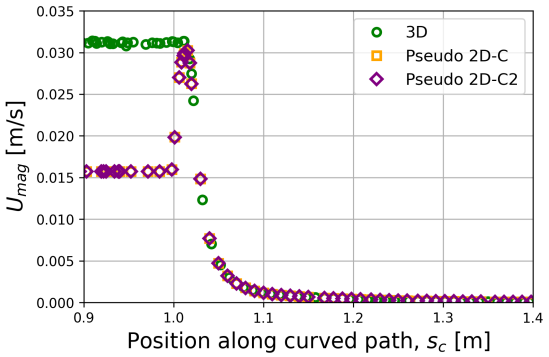

Figure 6.23: Velocity magnitude U_{mag} along center-line of curved path.

For an asymmetrical pipe system, with transitions from one to two pipes, the mass flow must be conserved [30]. Mathematically, this can be expressed by the following:

$$\dot{M}_1 = \dot{M}_2 + \dot{M}_3, \tag{6.6}$$

where $\dot{M}$ denotes the mass flow. The indices 1, 2, and 3 represent: the upstream section of the pipe before the branching, the straight section downstream of the branching, and the curved path downstream of the branching, respectively. The distribution of mass flow between the pipes is displayed in Table 6.4 for the *3D* model and in Table 6.5, respectively.

Table 6.4: Mass flow at different positions for *3D* model.

Position	**Mass flow [kg/s]**
Single Pipe Section, $s = 0.5m$	$5.84 \cdot 10^{-6}$
Straight Pipe Section, $s_s = 0.8m$	$3.05 \cdot 10^{-6}$
Curved Pipe Section, $s_c = 0.8m$	$2.76 \cdot 10^{-6}$

Table 6.5: Mass flow at different positions for *Pseudo 2D-C/C2* model.

Position	**Mass flow [kg/s]**
Single Pipe Section, $s = 0.5m$	$5.86 \cdot 10^{-6}$
Straight Pipe Section, $s_s = 0.8m$	$3.07 \cdot 10^{-6}$
Curved Pipe Section, $s_c = 0.8m$	$2.79 \cdot 10^{-6}$

The distribution caused by the asymmetry and the configuration in the pipe junction is also apparent by the different velocity magnitudes in the paths along the center-lines and the resulting jet formations. This can be seen by observation of, e.g., the two peaks in velocity magnitude, of $\approx 0.035\, m/s$ and $\approx 0.031\, m/s$ at $x = 1\, m$ in Figures 6.21 and 6.23. With concern to the mass flow beyond the branching feature it is evident that the *Pseudo 2D-C/C2* models capture this attribute as well. Thus, concluding that the division of mass flow sufficiently by the reduced dimensional model. This further supports the downstream desired features in terms of the peak of velocity at the exit but also the ability to maintain accuracy along the jet center-line.

From observation of Equation (6.6) and Table 6.4-6.5 it becomes evident that the data does not perfectly match the presented relation. Although, this in-equivalency is due to a minor data extraction intricacy. Namely, that the data averaged over the cross-sectional area to compute the mass flow, is taken from the intersected cell-centered values and not space-interpolated ones. Consequently, the mass flow from the simulations, denoted $\dot{M}_{1,sim}$, $\dot{M}_{2,sim}$ and $\dot{M}_{3,sim}$, are still perceived to hold for the mass conservation and align with the theoretical values such that

$$\dot{M}_{1,sim} = 5.84 \cdot 10^{-6} \approx \dot{M}_1,$$

and

$$\dot{M}_{2,sim} + \dot{M}_{3,sim} = 3.05 \cdot 10^{-6} + 2.76 \cdot 10^{-6} \approx \dot{M}_{1,sim}.$$

The decrease in the gradient of the pressure drop, displayed for both paths in Figures 6.20-6.22, can both be attributed to the decrease in flow velocity and consequently less momentum loss throughout each path respectively. As the fluid travels along the path with the least resistance, the straight and curved path are ensured to reach an equal state in this regard. Consequently, the pressure drops for both paths become equal.

6.5 Constricted Duct

To improve upon the knowledge of the applicability of the developed correction-based models, a final duct-related geometry was constructed. This is motivated by the fact that the previously tested configuration required no specific geometrical treatment in the *Pseudo 2D-C/C2* model, and the accuracy without the inclusion of the correction factor α was considered good enough. It was initially suggested that large variations in cross-sectional area along the channel could spark the need to put specific concern in the employed *momentum source*. The main reason is that a decrease in cross-sectional area leads to local steep velocity and pressure gradients. Resultingly, the *Constricted Duct* was created.

Due to the limitations of the *Thin Mesher*, the highest cross-sectional area ratio achieved between the until now used duct and the constricted section with a consistent *Pseudo 2D* mesh was 4:1. This was attained without the specific adjustments of *Thin Mesher Expert settings*. The encountered limitations and justification are addressed in Appendix F. The geometry used for evaluation of the constricted feature can be seen in Figure 6.24.

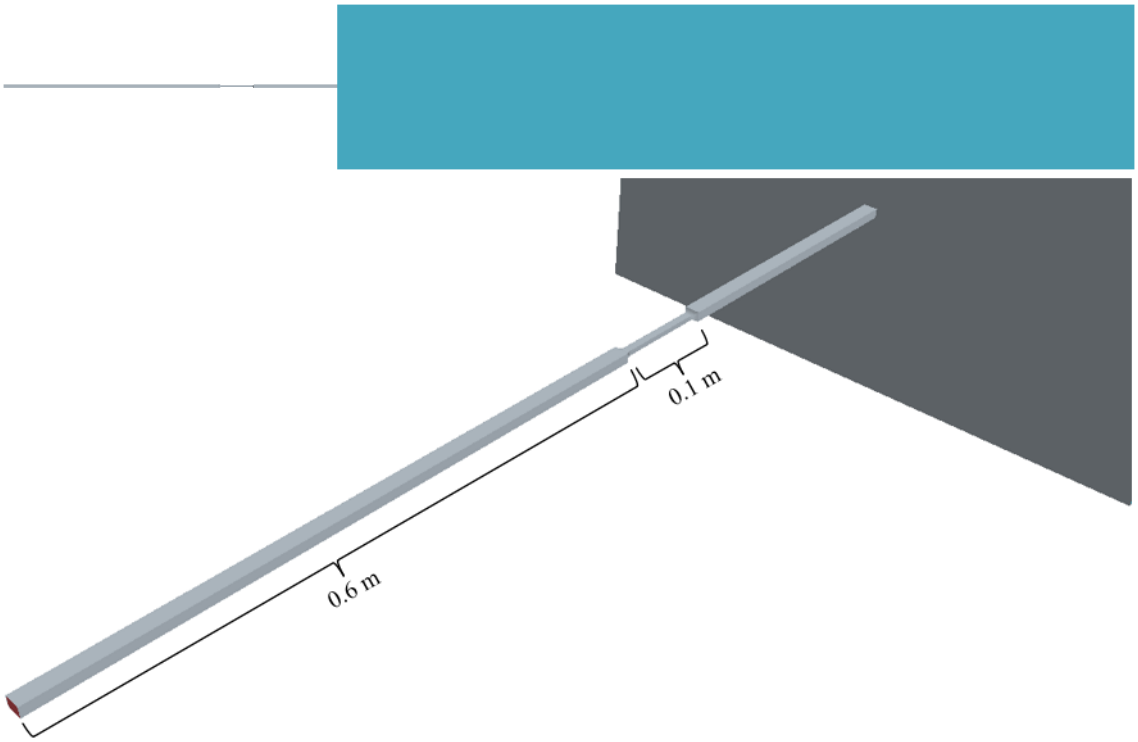

Figure 6.24: *Constricted Duct* geometry in xz and channel subdomain, respectively.

6.5.1 Mesh Generation

Due to the expected local velocity increase in the constricted region, a mesh control volume for the *3D* model was set, encompassing the concerned section of the channel. This was done to ensure an appropriate resolution mainly in the transitions between large-to-small and small-to-large cross-sectional areas, as these regions exhibit high velocity and pressure gradients. This lead to the exclusion of prism layers in the mesh generation as the enforced tetrahedral cells are smaller than specified inflation layer settings for the constricted section. Graphical depictions of the mesh in the constricted part can be seen in Figure 6.25.

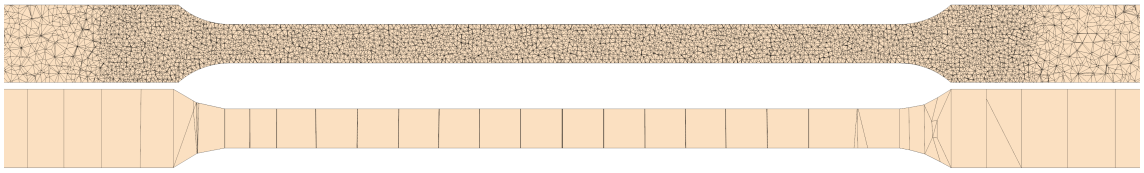

Figure 6.25: Constricted part mesh for *3D* and *Pseudo 2D*.

For more information regarding the achieved cell amount reduction, Table 6.6 details the regarded mesh statistics, w.r.t., the *Pseudo 2D* mesh and the *3D**. Herein, the *3D** denotes the mesh with the refinement encompassing the constricted section. With no mesh improvement in the region of decreased cross-sectional area and consequently not an established mesh-independence, the total channel cell amount was 544 360.

Table 6.6: Cell count comparison (channel) - *Constricted Duct*.

3D*	***Pseudo 2D***	**Relative cell amount [%]**
855 343	8 942	1.05

The correction of the model in terms of field function implementation differs slightly from the *Simple Geometry* for ducts. Here, specific concern was put on one additional aspect, namely the variations in hydraulic diameter. This was achieved by formulating an additional field function that specifies the cross-sectional variations, w.r.t., x. Here, x and s are interchangeable as the channel subdomain starts at $x = s = 0$ and is aligned with the x-axis. With the standard hydraulic diameter value $D_{h,0} = 0.012\,m$ and the constricted section's reduced equivalent $D_{h,con} = 0.006\,m$ the following piece-wise function was constructed:

$$D_h = \begin{cases} D_{h,0}, & x < 0.6 \text{ or } x > 0.7, \\ D_{h,con}, & 0.6 \leq x \leq 0.7. \end{cases}$$

The above relation was used in the *momentum source* and *momentum source derivative*, in Equation (6.2).

6.5.2 Evaluation and Discussion

Figures 6.26-6.27 display the velocity and pressure contour plots, while Figures 6.28-6.29 display the simulated results for the *3D* model and the reduced dimensional models, the *Pseudo 2D-C* and the *Pseudo 2D-C2* model. The first showcases the pressure along the domain, and the latter displays the velocity for the transitioning region between channel to room, both following the center-line. The extraction of the data is similar to the *Simple Geometry* case, see Figure 3.10, where data is collected from the center-line position along the domain.

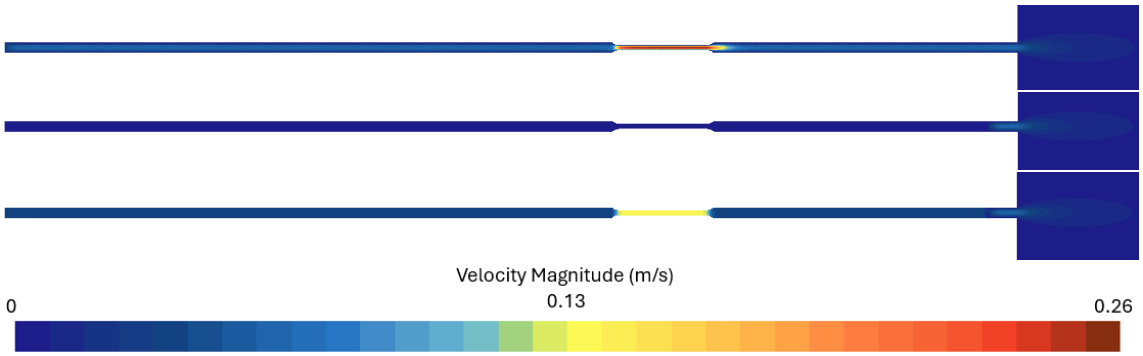

Figure 6.26: Contour plot; Velocity magnitude for *3D* model (top), *Pseudo 2D* model (middle) and *Pseudo 2D-C2* model (bottom), respectively.

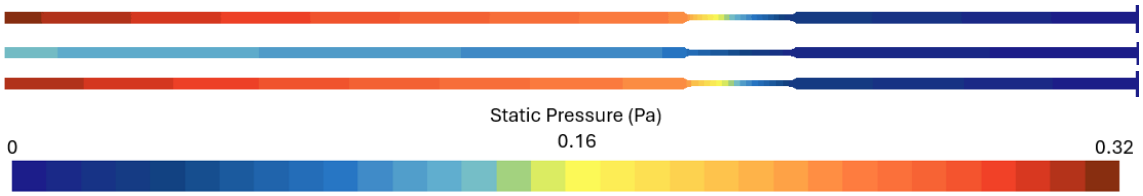

Figure 6.27: Contour plot; Static pressure for *3D* model (top), *Pseudo 2D* model (middle) and *Pseudo 2D-C2* model (bottom), respectively.

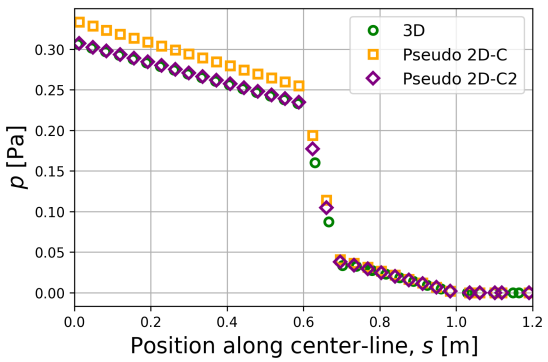

Figure 6.28: Pressure p along center-line of domain.

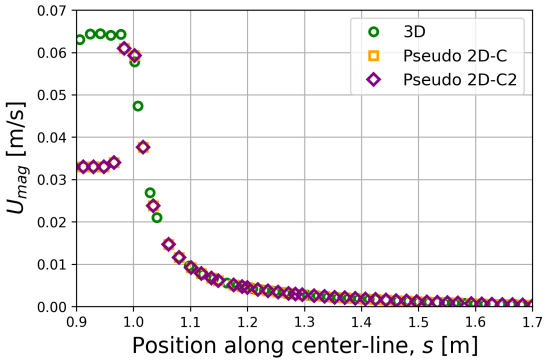

Figure 6.29: Velocity magnitude U_{mag} along center-line of domain.

Both corrected models show good behaviour in terms of similarity to the *3D* model. Regarding the velocity along the center-line in the jet region, the simulated data from the models are graphically indistinguishable.

As previously explained, a substantial reason of the inclusion of this geometrical feature was to induce stress onto the model, and enforce a need of the specified *momentum source* to achieve desirable accuracy. However, when considering variations in hydraulic diameter throughout the duct, specified as a field function and incorporated in the field function for the *momentum source* and *momentum source derivative*, both the corrected models perform well. Another concluding remark is that the correction factor α is necessary for achieving desirable accuracy. This can be noted by observing the vertical displacement of the *Pseudo 2D-C* in comparison to the *Pseudo 2D-C2* in the above pressure-plot. Without the inclusion of it, for $x \in [0, 0.6]$ prior to the constricted section, the pressure values deviate by $\epsilon^* \approx 9\%$ for the *Pseudo 2D-C*. The correction factor α improved the accuracy to $\epsilon^* \approx 0.2\%$. The computed residuals are both based on Equation (5.5) with the evaluation based on inlet pressure.

7 Pin-Fin: Application and Analysis

The analysis of the *Pin-Fin* geometry demonstrates the previously developed methods' implementation onto more advanced and complex geometrical features. This was done to extend the perspective of the testing and provide new insights, in terms of, e.g., velocity and pressure distribution. Furthermore, it was also conducted to evaluate the applicability of a *momentum source* correction in cases involving abrupt changes in velocity along the channel subdomain. This new geometrical feature was evaluated by the construction of a detailed mesh and by developing a reduced-order model, i.e., a small section of the channel subdomain. A momentum correction analysis was conducted by analyzing the pressure drop for $Re \approx 25 - 100$. Lastly, a comparison of the simulation results was made for the fully resolved *3D* model, *Pseudo 2D* model, and the corrected reduced dimensional model, respectively.

7.1 Set Up

The *Pin-Fin* geometry was created based on the *Simple Geometry* for the duct and thus adopted its boundary conditions. The implementation of pin-fins was achieved by the addition of multiple holes across the channel. The resulting circular voids, served as the *Pin-Fin* feature, as the constructed geometry comprised the fluid domain, rather than the physical object itself. In the observed case, the pin-fins were arranged in an aligned and symmetrical manner, where the distance between each pin-fin is the same both in the y and x- direction, i.e., the perpendicular (depth) and parallel direction of the flow, respectively. The distance between the center points of each pin-fin in the x-direction was set to $0.01\,m$ while the distance in the y-direction was set to $0.005\,m$. The diameter of each pin-fin was set to $0.003\,m$ with three pin-fins along each row. For the graphical illustration, see Figures 7.1-7.2.

Figure 7.1: *3D* model demonstrating the whole channel in xy plane for *Pin-Fin* geometry.

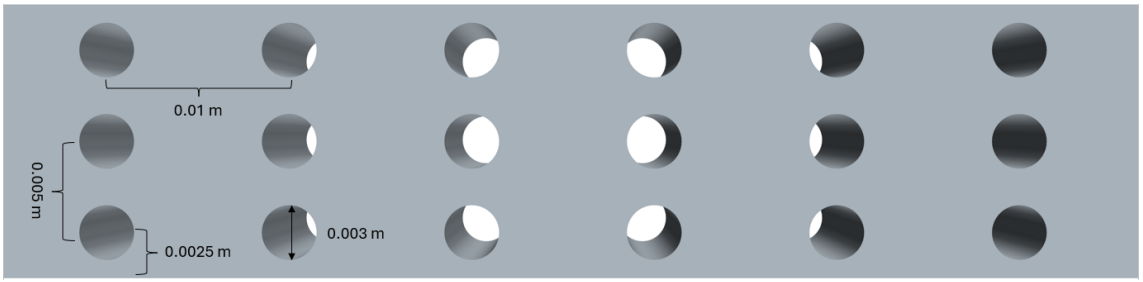

Figure 7.2: Dimensions for the *Pin-Fin* geometry in the channel subdomain.

For this geometry, the mesh generation was different. A fine mesh was necessary to fully resolve the *Pin-Fin* channel geometry. This level of detail was essential to capture the complex flow patterns and the interactions between the flow and the pin-fins. By using the same mesh settings as the *Simple Geometry* for the duct but decreasing the cell size in the channel, the number of cells in the subdomain became 43 866 781 and the total number of cells throughout the whole domain became 48 438 131, which is a significant increase compared to the previous geometrical configurations. The mesh of the *3D* geometry can be seen in Figure 7.3. It is worth noting that there are no prism layers in the channel subdomain. The reason for this is that the cells are very small, in fact smaller than the prism elements used in the parallel-plate and duct cases. This resulted in the exclusion of the prism layers during mesh generation. Due to the low Reynolds number for all evaluated cases, it is essentially redundant to have prism layers. Commonly implemented to provide better resolution in the boundary layers, the viscous effects are minimal and the velocity changes uniformly according to Figure 2.4 in Section 2.5.3 near the walls for such small Reynolds numbers.

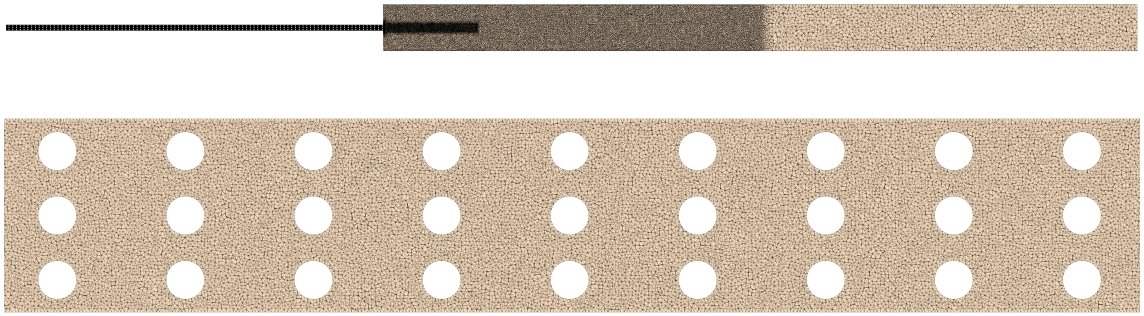

Figure 7.3: Inner mesh in xy plane for the full *3D* model and small part of the channel subdomain.

To get a better representation of the simulation results without excessive computational expense, a small section of the channel, with a length corresponding to the *denser mesh region*, i.e., $L_{DSM} \approx 0.03\,m$ for the duct geometries, was created, referred to as *small section-channel*. A fully-developed interface between the inlet and the outlet of the section was created with a periodic boundary condition, with a specified mass flow that equals the inlet velocity of $v = 0.033\,m/s$ corresponding to an inlet Reynolds number of approximately 25. The mesh was generated in an iterative manner, ensuring convergence of pressure and velocity simulation results, leading to a mesh containing 2 798 966 cells, see Figure 7.4. Since the *small section-channel* is only $0.03\,m$ long, the amount of cells needed for a similar order of accuracy would be significantly higher than the one used in the non-periodical based *3D* model. With the assumed mesh configuration settings, the grid-system would have to be comprised of $2\,798\,966 \cdot \frac{1m}{0.03m} \approx 93$ million cells in the channel to ensure full convergence of the velocity and pressure. However, to avoid such computational effort the *small section-channel* will be addressed in the following.

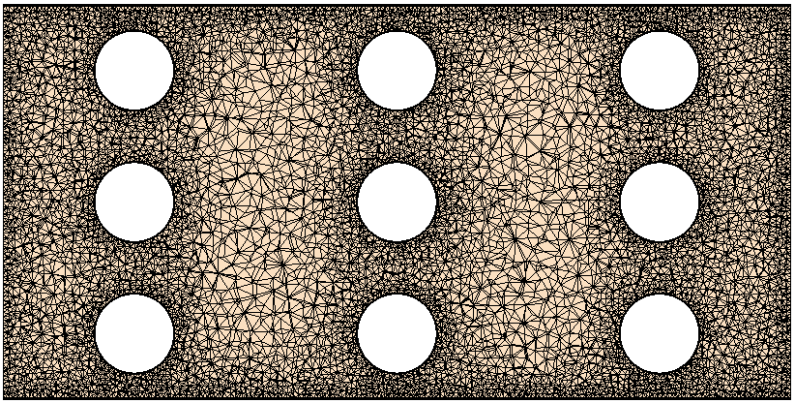

Figure 7.4: Inner mesh in xy plane for the *small section-channel* model.

Since the *Pin-Fin* feature required a fine mesh to accurately capture the intricate details and the circular shape, it was not possible to achieve a *Pin-Fin* configuration in the *Pseudo 2D* mesh across the whole channel. Instead, the region with a single cell configuration maintained the same channel shape as the *Simple Geometry* for duct and the *Pin-Fin* was geometrically included within the *denser mesh region*. This *denser mesh region* was constructed with the identical mesh settings as the *small section-channel*, see Figure 7.5. The *Pseudo 2D* mesh resulted in 2 694 345 cells in the channel and 7 436 507 cells in total. Table 7.1 is included to visualize the cell count for each model type, i.e., *3D*, *small section-channel* and the *Pseudo 2D* model, respectively.

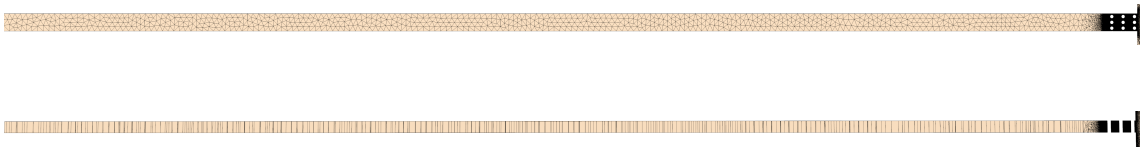

Figure 7.5: Inner mesh for the channel subdomain in xy and xz plane for the *Pseudo 2D* model, respectively.

Table 7.1: Number of cells for different mesh types of *Pin-Fin* geometry.

Mesh Type	Number of cells: Channel	Number of cells: Total
***3D* model**	43 866 781	48 438 131
***Small section-channel* model**	-	2 798 966
***Pseudo 2D* model**	2 794 345	7 536 507

7.2 Momentum Source Correction Analysis

Due to the higher resolution of the *small section-channel* and the lack of feasibility in having a similar resolution of the full three-dimensional model, the validation was made based on the *small section-channel* model. The evaluation was conducted for $Re \approx 25 - 100$ for the same reason as the previous ones, i.e., to determine the residuals' Reynolds number dependency. After assessing the small section, a *momentum source* correction was obtained by determining the pressure drop across this section using the following relation:

$$\frac{\Delta p}{\Delta l} = \frac{p_{in} - p_{out}}{L - 0}, \tag{7.1}$$

where p is the pressure, l is the considered length, p_{in} the upstream pressure, p_{out} the downstream pressure, both, w.r.t., the length of the *small section-channel*, and L the total length of the section. Equation (7.1) calculates the pressure drop by subtracting the outlet pressure with the inlet pressure and divides this difference with the length of this section, i.e., $0.03\,m$.

The pressure drops acquired for varying Reynolds numbers are illustrated in Table 7.2, as follows:

Table 7.2: Pressure drop for $Re \approx 25 - 100$.

Re	Pressure drop [(]Pa/m]
≈ 25	2.04
≈ 50	4.58
≈ 75	7.49
≈ 100	10.63

The pressure drops were then plotted, see Figure 7.6. The plot demonstrates the pressure drop as a function of the Reynolds number, where the Reynolds number is directly dependent on the velocity.

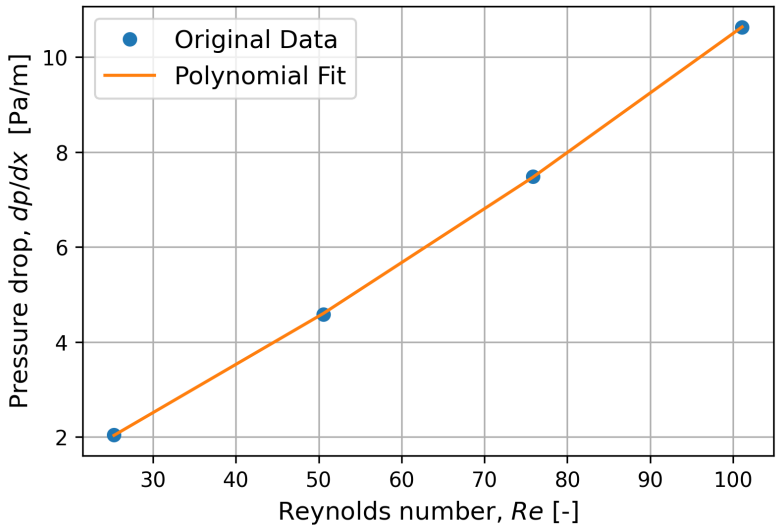

Figure 7.6: Pressure drop for several Reynolds numbers.

The original data, i.e., the pressure drop for different Reynolds numbers was approximated using a polynomial fit. The polynomial fit was chosen through an iterative process, by experimenting

with various degrees of trend lines to observe their behavior. A sufficient polynomial fit is given by:

$$\frac{dp}{dx} = \frac{dp}{dx}(Re) = 0.00023(Re)^2 + 0.0838Re - 0.23551, \tag{7.2}$$

was then implemented as a *momentum source*, in Equation (7.3), where $S_M(Re)$ is the mentioned *momentum source* term as a function of the Reynolds number Re and L the total length of the channel subdomain.

$$S_M = S_M(Re) = -(0.00023(Re)^2 + 0.0838Re - 0.23551) \cdot L \cdot [1, 1, 1]^T. \tag{7.3}$$

The *momentum source* described above was applied as a vector, conforming with previous cases because the *momentum source* definition in STAR-CCM+ is classified as a vector. Since the *momentum source* in this case is a function of the Reynolds number which is a direct function of the mean velocity, the *momentum source derivative* was set to 0 for x, y, z. The resulting reduced dimensional model for the *Pin-Fin* is denoted as *Pseudo 2D-CX*, indicating its different developed approach.

7.3 Evaluation and Discussion

This section highlights the results for the simulations of the *Pin-Fin* geometry with $Re \approx 25$ at the channel inlet, corresponding to an inlet velocity of $U \approx 0.033\ m/s$. From observation of the velocity contour plots, it becomes apparent that the *3D*, *Pseudo 2D* and *Pseudo 2D-CX* models closely align in regard to the jet, which verifies that the *denser mesh region* is sufficiently large to facilitate complete flow development before exiting the channel subdomain. Figure 7.7 demonstrates the velocity distribution from the channel to the room subdomain, observed from above, i.e., the xy plane for all three models, including the jet that is formed in the room subdomain. Figure 7.8 displays a zoomed view for the velocity near the channel end and a small part of the room subdomain. However, the pressure contour plots reveal that the *Pseudo 2D* model exhibits significantly lower pressure compared to the *3D* model, see Figure 7.9. The *Pseudo 2D-CX* model showcases similar pressure in the channel subdomain compared to the *3D* model, with a slight variation in pattern resulting from the implementation of the new field function, see Section 7.2.

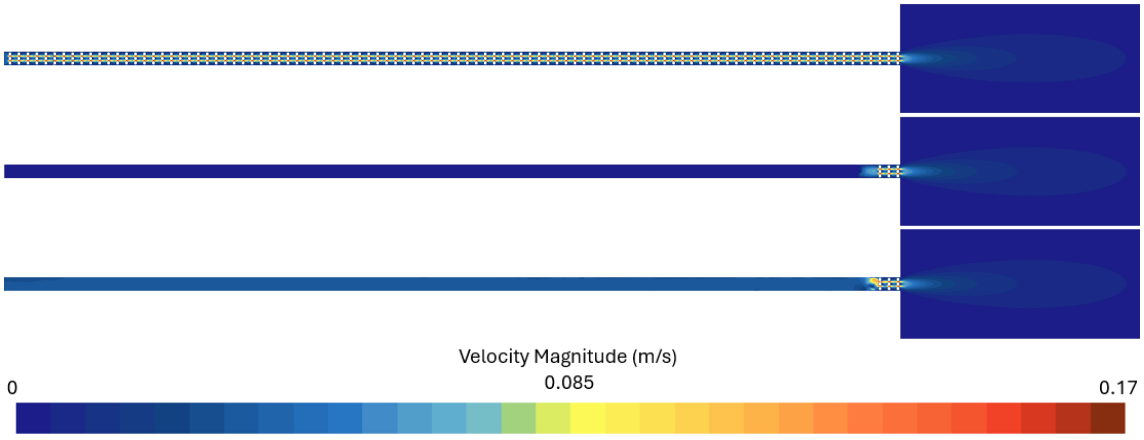

Figure 7.7: Contour plot for xy plane; Velocity magnitude for *3D* model (top), *Pseudo 2D* model (middle) and *Pseudo 2D-CX* model (bottom), respectively.

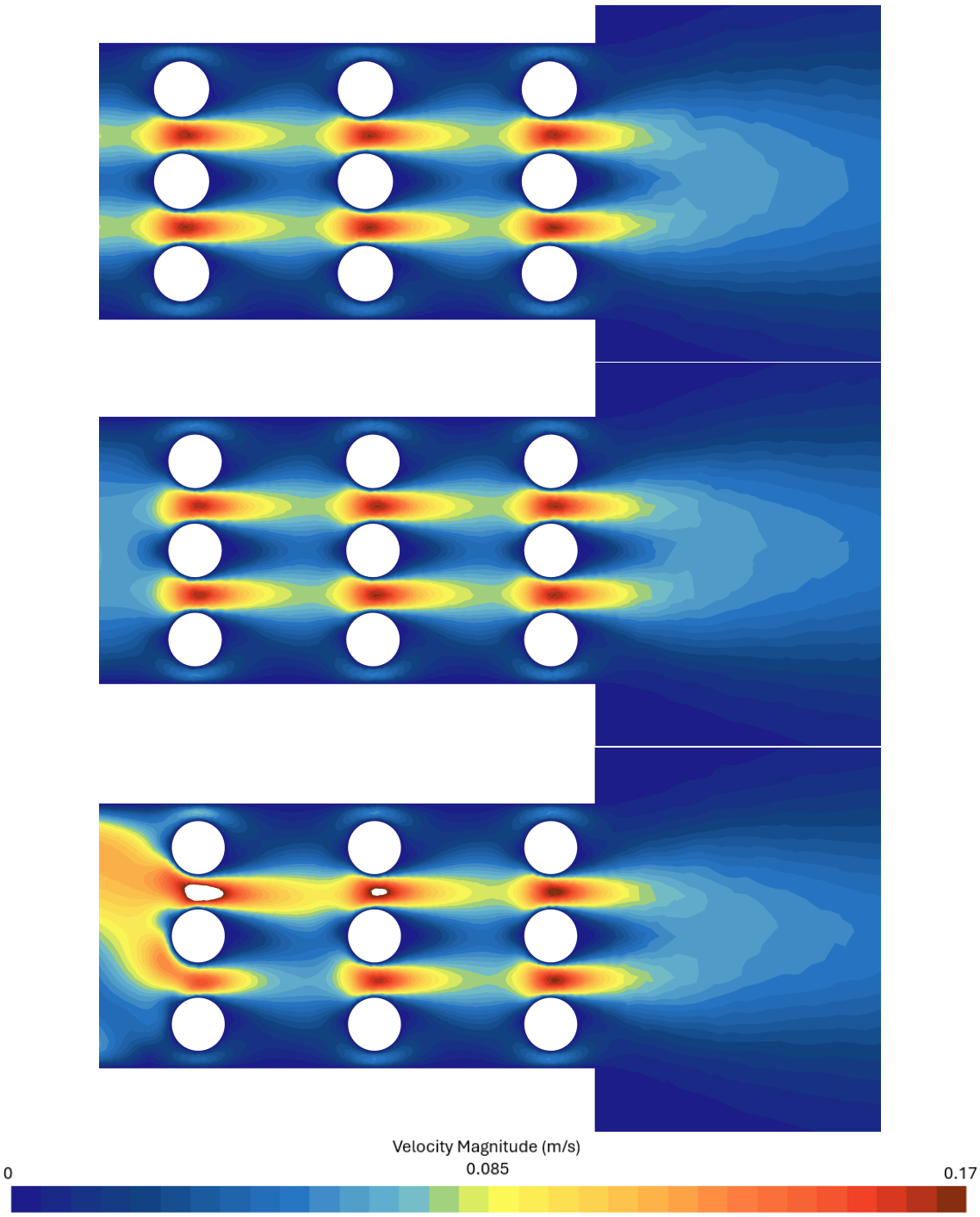

Figure 7.8: Contour plot for *xy* plane; Velocity magnitude for *3D* model (top), *Pseudo 2D* model (middle) and *Pseudo 2D-CX* model (bottom), respectively.

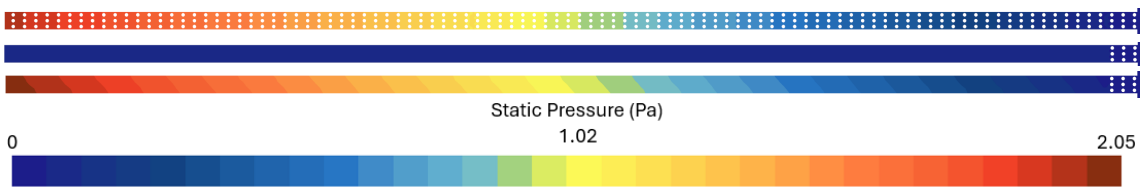

Figure 7.9: Contour plot; Static pressure for *3D* model (top), *Pseudo 2D* model (middle) and *Pseudo 2D-CX* model (bottom), respectively.

To provide a more detailed representation of the obtained results, graphs illustrating the pressure and velocity along the center-line of the channel and room subdomain, respectively, were generated, see Figures 7.10-7.11.

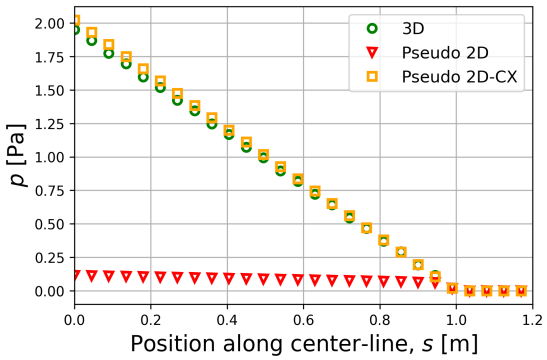

Figure 7.10: Pressure p along center-line of domain.

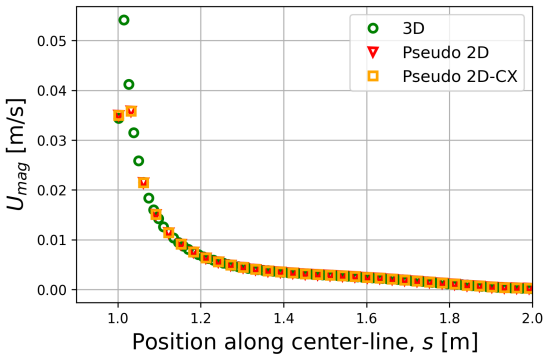

Figure 7.11: Velocity magnitude U_{mag} along center-line of domain.

The pressure values across the channel are significantly lower in the *Pseudo 2D* model compared to the *3D* and *Pseudo 2D-CX* models. In this case the pressure in the *Pseudo 2D-CX* model is more reliable than the *3D* model since the results in the latter have not fully converged due to mesh limitations. In this case, the comparison is thus not strictly conducted between the reduced dimensional model and the *3D* equivalent. Instead, the *3D* model is included to mainly serve as a demonstration of a feasible fully resolved simulation. Noteworthy, is that the *3D* simulation has almost fully converged, exhibiting very low levels of mesh-dependency. Furthermore, it is apparent that the velocity distribution along the center-line of the room subdomain, see Figure 7.11, showcases similar results for all models. This indicates that the *denser mesh region* is large enough in the channel. As a result, there is a similar velocity distribution in the room subdomain. This conclusion can be further justified based on the argument that with sufficient upstream conditions, assuming an identical downstream setup, the results should be identical for all models. In the same way as the previous analyses, residual plots were constructed, see Figure 7.12-7.13, based on Equations (5.5)-(5.6).

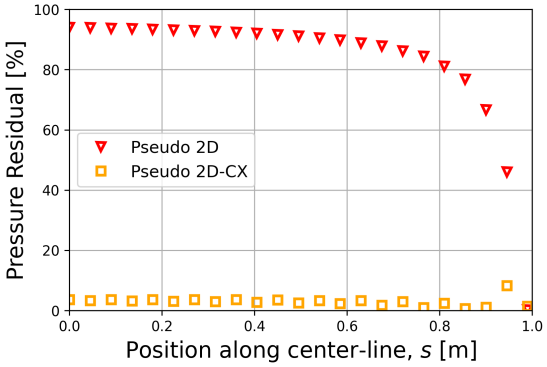

Figure 7.12: Pressure residuals, w.r.t., *3D*.

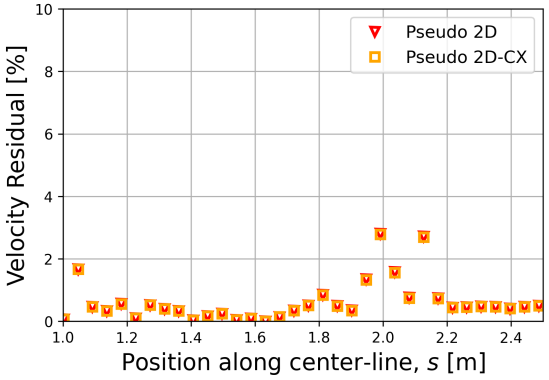

Figure 7.13: Velocity residuals, w.r.t., *3D*.

The pressure residual plot shows a significant difference between the *Pseudo 2D* and *Pseudo 2D-CX* model. It is evident that the pressure residuals for the *Pseudo 2D* model exceed 80% across most of the channel, whereas the *Pseudo 2D-CX* consistently maintains residuals below 5% throughout most of the channel subdomain. The velocity residual plot demonstrates that the residuals along the room subdomain for the *Pseudo 2D* and *Pseudo 2D-CX* are below 5%. Indicating, that both the *Pseudo 2D* and *Pseudo 2D-CX* model exhibit similar velocity distribution as the *3D* model. Furthermore, it is worth noting that the residual for velocity is identical for both the *Pseudo 2D* and *Pseudo 2D-CX* models, which is expected as identical mesh settings and *denser mesh region* configuration, are employed in both models. Additionally, as the field function solely aids the computation of pressure drop in the *Pseudo 2D-CX*, it does not influence the velocity. Another thing that could be noted is that the residuals increase after approximately 1.75 m and start decreasing after 2 m. The reason is that the cells experience a change after approximately 1.75 m, transitioning from a finer mesh to a coarser one. This effect is further amplified by the numerical issues with small numbers, supported by the velocity at positions beyond 1.5 m being close to zero. For the same reason as the previous geometrical features, the actual numerical difference

between the *Pseudo 2D* models and the *3D* model were constructed, see Figure 7.14-7.15, based on Equations (5.7)-(5.8).

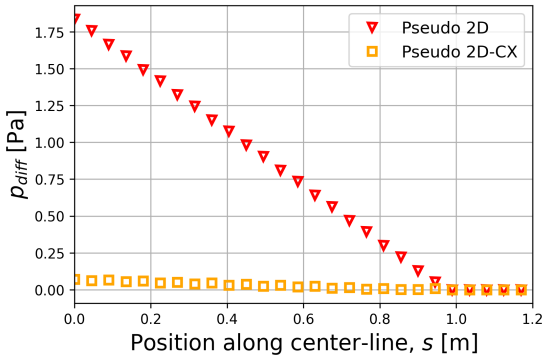

Figure 7.14: Pressure diff., p_{diff}, w.r.t., *3D*.

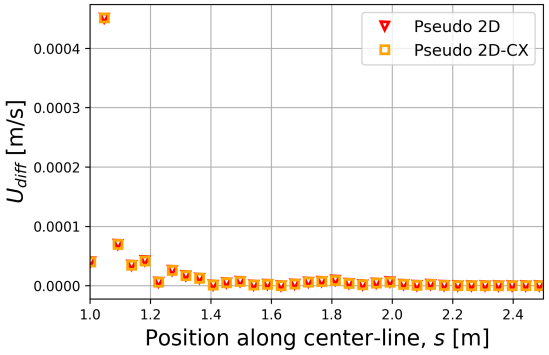

Figure 7.15: Velocity diff., U_{diff}, w.r.t., *3D*.

As anticipated, the pressure difference plot confirms once more that the *Pseudo 2D-CX* model aligns with the *3D* model. As can be noted, the numerical pressure difference is also significantly lower for the corrected version compared to the *Pseudo 2D* model. The velocity difference plot illustrates how small the numerical velocity difference is between the *Pseudo 2D* models and the *3D* model.

Summarizing, the following steps were adopted for the *Pin-Fin* geometry:

1. Creation of a model of a small section of the channel, matching the length of the *denser mesh region*, using a highly refined mesh. Followed by the determination of the pressure drop for different Reynolds numbers.

2. Plot-creation of the pressure drop as a function of Reynolds number, followed by approximating it using a polynomial regression.

3. Creation of a *Pseudo 2D* model with a *denser mesh region* including pin-fins, with the same mesh settings in the *denser mesh region* as step 1.

4. Application of the attained approximating regression-based function as a user-defined field function in the *momentum source* and implement it in the *Pseudo 2D* model in the region enclosed by slip boundaries.

5. Construction of a *3D* model with a sufficiently fine mesh to compare the different simulated models, i.e., the *3D* model, *Pseudo 2D* model, and *Pseudo 2D-CX* model.

The above scheme can be used as a general methodology, and it has been demonstrated to be suitable for analyses involving pin-fin features. Each analysis conducted based on this scheme or methodology is inherently geometry-dependent. Thus, depending on the choice of the user, other pin-fin-related features, e.g., staggered formations can be adopted, assuming appropriate *denser mesh region* length and overall representation in the *Pseudo 2D* model. The most important aspect is that the *Pin-Fin* geometry, follows a specific pattern in the channel, enabling channel modeling as a small section where a periodic boundary condition can be applied. This methodology could also be further extended to cover a broader range of Reynolds numbers, see Section 9.

8 Concluding Discussions

Reaching the end of this thesis, the following summarizes and concludes the key findings and insights obtained from the analyses. The primary aims outlined in the beginning are revisited, and the extent to which these objectives have been achieved is addressed. The applicability of the reduced dimensional model is also reflected concerning meshing aspects and overall results.

The primary objective of this thesis was to develop a reduced dimensional model for laminar pressure-induced gas flows in narrow gaps subjected to a sudden expansion. This was done in addition to the inclusion of testing the developed model on generalized geometrical configurations, including parallel plates, ducts, and pin-fin arrangements. For all tested geometrical features, the *Pseudo 2D-C/C2/CX* demonstrated a high level of accuracy compared to the fully resolved *3D* model. To summarize the methodology and model development for developing the reduced dimensional models, the following steps were adopted:

- Development of a *Simple Geometry* for the parallel plate and duct geometrical configurations.
- Construction of a *Pseudo 2D* mesh.
- Construction of a *denser mesh region* in the *Pseudo 2D* model to ensure sufficient flow development before entering the room subdomain.
- Modification of boundary conditions and implementation of *momentum source* and *momentum source derivative* by the help of user-defined field functions in the region with one cell in the orthogonal direction of the flow, before transitioning to the *denser mesh region*, to accurately resolve the pressure.

Concluding the development of the reduced dimensional model, the subsequent goal was to validate the developed model against three-dimensional simulations. This was done, w.r.t., the observation of mainly two properties, namely, the pressure drop along the channel subdomain and the velocity of the jet in the room. This was executed concurrently for the two configurations of *Simple Geometry*, namely, parallel plates and duct, along with the subjection to several geometrical features implemented onto the channel subdomain. For the case study regarding parallel plates, the developed *Pseudo 2D-C* model, accurately captured both the desired jet image as well as consistently achieving highly accurate pressure drops. The duct-related case study includes an improved reduced-dimensional model, the *Pseudo 2D-C2*, which incorporates a correction factor α based on the deviation in pressure gradient for the *Simple Geometry* of the *Pseudo 2D-C* model. Both reduced dimensional models attained a high accuracy in both considered regards but with the *Pseudo 2D-C2* exhibiting a slightly improved ability to capture the pressure drop.

Furthermore, the pressure drop, indicative of momentum loss throughout the domain, has not been specifically addressed in terms of field function formulation regarding the minor losses caused by sudden expansion and the implemented geometrical features. The theoretical pressure drop derived and used in the field functions, is solely based on the theory of geometrically straight domains, see Section 2.5.5. Meaning, that only the major losses are incorporated by field functions. The case study regarding parallel plates showed that the implemented geometrical features impose negligible minor losses, as a result of the low velocities and feature-dependent minor loss coefficient. This result was found by comparison of the geometries containing bends with the straight channel in *Simple Geometry*. For the cases where the implemented geometrical component imposes a significantly large loss, e.g., *Constricted Duct*, the reduced dimensional models sufficiently manage to accurately depict the pressure drop. Meaning, that they perform well in capturing the total losses without user-related aid except for the hydraulic diameter specification. This can be concluded by noticing that the *Pseudo 2D-C2* model consistently aligns with the results of the full *3D* equivalent for the exemplified case of the *Constricted Duct*. The division of mass flow was also fully captured by the reduced dimensional model as displayed by the *Branching Duct* geometry and thus displayed a high potential for a wide range of implemented geometries with no limiting aspects among the tested features.

The achieved reduction in cell count was significant for the reduced-dimensional models. In parallel plate configurations, the relative cell count within the channel subdomain was less than approximately 1%. Similarly, for duct-related cases, the relative cell count was less than approximately 1.5% for all cases. This demonstrates the potential for reduced computational cost and an increase in time efficiency for all considered simulations. The difference in cell reduction between the configurations can be attributed to the slightly larger *denser mesh region* as a prerequisite in the duct

geometries. The results and discussions regarding the case study for parallel plates and the duct are found in Sections 5 and 6, respectively.

The reduced dimensional model has thus been demonstrated to function desirably for laminar flows of Reynolds numbers below 100 for flows in narrow gaps subject to a sudden expansion. The applicability of the model in terms of implemented features was concluded to be absolute based on the regarded flow features but varied in terms of meshing aspects due to discontinuous attributes not being mesh-able with a desired *Pseudo 2D* configuration. For more information on some of the modeling limitations in terms of mesh generation, see Appendix F. Additionally, there may be unexplored limitations related to changes in physics or significant changes in geometry, such as when examining high Reynolds numbers that lead to turbulent flow features or when the domain is considered much smaller where adoption of the, e.g., Boltzmann equation becomes necessary to capture the sub-continuum physics. These aspects are addressed further in Section 9. Furthermore, as the developed models are of reduced order, both mass and momentum cannot be conserved in the channel subdomain simultaneously. This is an unavoidable feature for this case of reduced dimensional modeling. Hence, the utilization of the *denser mesh region*, adjustments of boundary conditions, and implementation of user-defined field functions to regain conservation of the properties before the flow enters the room subdomain.

Due to the different nature of the modeling of the *Pin-Fin*, e.g., by the geometrical exclusion of a large portion of the fins, the vast part of the pressure drop contribution from the minor losses is encompassed by the derived pressure gradient from the periodicity-based simulation of the *small section-channel* model. The field function implementation was obtained by calculating the pressure drops across various Reynolds numbers based on the *small section-channel* model, and a polynomial fit was applied to approximate the data. The polynomial fit was implemented as a *momentum source*, resulting in the *Pseudo 2D-CX* model. The simulation results indicated good alignment between the *Pseudo 2D-CX* and the fully resolved *3D* model, accompanied by a notable reduction in cell count, see Section 7. This demonstrates the methodology applied to a feature with increased complexity. Indicating the potential of reduced dimensional models, in a broader context, for CFD simulations with pressure-induced laminar flows.

9 Future Work

This thesis establishes the foundational principles for transitioning from a fully resolved *3D* model to a *Pseudo 2D* model in a small channel with different geometrical features. The studies and analyses made could be further extended to include a wider range of problems. The following are some proposed ideas that could be considered for future work:

- In this thesis, Reynolds numbers up to $Re = 100$ were analyzed, with a primary focus on $Re \approx 25$, as this range conforms with the application motivating the project. Because of the low Reynolds numbers, all the analyses were conducted using a steady-state approach. However, at higher Reynolds numbers, see Section 2.6, the jet becomes unstable which was also noted when simulating for higher Reynolds numbers. It would therefore be interesting to study flows with higher Reynolds numbers in the channel and see how they would affect the outflow by using a transient approach. The studies can be conducted on the same geometrical features presented in this thesis to compare the results. It would also be interesting to examine high Reynolds numbers that result in a turbulent flow within the channel to determine if the same field functions, *momentum source* and *momentum source derivative* can be used to accurately solve the pressure in the channel. Additionally, determining which turbulence model should be used for cases of turbulent flow would be valuable.

- Specific concern to the industry, for example within electronics; comprising much smaller domains. Such that, considerations of Knudsen number and the movement on the molecular level of the gas become too significant to neglect. Consequently, resulting in abandoning the continuum-based Navier-Stokes equations and adopting, e.g., the Boltzmann equation to accurately model the sub-continuum physics.

- The analysis of the last geometrical feature, i.e., *Pin-Fin* can be further extended and include other pin-fin related features, e.g., staggered formation. Other dimensions could also be tested to see how well the proposed methodology in Section 7 can be employed. By testing various features of pin-fins it might be possible to develop a general field function describing the pressure drop for different pin-fin-related geometries. The methodology can also be further extended to cover a broader range of Reynolds numbers. This includes higher Reynolds numbers where it becomes necessary to use a turbulence model to capture the turbulent effects. Since pin-fins tend to introduce disturbances and flow separation zones with high-pressure regions and accelerated flow between the pin-fins, described by Fernandes [10], therefore turbulence behaviors usually occur at lower Reynolds numbers due to these additional complexities. It would also be interesting to investigate at which Reynolds number the transition from laminar to turbulent flow occurs in the *Pin-Fin* geometry and compare it to the transition in smooth channels.

- Additionally, studying bulk temperature transport and heat transfer within the channel, especially in heat exchangers, could be valuable. Future work could explore how different geometrical features affect heat transfer efficiency and temperature distribution. For instance, analyzing how pin-fin arrays simulated by the reduced dimensional models perform to ultimately study heat exchanger designs effectively. Moreover, using conjugate heat transfer models coupled with the reduced dimensionality could provide new insights and understanding of thermal behavior in the mentioned setting, enabling more efficient and time-saving simulations involving transfer of heat.

References

[1] FS Dynamics — fsdynamics.eu. `https://fsdynamics.eu/`. [Accessed 25-05-2024].

[2] Joe Alexandersen. Topography optimisation of fluid flow between parallel plates of spatially-varying spacing: revisiting the origin of fluid flow topology optimisation. *Structural and Multidisciplinary Optimization*, 65(5):152, 2022.

[3] A Baloch, P Townsend, and MF Webster. On two-and three-dimensional expansion flows. *Computers & Fluids*, 24(8):863–882, 1995.

[4] Terence D. Blake. Slip between a liquid and a solid: D.m. tolstoi's (1952) theory reconsidered. *Colloids and Surfaces*, 47:135–145, 1990.

[5] Wang Chang, Gao Pu-zhen, Tan Si-chao, and Xu Chao. Effect of aspect ratio on the laminar-to-turbulent transition in rectangular channel. *Annals of Nuclear Energy*, 46:90–96, 2012.

[6] R. E Denton and Y Hu. Symmetry boundary conditions. *Journal of Computational Physics*, 228(13):4823–4835, 2009.

[7] Theodore H.Okiishi Wade W.Huebsch Donald F.Young, Bruce R.Munson. *Introduction to fluid mechanics*. John Wiley and Sons,Inc., 2012.

[8] Franz Durst, A Melling, and James H Whitelaw. Low reynolds number flow over a plane symmetric sudden expansion. *Journal of fluid mechanics*, 64(1):111–128, 1974.

[9] Melkamu Embiale, Addisu Bekele, Chandraprabu Venkatachalam, and Mohanram Parthiban. Cfd simulation of pressure drop in turbulence flow of water through circular, square, rectangular and triangular cross-sectional ducts. *Applied Engineering Letters : Journal of Engineering and Applied Sciences*, 6(1):39–45, 2021. 5.

[10] Royce Fernandes. Investigation of pin fin cooling channels for applications in gas turbines. 2016.

[11] D.F. Fletcher, M. McCaughey, and R.W. Hall. Numerical simulation of a laminar jet flow: a comparison of three cfd models. *Computer Physics Communications*, 78(1):113–120, 1993.

[12] Jan HK Haertel, Kurt Engelbrecht, Boyan S Lazarov, and Ole Sigmund. Topology optimization of a pseudo 3d thermofluid heat sink model. *International Journal of Heat and Mass Transfer*, 121:1073–1088, 2018.

[13] Hassnia Hajji, Lioua Kolsi, Kaouther Ghachem, Chemseddine Maatki, Ahmed Kadhim Hussein, and Mohamed Naceur Borjini. Numerical study of heat transfer and flow structure over a microscale backstep. *Alexandria Engineering Journal*, 60(3):2759–2768, 2021.

[14] Tin-Kan Hung and Enzo O Macagno. Laminar eddies in a two-dimensional conduit expansion. *La Houille Blanche*, (4):391–401, 1966.

[15] HT Huynh, Zhi J Wang, and Peter E Vincent. High-order methods for computational fluid dynamics: A brief review of compact differential formulations on unstructured grids. *Computers & fluids*, 98:209–220, 2014.

[16] A.G. Kravchenko and P. Moin. On the effect of numerical errors in large eddy simulations of turbulent flows. *Journal of Computational Physics*, 131(2):310–322, 1997.

[17] Hyun Geun Lee and Junseok Kim. Two-dimensional kelvin–helmholtz instabilities of multi-component fluids. *European Journal of Mechanics - B/Fluids*, 49:77–88, 2015.

[18] Enzo O Macagno and Tin-Kan Hung. Computational and experimental study of a captive annular eddy. *Journal of fluid Mechanics*, 28(1):43–64, 1967.

[19] Lewis F Moody. Friction factors for pipe flow. *Transactions of the American Society of Mechanical Engineers*, 66(8):671–678, 1944.

[20] Manh Nguyen and ha Sang. Minor head loss analysis of laminar fluid flow in complex geometries. *Journal of Science and Technique*, 18:5 18, 12 2023.

[21] Bastian E. Rapp. Chapter 9 - fluids. In Bastian E. Rapp, editor, *Microfluidics: Modelling, Mechanics and Mathematics*, Micro and Nano Technologies, pages 243–263. Elsevier, Oxford, 2017.

[22] W. Brian Rowe. Chapter 2 - Basic Flow Theory. In W. Brian Rowe, editor, *Hydrostatic, Aerostatic and Hybrid Bearing Design*, pages 25–48. Butterworth-Heinemann, Oxford, 2012.

[23] Siemens Digital Industries Software. Simcenter STAR-CCM+ User Guide. In *Volume Meshers*, chapter Thin Mesher Expert Properties. 2023.

[24] Siemens Digital Industries Software. Simcenter STAR-CCM+ User Guide. In *Theory*, chapter Finite Volume Discretization. 2023.

[25] Siemens Digital Industries Software. Simcenter STAR-CCM+ User Guide. In *Simulating Physics*, chapter Flow Regimes. 2023.

[26] Siemens Digital Industries Software. Simcenter STAR-CCM+ User Guide. In *Simulating Physics*, chapter Applying Flow Sources and Sinks. 2023.

[27] Siemens Digital Industries Software. Simcenter STAR-CCM+ User Guide. In *Volume Meshers*, chapter Thin Mesher. 2023.

[28] Yupeng Sun, Hafiz Muhammad Adeel Hassan, and Joe Alexandersen. Application of a reduced-dimensional model for fluid flow between stacks of parallel plates with complex surface topography. *Fluids*, 8(6):174, 2023.

[29] Henk Kaarle Versteeg and Weeratunge Malalasekera. *An introduction to computational fluid dynamics: the finite volume method*. Pearson education, 2007.

[30] F.M White. *Fluid Mechanics*. McGraw-Hill Education. McGraw-HillHigher Education, 2016.

[31] Mohd Hafiz Zawawi, A Saleha, A Salwa, NH Hassan, Nazirul Mubin Zahari, Mohd Zakwan Ramli, and Zakaria Che Muda. A review: Fundamentals of computational fluid dynamics (cfd). In *AIP conference proceedings*, volume 2030. AIP Publishing, 2018.

Appendices

Appendix A

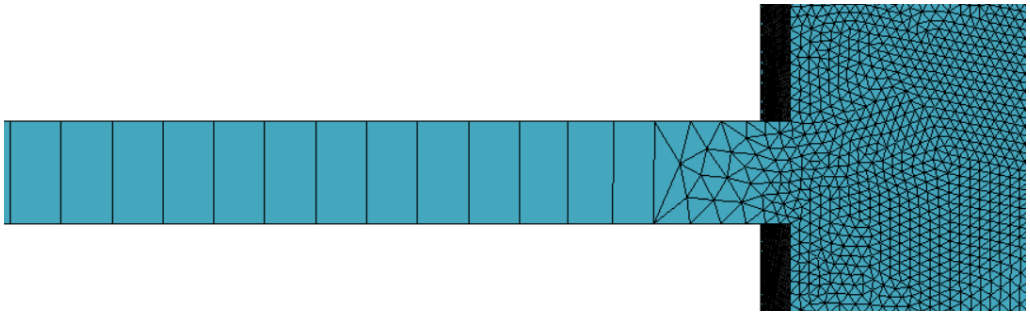

Figure 9.1: Surface mesh; transition from channel via sudden expansion into room subdomain.

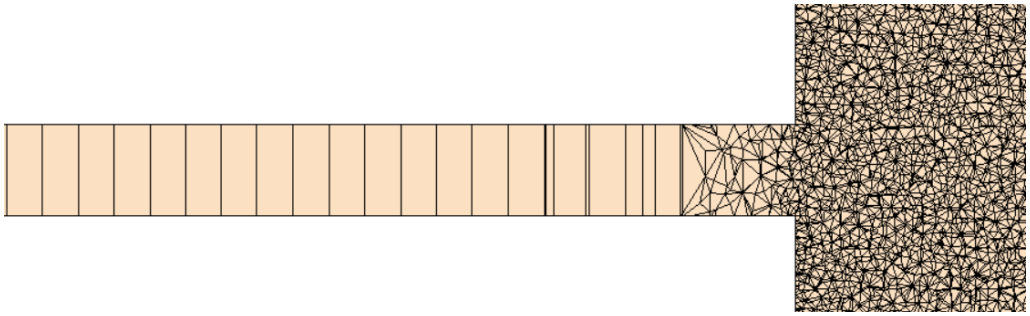

Figure 9.2: Internal mesh; transition from channel via sudden expansion into room subdomain.

Appendix B

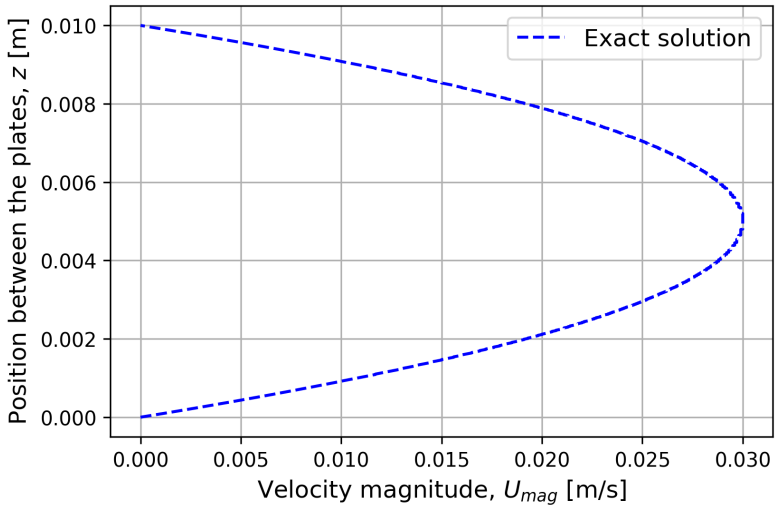

Figure 9.3: Poiseuille velocity profile - exact analytical solution for flow between plates of inlet velocity $U = 0.02\,m/s$, computed for flow validation.

Appendix C

Comparison Between Parabolic and Planar Velocity Profile for Jet Formation

Early in the development of the reduced dimensional model, the difference between a planar and parabolic velocity profile entering the room subdomain was concerned. The comparison was conducted between two simulations, where the first solely contained the room with the channel replaced

by an inlet, and the second, contained the full *Simple Geometry*. Here, the first enters the room with a planar profile and the second with the parabolic profile. The results in terms of velocity magnitude, extracted along the center-line of the domain can be seen in Figure 9.4.

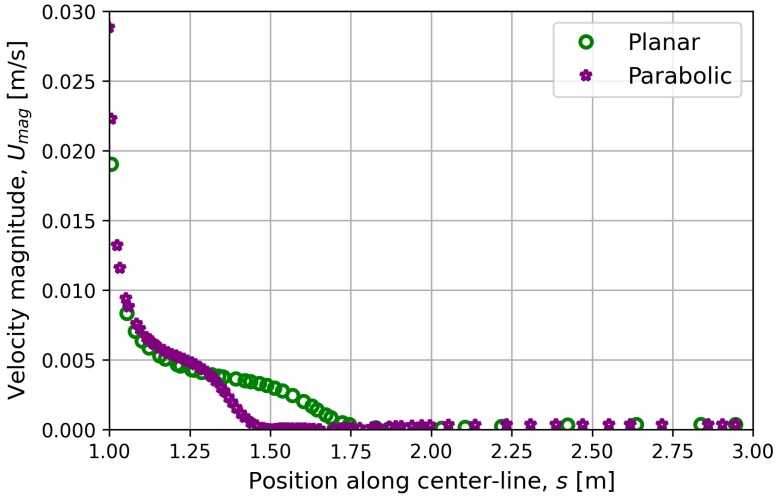

Figure 9.4: Velocity U_{mag} along the domain for planar and parabolic profile.

Here, it can be observed that the velocity is similar between the two profiles for $0 \leq x \leq 1.3\,m$ but towards the end of the jet significantly different. For the essential jet region, i.e., approximately $-0.05 \leq z \leq 0.015\,m$, the velocities also exhibit similar to almost equal values. The main difference is that the parabolic profile contain a slightly larger center-line (maximum) velocity, as anticipated, due to its mean (bulk) velocity resulting in a higher peak velocity but lower values of the extremities. Furthermore, the planar profile extends much further than the parabolic equivalent. This is likely because the center-line fluid "particle" experiences a slip from its neighboring elements, meaning that it takes longer for it to be subject to shear from top and bottom in the xz plane. This concludes that a planar condition is not sufficiently similar to a parabolically developed profile.

The observation was performed in coherence with the adoption of the *denser mesh region* at the channel end. This instead ensured, for all simulations, to accurately development the parabolic profile and resultingly the jet. This conclusion is mainly based on observation of the center-line velocity.

An attempt to locally influence the development of a parabolic velocity profile was performed. This was done utilizing a user-defined field function in STAR-CCM+ to formulate a momentum source dependent on the vertical position in the early part of the room subdomain. Based on the attempt, it was found that the pursued locality was unable to be obtained and only larger areas than that of the small entrance region were possible using this method. As no success was achieved, the attempt was discarded.

Appendix D

Diminish of Vertical Velocity after Bend

This section addresses the deviant feature prominent in the *Pseudo 2D* model for bending features with full 2D mesh. This attribute arose in the form of an increase in velocity magnitude for the *Pseudo 2D* model after the bend. This was seen before the implementation of the *Pseudo 2D-C* model and negatively impacted the formation of the jet. It was found in Figure 9.5 that the vertical velocity before the bend did not completely diminish as the channel became horizontal, explaining the observed deviant feature. This was concluded to be due to the presence of only one cell between the walls across the radial direction of the bend, in the cross-sectional plane xz. Consequently, it is impossible to accurately transport flow information with the no-slip boundary condition while being subject to directional change. However, this effect was fully mitigated in the *Pseudo 2D-C* model, by the replacement of the slip boundary condition on the walls, permitting the fluid to adopt prerequisite cell values to change direction.

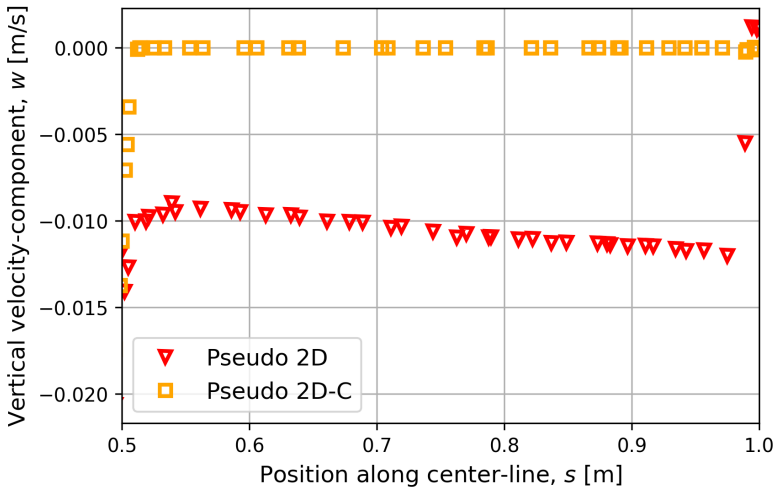

Figure 9.5: Vertical velocity component w in horizontal section of the channel.

In addition to the presented analysis, a brief validation was carried out. Performed to increase the knowledge of the behavior of flows subject to elbows or bends. The validation was scoped around the aim of determining how fast the flow's perpendicular velocity components diminish and when the straight channel flow properties are recovered after a smooth/sharp bend. The analysis is presented in the following section.

Both the sharp and the smooth bend, found in Section 5, are considered respectively for various inlet velocities. The inlet velocities simulated are $U = 0.02$, 0.04, 0.06, 0.08 (m/s) and their corresponding Reynolds numbers $Re \approx 25$, $Re \approx 50$, $Re \approx 75$, $Re \approx 100$. Figure 9.6 and 9.7 display the vertical velocity component over a distance after the bend.

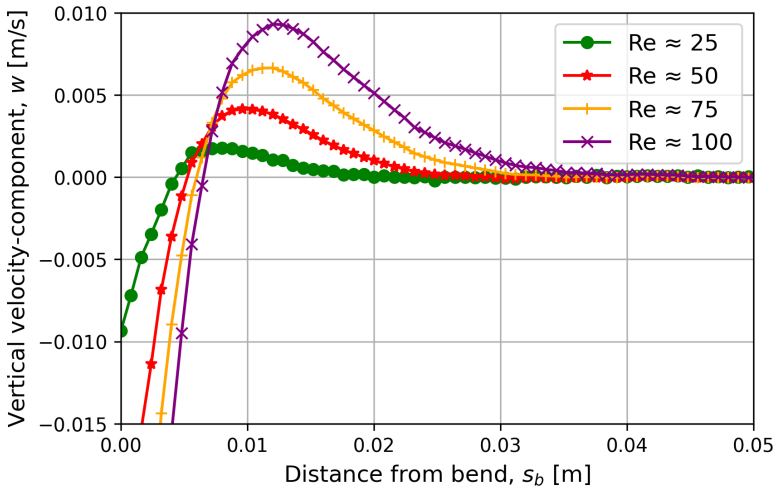

Figure 9.6: Vertical velocity component w between plates at distances from the sharp bend.

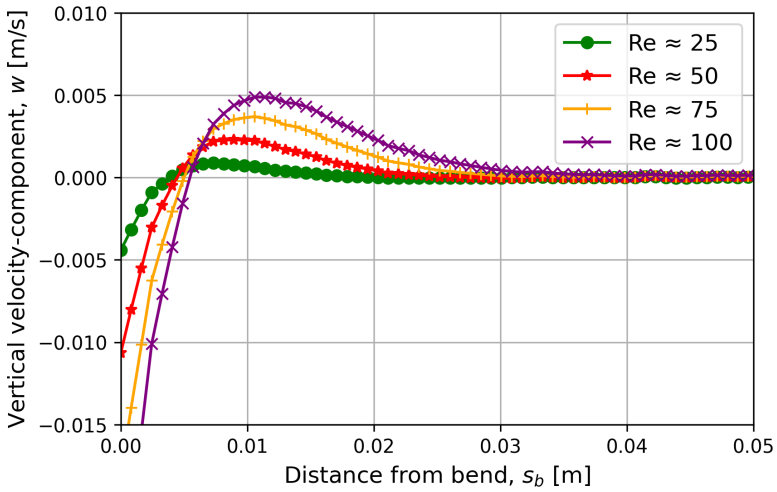

Figure 9.7: Vertical velocity component w between plates at distances from the smooth bend.

Several conclusions can be drawn from the observation. The sharper bend exhibits a steeper velocity gradient mainly in the range $0 \leq s_b \leq 0.01\,m$ due to the separating flow from the right wall as a result of the discontinuity in the geometry and boundary influence. The smooth bend exhibits constant influence from its continuously redirecting walls and no flow separation occurs. Consequently, the vertical velocity component is diminishing more gradually and less steeply for the smooth bend in comparison to the sharp bend. This impacts the rebounding, positive vertical velocity, the distance it reaches its maximum, and ultimately the point where the flow in the vertical direction is completely worn off. This leads to the sharp bend attaining a slightly higher maximum and further distance at which it occurs compared to the smooth bend. The approximate values at which the vertical flow component has diminished completely are found in Table 9.1.

Table 9.1: Positions of diminished vertical velocity component for smooth and sharp bend.

Feature	**Re**	**Distance from bend, s_b [m]**	**Vertical velocity, w [m/s]**
Sharp bend	25	0.020	9.8e-6
-	50	0.028	7.8e-5
-	75	0.037	8.3e-5
-	100	0.045	6.5e-5
Smooth bend	25	0.018	7.0e-5
-	50	0.024	7.8e-5
-	75	0.030	9.0e-5
-	100	0.040	9.8e-5

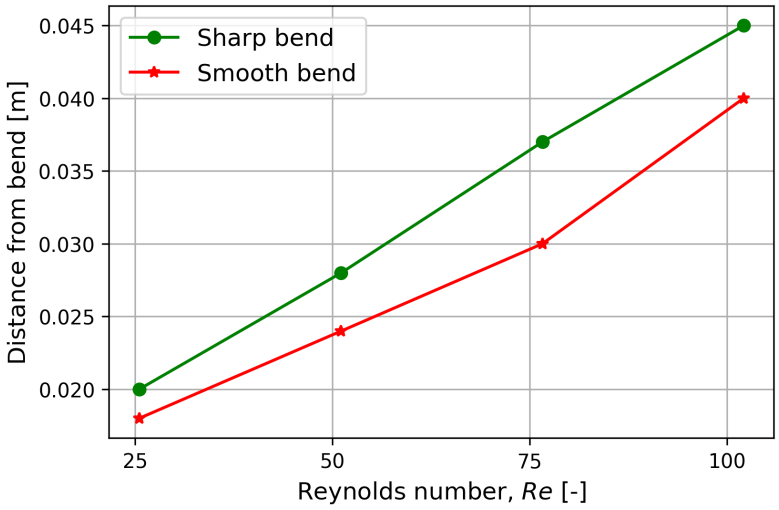

Figure 9.8: Approximate distance from bend where zero velocity in vertical direction is reached, w.r.t., *Re*.

Appendix E

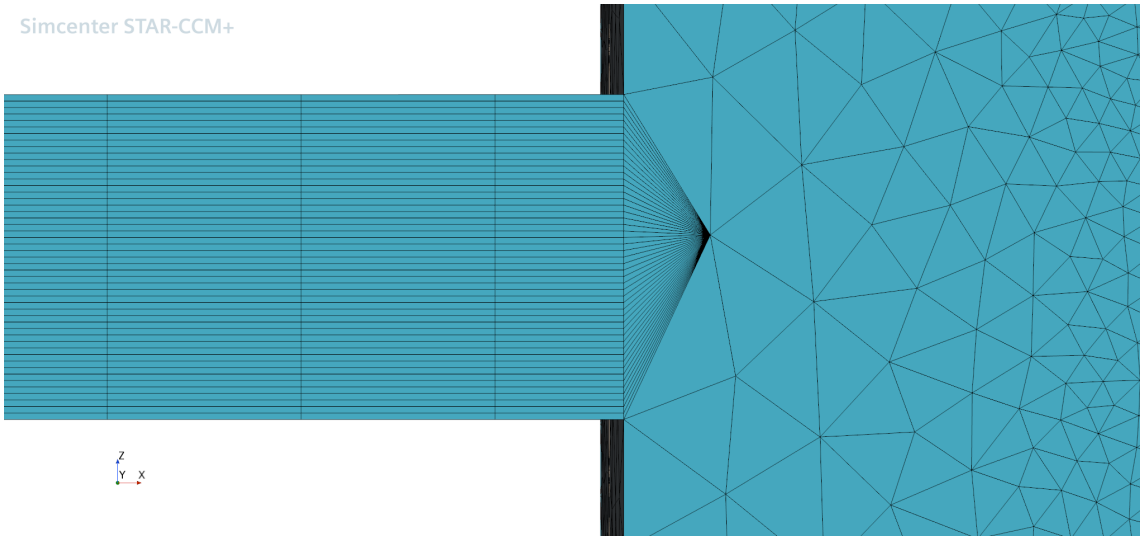

Figure 9.9: Surface mesh transition from structured to unstructured mesh (50 layers in the channel between the plates).

Appendix F

Model Limitations and Meshing Aspects of Pseudo 2D in STAR-CCM+

This section highlights some of the intricacies and important aspects when generating a *Pseudo 2D* mesh. This is done, w.r.t., various geometries and software-specific settings to achieve a high degree of applicability. During the construction of various geometries, employing the *Thin Mesher* [27] with precision and a resulting desired configuration, proved to be rather intricate. Before addressing the regarded aspects, some explanation of the *Thin Mesher* and how it functions is in order. The *Thin Mesher* provides the user with, mainly, two different approaches in terms of meshing implementation. The first, being the *Parts-Based Meshing* used in this project, which enables the choice of *Thin Mesher*, and as displayed by the Figure 3.9 in Section 3.4.2, becomes available after choosing either *Tetrahedral Mesher* or the *Polyhedral Mesher*. This implementation enables the automatic recognition of the geometry areas as "thin" or "bulk". The mesh, which is thereafter constructed for the areas considered thin, is comprised of prismatic-type cells. Resultingly, as seen in Figure 9.10, the confined space between the plates spans the elongated dimension of the cells

of prismatic type. Thus, forming the desired *Pseudo 2D mesh* property with one cell between the plates in the height direction. The second approach in terms of *Thin Mesher* utilization, i.e., *Region-Based Meshing*, further explained in [27], is to select the *Thin Mesher* as a *Core Volume Mesher*. This approach was not explored as it was not found in the software, most likely due to the prechosen *Automated Mesher*.

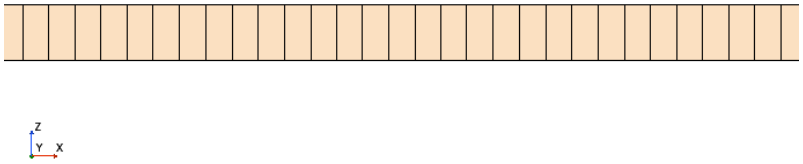

Figure 9.10: A straight section fully comprised of *Pseudo 2D* mesh.

After providing a brief explanation of the options and the choices made in terms of *Thin Mesher*, the discussion of the various encountered aspects can be presented. Primarily, the complexity emerged during the exploration of which geometrical features allowed non-discontinuous, valid mesh transitions, as the dependency on both the geometrical feature and also various *Thin Mesher* settings showed significant influence. To present some of the findings with regards to which cases provided a valid mesh and which ones did not, a list and a table are displayed below. The list includes some of the considered geometrical features evaluated, divided into *Cases* for ease of referencing. Table 9.2 presents the mesh settings evaluated.

- Case 1: Bends/elbows, both smoothly bent with a continuous thickness and radius, and non-discontinuous sharp equivalents. Real-world applications such as pipes or ducts are comprised of the geometrical features of this case.
- Case 2: Increased or decreased plate distance for a section of the channel. Both gradual and abrupt transitions. Real-world applications such as diffusers or mufflers for increased space and constricted sections in ducts or valves for decreased space can be included in this category.
- Case 3: Linearly increasing distance between plates for the end of the channel, i.e., diverging plate spacing. Real-world applications included are diverging channel or nozzles.
- Case 4: Corrugated plates of zigzag formation. Heat exchangers are an example of a real-world application.

Table 9.2: Description of *Thin Mesher Expert Settings* [23].

Thin Mesher Expert Setting	**Description**
Thin Mesher Maximum thickness	This option removes the automatic identification of thin areas and enables a user-specified threshold value in the format of either a specified size, $S\ [m]$, or as a fraction of the *Base Size* of the mesh. The parts of the geometry which are larger than specified setting are considered bulk and conversely, the smaller become considered as thin.
Thin Mesher Surface Size Ratio	This option allows the user to set a threshold for the ratio of the surface cell size (local).

For *Case 1*, as previously mentioned, the continuous smooth bend version was completely comprised of the *Pseudo 2D* model, while the sharp bend equivalent generated an unstructured 3D. These resulting meshes were both obtained without the inclusion of adjusting the *Thin Mesher Expert Settings* and instead only relying on the automatic generation of the mesh.

For *Case 2* in the above list, a thickness ratio of $< 1/2$ and cross-sectional area $< 1/4$ for both

gradual and abrupt increases and decreases, respectively, the mesher only identified the thinner sections as "thin". This results in constricted sections becoming the sole thin part and enlarged sections being comprised of 3D unstructured mesh. Conversely, with a thickness ratio of $> 1/2$ and $>1/4$ in cross-sectional area ratio, the non-discrete, gradual transitions between various thicknesses allowed for a full *Pseudo 2D* mesh to form, both using either fillets or chamfers as a transitional component. Various *Thin Mesher Expert Settings* were tested to achieve even lower thickness ratios with a valid *Pseudo 2D* mesh. Examples of configurations that provided a full *Pseudo 2D* mesh. However, due to the employment of the *Parts-Based Meshing* and the whole geometry being a single part, the *denser mesh region* became comprised of *Pseudo 2D* mesh as well and lost its desired properties. An approach to potentially avoid this issue would be to divide the geometry into separate parts, which consequently might enable the possibility of conserving the unstructured attribute of the *denser mesh region*.

Case 3, as a consequence of being directly connected to the room subdomain, became comprised of a three-dimensional unstructured mesh in the diverging section. By modification of the *Thin Mesher Expert Settings* gradually increasing/decreasing sections can be comprised of a *Pseudo 2D* mesh. However, as the *denser mesh region* governs an important feature of the *Pseudo 2D* model. Our recommendation in terms of approach for diverging nozzles would be to simply let the diverging/converging transition be comprised of a full *3D* mesh with appropriate density.

The corrugation evaluated; a zigzag pattern with an inclination/declination of $\approx 11°$, displayed good behavior in terms of *Pseudo 2D* meshing and is thereby likely to attain a high level of *Pseudo 2D* meshing for acute inclination angles.

Even though not all geometrical features were rigorously explored in terms of mesh-applicability of the *Pseudo 2D* model. The above highlights some of the characteristic features, possibilities, and suggestions to how the validity and applicability can be influenced by the user. It was found that both the model in its full capacity and the mesh itself, are heavily dependent on geometrical factors. Ultimately, outside of this thesis, it is left for the one performing the simulation to decide if the attained properties are desirable, and in some aspects, simply reducing the overall mesh count, without achieving a concise *Pseudo 2D* mesh, can be desirable.

Appendix G

Contributions

Here, the specific contributions each author made to this thesis are outlined. It is important to note that both authors participated in every stage of the process, contributing to all aspects of the thesis and writing in all sections of the report.

Abdulla Rahmah
Contributions made include but are not limited to method and generation of *Simple Geometry* (duct), *Single Sharp Bend*, *Multiple Sharp Bends*, *Multiple Bending Duct* and *Pin-Fins*.

Leo Flydalen
Contributions made include but are not limited to method and generation of *Simple Geometry* (parallel plates), *Single Smooth Bend*, *Multiple Smooth Bends*, *Branching Duct* and *Constricted Duct*.